Title
Nuclear Excitation by Electronic Transition of U-235

Author
Chodash, Perry Adam

Publication Date
2015

Peer reviewed|Thesis/dissertation

Nuclear Excitation by Electronic Transition of U-235

by

Perry Adam Chodash

A dissertation submitted in partial satisfaction of the

requirements for the degree of

Doctor of Philosophy

in

Engineering-Nuclear Engineering

in the

Graduate Division

of the

University of California, Berkeley

Committee in charge:

Professor Eric B. Norman, Chair
Professor Karl A. Van Bibber
Professor Michael Nacht
Doctor Jason T. Burke

Summer 2015

Nuclear Excitation by Electronic Transition of U-235

Abstract

Nuclear Excitation by Electronic Transition of U-235

by

Perry Adam Chodash

Doctor of Philosophy in Engineering-Nuclear Engineering

University of California, Berkeley

Professor Eric B. Norman, Chair

Nuclear excitation by electronic transition (NEET) is a rare nuclear excitation that is theorized to occur in numerous isotopes. One isotope in particular, ^{235}U, has been studied several times over the past 40 years and NEET of ^{235}U has never been conclusively observed. These past experiments generated conflicting results with some experiments claiming to observe NEET of ^{235}U and others setting limits for the NEET rate.

This dissertation discusses the latest attempt to measure NEET of ^{235}U. If NEET of ^{235}U were to occur, ^{235m}U would be created. ^{235m}U decays by internal conversion with a decay energy of 76 eV and a half-life of 26 minutes. A pulsed Nd:YAG laser operating at 1064 nm with a pulse energy of 789 mJ and a pulse width of 9 ns was used to generate a uranium plasma. The plasma was captured on a catcher plate and electrons emitted from the catcher plate were accelerated and focused onto a microchannel plate detector. A decay of 26 minutes would suggest the creation of ^{235m}U and the possibility that NEET occurred. However, measurements performed using a variety of uranium targets spanning depleted uranium up to 99.4% enriched uranium did not observe a 26 minute decay. Numerous other decays were observed with half-lives ranging from minutes up to hundreds of minutes. While NEET of ^{235}U was not observed during this experiment, an upper limit for the NEET rate of ^{235}U was determined. In addition, explanations for the conflicting results from previous experiments are given. Based on the results of this experiment and the previous experiments looking for NEET of ^{235}U, it is likely that NEET of ^{235}U has never been observed.

This dissertation is dedicated to my parents. Thank you for your encouragement and support as I pursued my dream of becoming a scientist.

Contents

List of Figures

List of Tables

Acknowledgments

This work would have been impossible without the guidance and support of many people. I would first like to thank Rick Norman, my advisor at Berkeley, for all of the advice and support he has provided throughout my graduate studies. Rick's ability to find unique solutions for complex problems has always amazed me and his insight was essential for the success of this experiment. I was lucky to have not one, but two advisors for my experiment. Jason Burke, my advisor at Lawrence Livermore National Laboratory, provided additional guidance and a laboratory to conduct the experiment. I have learned so much from his vast knowledge of experimental physics. I would also like to thank my other committee members, Karl Van Bibber and Michael Nacht, for their insight.

Numerous collaborators provided assistance, knowledge, and equipment throughout the experiment. Robert Casperson and Richard Hughes were invaluable sources of information. Scott Wilks provided the plasma simulations. Kiel Holliday, Jason Jeffries, Roger Henderson, Brandon Chung, and Jeff Stanford provided the radioactive samples used during the experiment. Molly Wakeling helped characterize the translation arm and the translation stage. Scott Fisher was somehow able to turn my sticky note drawings into machined parts. I also want to thank John Koglin for his sarcastic remarks and thinking this experiment would never work.

Finally, I would like to thank my friends and family. None of this would have been possible without my parents. They have always encouraged me to pursue my interest in science and without them, I would have never become a scientist. I would also like to thank my brother for constantly asking if I was done. Stopping him from asking that question was a great impetus to finish. A special thanks to my fiancée, Alison, for all of her encouragement and keeping me focused on finishing this work.

The author wrote this dissertation in support of requirements for the degree Doctor of Philosophy in Nuclear Engineering at the University of California, Berkeley. The research is not a deliverable for any United States government agency. The views and opinions expressed are those of the author, and do not state or reflect those of the United States government or Lawrence Livermore National Security, LLC.

Neither the United States government nor Lawrence Livermore National Security, LLC, nor any of their employees makes any warranty, expressed or implied, or assumes any legal liability or responsibility for the accuracy, completeness, or usefulness of any information, apparatus, product, or process disclosed, or represents that its use would not infringe privately owned rights. Reference herein to any specific commercial product, process, or service by trade name, trademark, manufacturer, or otherwise does not necessarily constitute or imply its endorsement, recommendation, or favoring by the United States government or Lawrence Livermore National Security, LLC, and shall not be used for advertising or product endorsement purposes.

This work was performed under the auspices of the U.S. Department of Energy by Lawrence Livermore National Laboratory under Contract DE-AC52-07NA27344. This research was additionally performed under appointment to the Nuclear Nonproliferation In-

ternational Safeguards Graduate Fellowship Program sponsored by the National Nuclear Security Administrations Next Generation Safeguards Initiative (NGSI). This work was further supported by the U.S. Department of Homeland Security, UC Berkeley, and the Nuclear Science and Security Consortium under DOE Contract DE-NA0000979.

Chapter 1

Introduction

Nuclear excitation by electronic transition (NEET) is a rare nuclear excitation that is theorized to occur in certain isotopes. NEET occurs due to a coupling between a nuclear transition and an electronic transition of an atom and is the time reversal of bound internal conversion. Excited bound electrons in an atom typically de-excite by emitting x-rays or Auger electrons. In the case of NEET, the coupling between the electronic transition and the nuclear transition allows for the excited electrons to de-excite by pumping the nucleus to an excited state. Although this nuclear excitation was predicted over 40 years ago, no experiment has conclusively demonstrated the effect. The difficulty in observing NEET comes from the low probability of this excitation occurring. In addition, previous experiments looking for NEET have to exclude competing reactions that generate the same signal. One of the candidate isotopes for NEET is ^{235}U. This dissertation focuses on determining if NEET occurs in ^{235}U and at what rate.

The dissertation is organized into eight chapters. Chapter 1 introduces the two motivations for the experiment. Chapter 2 describes the nuclear and plasma theory relevant for the experiment. The chapter also describes the earlier attempts to measure NEET of ^{235}U. Chapter 3 covers the experimental setup. This includes the equipment used, the laser properties, and the simulations to optimize the optical setup and the electrostatic lens. Chapter 4 begins with the hydrodynamic plasma simulations that modeled the laser ablation plasma. These calculations were used to predict how many ^{235}U nuclei would undergo NEET. The chapter also includes the metal ablation experiments done to understand the basic properties of ablation plasma along with the spot size of the laser. Chapter 5 covers the natural and depleted uranium tests. This includes the initial tests using a radioactive source to calculate ablation parameters along with the initial null tests for the experiment. Chapter 6 describes the initial enriched uranium tests performed. The uranium carbide experiments are discussed in Chapter 7. The results of the enriched uranium tests using uranium carbide were used to determine the ^{235}U NEET rate. Chapter 8 provides concluding remarks and discusses improvements for future measurements.

1.1 Stellar Environments

One area of the universe where NEET may play a major role is within stars. Numerous nuclear reactions occur in the hot plasma of stars. The most well known reaction is nuclear fusion, the power source for all stars. Other important reactions within stars include scattering, capture reactions, and photoexcitation. One reaction that is not well understood and may have a major influence on stellar nucleosyntheis is NEET. Like photoexcitation or inelastic scattering, NEET can excite the nucleus from its ground state to higher lying states. Typical lifetimes of nuclear states are of order picoseconds. Many states do not exist for a long enough time for nuclear reactions to occur on the excited nuclei. However, many nuclei found within stars have low lying nuclear isomers with lifetimes ranging from microseconds up to years. These nuclear isomers can take part in a variety of nuclear reactions. A key difference between these nuclear isomers and their respective ground states is that the isomers have a different spin and parity. Reactions on states with a different spin and parity occur at different rates. The cross sections for reactions on grounds states and reactions on excited states can be vastly different [1–3].

A change in reaction cross sections for nuclei within stars will influence the quantity and ratios for isotopes produced. NEET can influence both the s-process isotopes and the r-process isotopes produced in stars. During the s-process, neutron capture creates many of the heavier isotopes. This is a slow process of neutron capture that occurs over years. Long lived nuclear isomers generated can have different neutron capture cross sections. NEET would produce a fraction of these nuclear isomers. This difference in cross section would affect the ratio of certain isotopes produced within stars. The r-process occurs during supernova and happens over a timescale of seconds. Once again, nuclear isomers can have different cross sections that would change the overall isotope ratios generated within the star. If NEET was measured for a variety of candidate isotopes, that data can be combined with reaction data on those isotopes to predict how the isotope ratios produced in stars changes. This information can be used to improve our knowledge of stellar nucleosyntheis.

1.2 Nuclear Nonproliferation

One of the most pressing issues currently facing this planet is the proliferation of nuclear material and nuclear technology. The nonproliferation treaty (NPT) entered into force in 1970 in order to prevent nonnuclear weapon states (NNWS) from pursuing or obtaining nuclear weapons while still allowing civilian use of nuclear technology. In exchange for not pursuing or acquiring nuclear weapons, nonnuclear weapon states were able to cooperate with nuclear weapon states in order to have a civilian nuclear program. The International Atomic Energy Agency (IAEA) was put in charge of monitoring NNWS. Safeguards agreements between the IAEA and NNWS were established in order to deter states from diverting nuclear material in addition to deterring those states from pursuing nuclear weapon related work. Nuclear safeguards is a key aspect of the NPT. The possibility of numerous states

gaining nuclear weapons increases without the ability of the international community to monitor the nuclear activities of states.

Numerous technologies are used to monitor NNWS. What technology is used depends on which part of the nuclear fuel cycle is being monitored. Although the IAEA monitors all aspects of the nuclear fuel cycle, certain parts of the cycle are more likely to be monitored due to the possibility of diversion of special nuclear material (SNM). Special nuclear material is defined as plutonium, ^{233}U, or material containing an enriched amount of ^{235}U [4]. The ^{233}U, ^{235}U along with ^{239}Pu are fissile isotopes that can be used to make a nuclear weapon. Diversion of SNM is most likely to occur during uranium enrichment, reactor operation, and fuel reprocessing. These three areas are heavily scrutinized by the IAEA and technologies related to these areas are closely monitored with many technologies being export controlled.

Uranium enrichment offers NNWS the ability to create their own fuel needed in nuclear reactors. Many nuclear reactors use low enriched uranium (LEU) in order to run. The most common type of nuclear reactor used around the world, the light water reactor, uses uranium enriched to between 3% and 5% ^{235}U. This uranium is not at a high enough enrichment to be used in a nuclear weapon. However, the enrichment process can enrich uranium to levels far higher than 5%. The next most common level is 20% enrichment. This level of enrichment is used in reactors that are either research reactors or are medical isotope production reactors. Highly enriched uranium (HEU) is defined as uranium containing more than 20% ^{235}U [5]. This is the level of enrichment that is higher than what is necessary for a civilian nuclear program. Although certain nuclear reactors do use uranium enriched beyond the 90% level, proliferation concerns have forced the conversion of many of these reactors down to under 20%.

There are numerous methods to enrich uranium. The most common method used during the 20$^{\text{th}}$ century was gaseous diffusion. In this method, UF_6 gas moves through a specially designed barrier known as a diffusion barrier. The UF_6 molecule containing ^{235}U effuses through the barrier separating it from the UF_6 molecule containing ^{238}U. The output of a single stage is slightly enriched in ^{235}U. Multiple stages are strung together in a cascade in order to obtain the enrichment desired. Gaseous diffusion enrichment plants are large, energy intensive facilities. These plants require thousands of stages in order to enrich uranium. Technology advances over the past few decades has allowed for the use of gas centrifuges for uranium enrichment. In this method, UF_6 gas is placed in a high speed centrifuge. Due to the difference in mass between the molecules containing ^{235}U versus ^{238}U, ^{235}U concentrates closer to the center of the centrifuge. This gas is then fed to another centrifuge forming a cascade similar to the gaseous diffusion process. The benefit of the centrifuge method is that it is far more efficient at separating ^{235}U from the sample. In the case of gaseous diffusion, the separation factor is 1.004. This is compared to approximately 1.3 for the centrifuge method [6]. The majority of uranium enrichment today is done using gas centrifuges. Like gaseous diffusion facilities, centrifuge facilities are costly and energy intensive. Both facilities are very large due to the number of stages necessary to enrich large amounts of uranium. A centrifuge facility requires far fewer stages than a gaseous diffusion plant due to the larger separation factor. Although they can be smaller than diffusion facilities, they require more

advanced technology. For these reasons, it is difficult to build and operate a covert uranium enrichment facility.

The final uranium enrichment method currently under development is laser enrichment. Laser enrichment for uranium was studied for many years at various national laboratories. Los Alamos National Laboratory developed a method called molecular laser isotope separation (MLIS), while Lawrence Livermore National Laboratory developed atomic vapor laser isotope separation (AVLIS). Currently, a facility using the laser isotope separation process called separation of isotopes by laser excitation (SILEX) is being built in the United States. Little is known about the exact process due to its classification. What is known is that the process works by using a finely tuned laser. It is likely that the laser selectively excites UF_6 containing ^{235}U and may disassociate the molecule, while the UF_6 containing ^{238}U is not affected. The ^{235}U can then be separated from the ^{238}U by various methods. For laser isotope separation to work, one needs finely tuned lasers that can selectively excite the molecule containing ^{235}U and optics that can withstand the high laser power and repetition rate necessary to make the process economical. Laser enrichment has a benefit compared to the other enrichment methods in that its separation factor is significantly larger. This means that fewer stages are needed and allows for faster enrichment of uranium. Laser enrichment facilities can be smaller than the more traditional enrichment facilities. This would make covert laser enrichment facilities possible. However, laser enrichment technology is more technologically advanced than the older enrichment methods and creates a technology barrier to countries wanting to covertly enrich uranium using lasers.

Newer technologies that allow for easier methods of uranium enrichment are a double-edged sword. Making uranium enrichment easier and cheaper is a benefit to countries using civilian nuclear technology. Nuclear reactors are used for medical isotope production, scientific research, power generation, and many other areas. Having cheaper fuel due to the lower cost of enrichment is a major benefit to nuclear energy. However, states or non-state actors wanting to acquire nuclear materiel for nuclear weapons can use this technology to hasten their acquisition of material. Newer methods of enrichment are not only more efficient, but they can be easier to hide. The ability to locate enrichment facilities becomes harder as the technology improves. For this reason, newer methods of uranium enrichment need to be investigated to determine if they have the capability of being used to covertly enrich uranium.

One proposed method of uranium enrichment uses NEET to help separate ^{235}U from ^{238}U [7, 8]. Uranium enrichment via NEET is very similar to laser enrichment of uranium. In order for NEET to occur, the electrons need to be excited. This can be accomplished using a high power laser. For this experiment, a Nd:YAG laser was used. However, other high power lasers would suffice. The laser hits the uranium target and generates a plasma. If NEET occurs, it would excite the ^{235}U into its isomeric state, ^{235m}U. The isomeric state of uranium is long lived and decays solely by internal conversion. Internal conversion causes the ejection of a low energy electron from the uranium atom. While ^{235}U has an isomeric state populated by NEET, ^{238}U does not. The decay of ^{235m}U ejects an electron leaving a charged ^{235}U atom. The ^{238}U atoms within the sample are not charged. Applying an electric

field would cause the ^{235}U to separate from the ^{238}U. Like the forms of laser enrichment described above, the ^{235}U is separated from the ^{238}U following irradiation by at least one laser. However, unlike the above methods, the laser used for this process does not have to be specially tuned. In fact, Nd:YAG lasers are ubiquitous around the world. They are used in welding, dentistry, military applications, and scientific experiments just to name a few common applications. The technology barriers for this form of enrichment are not as high as the other laser enrichment methods.

A new form of laser enrichment using NEET of ^{235}U would create numerous challenges for the nonproliferation community. This new form of enrichment may be used to covertly create fissile material. Laser enrichment via the NEET process may be as efficient as current laser enrichment processes if the NEET rate of ^{235}U is large. This creates the possibility that countries could create large amounts of fissile material. The IAEA currently has safeguards in place to monitor countries that enrich uranium, but a new method of uranium enrichment may require different safeguards. In the case of using NEET to enrich uranium, the biggest challenge for the IAEA would be the technology used for the laser is ubiquitous. The laser needed for NEET of ^{235}U can be made using components that are not export controlled. The list of export controlled components may have to be expanded to include various laser components and optics. However, the expansion of export controlled components would be difficult. This is because the lasers that would be able to create NEET of ^{235}U are common and are used for a wide variety of applications. Because export controls may not be able to be implemented, this new form of uranium enrichment would remove the extra layer of protection afforded by export controls. The IAEA would have to rely on its ability to inspect enrichment facilities and its ability to conclude that there are no covert enrichment facilities. Thus, the IAEA could still determine if a country is in violation of their safeguards agreement using current verification techniques. The ability to verify compliance becomes more important without the ability to export control. NEET of ^{235}U may pose a significant proliferation risk if the rate at which it occurs is large enough to make the enrichment process viable. For this reason, measurements of the ^{235}U NEET rate are needed.

Chapter 2

NEET Theory and Previous Experiments

The following chapter discusses the underlying theory necessary to understand the experiment. The chapter begins with an overview of internal conversion. Internal conversion is not only the primary decay mode for ^{235m}U, but it also has relevance to the theory of NEET. Following the discussion of internal conversion, the properties of uranium that are necessary for the theoretical NEET calculations are then discussed. This is followed by the theory of NEET for ^{235}U. Two derivations for the theoretical NEET rate are presented. The laser plasma interaction is then discussed with a focus on the transfer of energy from the laser light to the resulting plasma. The competing nuclear reactions that can create ^{235m}U and generate a signal similar to NEET are discussed along with the probabilities of the reactions occurring within a uranium plasma. The chapter concludes with a description of past experiments that have attempted to determine the ^{235}U NEET rate. Explanations for why past results have differing conclusions are presented.

2.1 Internal Conversion

To understand the intricacies of nuclear excitation by electronic transition, it is important to have an understanding of internal conversion. When a nucleus gets excited from its ground state to an excited state, it will eventually release the excess energy by some form of decay. Gamma ray emission is the most common form of de-excitation. It is possible for nuclei in an excited state to decay by particle emission. For nuclei excited to very high energies, emission of nucleons can occur. In certain nuclei, the excess energy is removed by the emission of an atomic electron in a process called internal conversion. The energy of the emitted electron is equal to the total energy of the nuclear transition minus the binding energy of the atomic electron. Internal conversion directly competes with gamma emission. Because of this, one must account for the internal conversion rate when calculating decay rates for nuclear

transitions. This is accomplished by defining an internal conversion coefficient as

$$\alpha = \frac{\lambda_e}{\lambda_\gamma}, \tag{2.1}$$

where λ_e is defined as the decay rate for internal conversion and λ_γ is the decay rate associated with only gamma emission [9]. With this definition, the total decay rate for a single nuclear transition can be defined as

$$\lambda_t = \lambda_\gamma(1 + \alpha). \tag{2.2}$$

Internal conversion coefficients can be theoretically calculated. Equation 2.3 is a general equation for calculating the internal conversion coefficient for K-shell emission from an electric multipole transition.

$$\alpha_K^L = Z^3 \left(\frac{L}{L+1}\right) \alpha_{fs}^4 \left(\frac{2m_e c^2}{E}\right)^{L+5/2}, \tag{2.3}$$

where Z is the atomic number, L is the multipole order, E is the energy of the transition, m_e is the rest mass of the electron, and α_{fs} is the fine-structure constant [10]. It is important to note that this equation does not take into account relativistic effects or other higher order corrections. However, many important principles governing the probability of internal conversion can be seen and these principles are relevant for this experiment. There are three important features to this equation. First, the internal conversion coefficient increases with Z^3. This means that the probability of internal conversion occurring is much greater for heavier elements like uranium. In addition, the coefficient increases with larger multipole orders. If there is a large difference in spin between the initial and final states for a nuclear transition, it is very likely the transition would de-excite via internal conversion. Lastly, the internal conversion coefficient decreases with higher energy transitions. Based on these characteristics, it suggests that low energy transitions in heavy nuclei with large differences in spin between the states would decay primarily via internal conversion.

Internal conversion involves the transition of an atomic electron from a bound state to being free. There exists a form of internal conversion where instead of an electron going from a bound state to a free state, the electron transitions between two bound states. This form of internal conversion is called bound internal conversion (BIC). BIC would be most evident for nuclei that are stripped of a significant amount of their atomic electrons, thereby preventing the normal internal conversion process. The theory of BIC was laid out by F. F. Karpeshin et al. and the paper focused on the isotope ^{125}Te [11]. Experimental results on ^{125}Te suggest that this rare decay mode does in fact occur [12–15]. The evidence that BIC occurs is important for any measurement looking for NEET. This is because NEET is the inverse of BIC. The fact that BIC occurs in nature suggests that NEET may also occur.

2.2 Uranium Properties

There are numerous isotopes that can undergo NEET. ^{235}U has many properties that make it a very good candidate to look for NEET. Since NEET involves an interaction between the nucleus and the electrons, the nuclear and the atomic properties of uranium are important. Natural uranium consists of three isotopes, ^{234}U, ^{235}U, and ^{238}U. The abundances, half-lives, and the spin and parity for the four uranium isotopes relevant for this experiment and the metastable state in ^{235}U are shown in Table 2.1. Uranium samples either have the natural abundance of ^{235}U, an enriched amount of ^{235}U, or a depleted amount of ^{235}U. Due to the enrichment process, ^{236}U is found in samples of enriched uranium. Although the goal of uranium enrichment is to enrich the sample in ^{235}U, the process also increases the relative amounts of ^{234}U and ^{236}U. Because of this, the specific activity for a sample of enrichment uranium is significantly higher than a sample of natural uranium. The samples used during the experiment were metallic uranium with an oxide layer, metallic uranium binary, or were uranium ceramic. Two types of ceramic targets were used, uranium oxide and uranium carbide.

Isotope	Abundance	Half-life	J^π
^{234}U	0.0054%	2.455×10^5 yr.	0^+
^{235}U	0.7204%	7.04×10^8 yr.	$7/2^-$
^{235m}U	–	≈ 26 min.	$1/2^+$
^{236}U	–	2.342×10^7 yr.	0^+
^{238}U	99.2742%	4.468×10^9 yr.	0^+

Table 2.1: Uranium isotope properties for the four isotopes of interest along with the metastable state [16]. All of the information for the isotopes except for ^{235m}U correspond to their ground states. ^{235m}U is the first excited state of ^{235}U and has an excitation energy of 76.0 eV.

^{235}U is the isotope of uranium that can undergo NEET. ^{235}U primarily decays by alpha emission releasing alpha particles with energies between 4 and 4.6 MeV. ^{235}U can also spontaneously fission and cluster decay with smaller probabilities. ^{235}U is special in that it has the second lowest known nuclear state at 76.0 eV [16]. The only isotope with a lower known nuclear state is ^{229}Th with a 7.8 eV excited state [17]. A level diagram showing the first few nuclear excited states for ^{235}U is shown in Figure 2.1. The first two excited states are most relevant for this experiment. Due to the high Z of uranium, the low energy of the nuclear transition, and the large difference in spin between the ground state and the excited state, the decay of the metastable state at 76.0 eV is entirely by internal conversion. A 76 eV gamma ray has never been observed. The half-life for this internal conversion decay is approximately 26 minutes. The half-life is not well defined since the chemical environment

affects the internal conversion decay [18–21]. Experiments have measured the energies for the conversion electrons, although there are discrepancies in their values due to the chemical environment of the uranium [21–24].

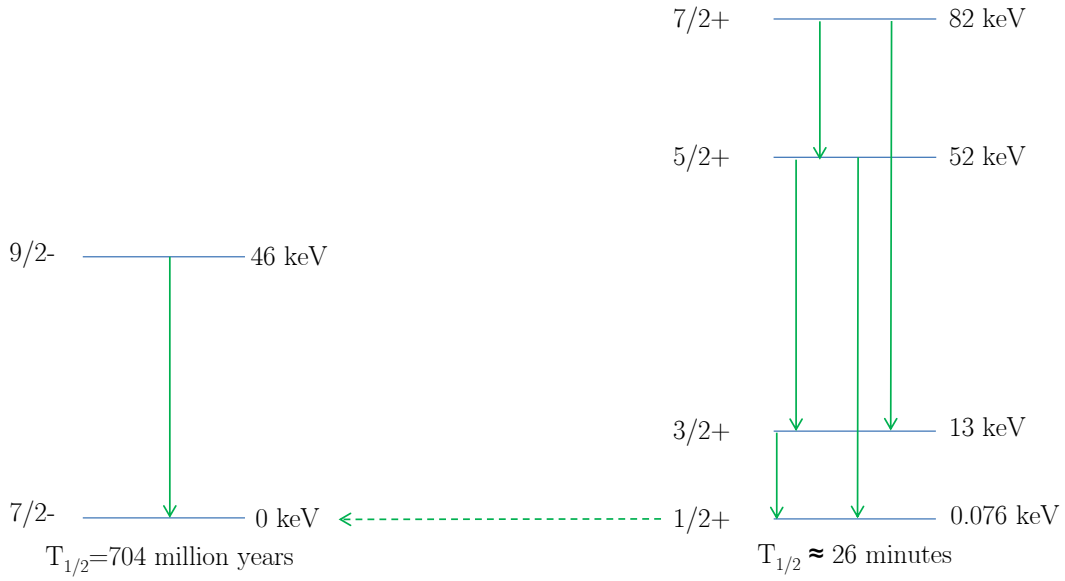

Figure 2.1: ^{235}U level diagram showing the first few excited states with the metastable state on the side. [16]

2.3 Nuclear Excitation by Electronic Transition Theory

Nuclear excitation by electronic transition was first proposed by Masato Morita in 1973 [7]. It is a rare nuclear excitation that involves a coupling between the atomic electrons surrounding the nucleus and the nucleus itself. When an electron in a lower shell is excited to a higher shell, it has many ways of de-exciting. The electron can fall from the higher shell to the lower shell emitting a photon in the form of an x-ray. Another possibility is the energy for the transition is transferred to one of outer electrons causing the ejection of an Auger electron from the atom. NEET would compete with both x-ray and Auger electron emission. In NEET, the transition energy for the atomic transition couples to the nucleus via a virtual photon. This in turn causes the excitation of the nucleus. The nucleus would then de-excite via the nuclear decay modes allowed for the nuclear excited state.

NEET theory has evolved over the past 40 years. Numerous papers have attempted to calculate the NEET rate for various conditions and for various candidate isotopes [7, 25–32]. In addition, numerous experiments have been performed looking for NEET in various isotopes with varying results [33–44]. There are many candidate isotopes with low lying nuclear isomers with energies accessible to electron transition energies [45]. Numerous difficulties exist for predicting NEET rates which are compounded for large nuclei like uranium. At a minimum, NEET theory involves the combination of both atomic and nuclear theory. Not only does the nuclear state have to be correctly modeled, but the electronic states also have to be correctly modeled. While atomic theory can model complex atoms like uranium, some models for NEET also include plasma theory in order to account for electronic configurations in an evolving plasma. The addition of a plasma environment significantly increases the difficulty for modeling the electronic configuration and possible transitions. Since this experiment involves a laser produced plasma, the theory presented here is specific to NEET occurring in a laser produced plasma. Two derivations for the NEET rate in ^{235}U will be discussed. Both derivations make different assumptions in order to calculate the NEET rate. Although the derivations are different, both result in similar predicted NEET rates.

The first derivation presented here was done by M. R. Harston and J. F. Chemin [25]. An important concept for both derivations is the energy mismatch between the two transitions. For NEET to occur, both the electronic and the nuclear transition energies have to overlap. They do not have to exactly match since the states have finite width. This width is broadened from its natural width due to effects such as Doppler broadening and Stark broadening. The degree that the transition energies differ is called the energy mismatch and is defined when the energy mismatch is not zero as

$$\delta_{if} = \Delta E_e - \Delta E_N, \tag{2.4}$$

where ΔE_e is the electron transition energy and ΔE_N is the nuclear transition energy. The NEET excitation rate is defined as

$$\lambda_{NEET} = \sum_q \sum_{if} P^{q,i}(n_e, T)\lambda_A^{q,i}(n_e, T)P_{NEET}^{q,i}(n_e, T), \tag{2.5}$$

where i is the initial atomic state, f is the final atomic state, q is the charge state within the plasma, T is the electron temperature in the plasma, n_e is the electron density in the plasma, $P^{q,i}(n_e, T)$ is the fraction of ions in a specific atomic configuration, $\lambda_A^{q,i}(n_e, T)$ is the atomic transition de-excitation rate, and $P_{NEET}^{q,i}(n_e, T)$ is the probability for the NEET transition to occur. The importance of the energy mismatch is clearly seen when the probability for the NEET transition as laid out in [29] is written as

$$P_{NEET}^{q,i}(n_e, T) = \left(1 + \frac{\Gamma_f}{\Gamma_i}\right) \frac{V_{if}^2}{\delta_{if}^2 + \frac{1}{4}(\Gamma_f + \Gamma_i)^2}, \tag{2.6}$$

where Γ_i and Γ_f are the initial and final atomic state widths, and V_{if} is the matrix element for the nuclear-atomic coupling. If the energy mismatch is large, the probability of NEET

occurring is significantly reduced. In addition, the nuclear-atomic coupling matrix element has a significant role in the probability of NEET occurring. If there is a large mismatch between the atomic wave function and the nuclear wave function, the matrix coupling values are smaller. This mismatch can occur if the nuclear transition has a different multipolarity than the electronic transition.

Two electronic transitions are thought to exist that can couple to the ^{235}U nucleus in order for NEET to occur. The first electronic transition, $6p_{1/2} \rightarrow 5d_{5/2}$, is expected to occur when the uranium is in a charge state of 10+ (U^{10+}). For this case, Harston and Chemin predict four excitation resonances that occur with an energy mismatch of under 4 eV. A second set of resonances is predicted to occur for uranium in a charge state of 23+ (U^{23+}). When uranium is in a charge state of 23+, the dominant electron transition for NEET is expected to be the $6d_{5/2} \rightarrow 6p_{1/2}$ transition. This transition is expected to produce a higher NEET excitation rate. Although the rate is predicted to be higher, the increase in the charge state of the uranium adds difficulty to the measurement. This is because a higher plasma temperature is needed in order to produce U^{23+}. More importantly, both electronic transitions are M2 transitions. This is in contrast to the nuclear transition which is an E3. As mentioned above, the mismatch in multipolarity between the electron and nuclear transitions lowers the probability for NEET to occur.

In order for estimates of the NEET rate to be produced, certain assumptions for the plasma were necessary. The plasma model used was a collisional-radiative model (CR). In this model, there is a homogeneous plasma with the electrons having a single temperature described by a Maxwellian. Both collisional and radiative excitation and recombination in the plasma are taken into account [46]. The reality of a laser produced plasma is much different than what is used for this calculation. A laser produced plasma is not homogenous and there is a time where the electrons and ions do not have the same temperature. In addition, the production of energetic electrons is possible which would create a non-Maxwellian distribution for the electron energies. Regardless of these facts, the plasma used in this calculation does offer some insight into the range of possible excitation rates. The plasma model predicted U^{10+} and U^{23+} dominate at plasma temperatures of 20 eV and 100 eV respectively. In the end, two excitation rate ranges were predicted based on the plasma temperature. The NEET excitation rate for ^{235}U in a 20 eV plasma was theorized to be

$$10^{-9}\ s^{-1} < \lambda_{NEET} < 10^{-4}\ s^{-1}, \tag{2.7}$$

while the NEET excitation rate for a 100 eV plasma was theorized to be

$$10^{-6}\ s^{-1} < \lambda_{NEET} < 1\ s^{-1}. \tag{2.8}$$

The NEET rates presented above have two important features. First, the NEET rate is expected to be significantly larger for the $6d_{5/2} \rightarrow 6p_{1/2}$ transition. This suggests that high plasma temperatures are necessary. It also helps explain the inconsistencies seen in previous measurements that are explained in Section 2.6. More importantly, the predicted NEET rate for ^{235}U spans nearly 10 orders of magnitude. This is an enormous range that suggests

there are not enough data available to accurately make a prediction for NEET of ^{235}U. Nevertheless, these ranges can be used with more accurate plasma models to set upper and lower bounds for the predicted number of isomers produced via NEET.

The second derivation for the NEET rate of ^{235}U was derived by P. Morel et al. [26]. Unlike the previous derivation [25], this paper uses a plasma that is in local thermodynamic equilibrium (LTE). LTE plasma exists when collision induced processes outweigh radiative induced processes and there is a balance between collisional excitation and ionization and their inverse processes [47]. The energy mismatch in the paper, δ, has the same definition as Equation 2.4. The NEET probability, P_{NEET} has a more complicated form than the derivation found in Harston and Chemin. However, the NEET probability reduces to Equation 2.6 over a characteristic time on the order of 10^{-13} s [26]. The two electronic transitions explored in the paper were the same ones explored in [25], the $6d_{5/2} \rightarrow 6p_{1/2}$ transition and the $6p_{1/2} \rightarrow 5d_{5/2}$ transition. Based on their calculations, it was found that uranium in charge states of U^{11+} and U^{21+} yielded the best matching for those electronic transitions. These charge states were similar to ones found in [25]. The difference in predicted charge states could be due to the different plasma model used. It is important to note that the slight difference in required charge states may equate to a large difference in plasma conditions.

Since the energy mismatch depends heavily on the temperature, charge state, and density of the ion, the NEET probability over the plasma time period had to be calculated. This was done using a radiative hydrodynamic Lagrangian bi-dimensional code. The laser used during their simulation had a wavelength of 1.06 μm, a power density of 10^{14} W/cm^2, a pulse length of 1 ns, and a spot size of 1 mm [26]. It should be noted that it was assumed that NEET mostly occurred in the LTE region of the plasma. This region was located near the surface where there was a high density, lower temperature plasma. This calculation did not account for any non-LTE effects or regions. While LTE may be a valid assumption for the dense portion of the plasma, the corona of the plasma plume would not be governed by LTE. The NEET rate equation used was very similar to the earlier derivation. The NEET rate was defined as

$$\lambda^{NEET}(\rho, T_e) = \sum_{\alpha,\beta} P_\alpha(\rho, T_e) \frac{\Gamma_\alpha}{\hbar} \frac{|R_{\alpha\beta}(\delta)|^2}{\delta_{\alpha\beta}^2 + \left(\frac{\Gamma_\alpha + \Gamma_\beta}{2}\right)^2} \left(1 + \frac{\Gamma_\beta}{\Gamma_\alpha}\right), \tag{2.9}$$

where ρ is the density, T_e is the plasma temperature, $P_\alpha(\rho, T_e)$ is the initial configuration probability, Γ_α is the initial atomic width, Γ_β is the final atomic width, and $R_{\alpha\beta}$ is the coupled nuclear-atomic matrix elements. Unlike the earlier derivation, far more electronic configurations were taken into account. The final NEET excitation rate for a single electronic transition is defined as

$$\lambda^{NEET}(\rho, T_e) = \frac{2\pi}{\hbar} D_1 p_1 (1 - p_2) |R_{12}(\bar{\delta})|^2 \frac{1}{\sqrt{2\pi\sigma^2}} e^{-\frac{\delta^2}{2\sigma^2}}, \tag{2.10}$$

where D_1 is the shell degeneracy, p_1 and p_2 are the occupancy probability for a given shell, and σ is the energy variance. The energy variance is defined as "the dispersion of the electronic transition energy of real configurations around the average-atom value"[26].

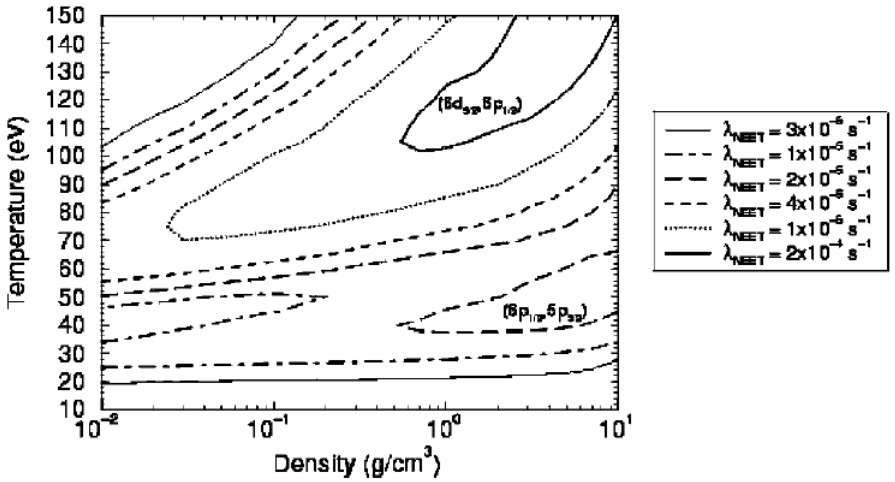

Figure 2.2: Predicted NEET rate of ^{235}U from a laser produced plasma at LTE. Reprinted figure with permission from [26]. Copyright 2004 by the American Physical Society.

Figure 2.2 shows the NEET rate dependence on both temperature and density found in Morel et al. Two islands with larger NEET rates are clearly visible. Comparisons can be made to the NEET rates predicted in [25]. First, the NEET rates calculated in Morel et al. are more constrained. They span only three orders of magnitude. The rates are also in the middle of what was predict by Harston and Chemin. These rates were also calculated using more electronic configurations. However, the LTE assumption may not be accurate for laser produced plasma. Morel et al. cite an LTE criterion described in [48] as justification for LTE. However, while a plasma that has a temperature greater than 30 eV and a density greater than 0.1 g/cm^3 may be considered in LTE, a significant portion of the plasma generated by the laser does not meet that criterion. In addition, hydrodynamic plasma codes have a significant amount of variability in their inputs. Opacity tables, equations of state (EOS), and atomic models can be changed. These changes could yield different plasma with different densities and temperatures. For this reason, it is not known how the predicted NEET rate from Morel et al. varies with plasma data variations. In addition, the plasma generated was created by a specific laser type with specific properties. It is not known how the rates would change with a laser that is either less powerful or has a longer laser pulse. For these reasons it is difficult to fully accept the conclusions for the NEET rate found in Morel et al. While they can be used as a guide for expected NEET rates in laser produced uranium plasma, the plasma situation modeled is specific to a laser with certain characteristics and assumes an LTE plasma which may not be an accurate assumption.

2.4 Laser Plasma Interactions

A general understanding for the laser interaction with the plasma is necessary to fully understand how the plasma temperatures are generated. An important concept within plasma physics is the critical density, which is defined as

$$n_c = \frac{\epsilon_0 m_e}{e^2}\omega^2, \tag{2.11}$$

where ϵ_0 is the permittivity of free space, m_e is the mass of the electron, e is the charge of the electron, and ω is the angular frequency of the photon [49]. The formula can be simplified to

$$n_c = \frac{1.1 \times 10^{21}}{\lambda_\mu^2}\ cm^{-3}, \tag{2.12}$$

where λ_μ is the wavelength of the photon in μm [50]. The critical density of a plasma, sometimes called the cut-off density, defines a point known as the cut-off frequency. Laser light that has a frequency below the cut-off frequency reflects off of a plasma or is partially absorbed. For the lasers discussed in this dissertation, the critical densities are $n_c \approx 9.8\times10^{20}$ cm^{-3} for the Nd:YAG laser at 1.06 μm and $n_c \approx 9.8\times10^{18}$ cm^{-3} for the TEA CO_2 at 10.6 μm. Laser light initially heats the surface of the target generating a plasma. As the plasma grows, the light begins to interact with the plasma. This interaction leads to many physical effects. Many of these effects occur at the critical density for light in the plasma or at a fraction of the critical density. One of the most important effects is resonance absorption. Resonance absorption occurs when the electric vector associated with the laser light is aligned with the density gradient of the plasma. This oscillates electrons in the direction of the density gradient. This in turn generates an electron plasma wave. In essence, the laser light couples to the plasma and transfers energy to the plasma by the generation of a plasma wave. The polarization of the light will be discussed using the convention of s and p-polarized light. Light that is linearly polarized with the electric field vector parallel to the normal vector to the surface is termed p-polarized light. S-polarized light has the electric field vector perpendicular to the normal vector. The laser plasma coupling is strongest for p-polarized light. One can see this by imagining the laser hitting the surface at a small angle of incidence. Most of the resulting plasma leaves the surface in the direction perpendicular to the surface The density gradient for the plasma is strongest in the direction aligned with the normal to the surface. P-polarized light, with its electric field parallel to the normal vector, will strongly couple to the plasma and excite an electron wave. Resonance absorption has an angle dependence due to the electric field alignment condition. For p-polarized light, the strongest absorption occurs for an angle of incidence of between 15° and 25°, where the angle of incidence is defined as the angle between the propagation vector and the normal vector [51–53].

Two other electron plasma waves can be generated by laser light. These plasma waves are caused by plasma instabilities. A plasma instability is an unstable growth of a plasma wave. For this experiment, only electron plasma waves are discussed. One possible plasma

instability is called the Raman instability. For this instability, the laser light inelastically scatters off of the plasma. This results in the generation of an electron plasma wave and scattered light. This form of scattering, called stimulated Raman scattering, can only occur in plasma when $n_e \leq \frac{n_c}{4}$, where n_e is the electron density. The second way an electron plasma wave is generated is by the two plasmon instability. This instability is rarer than the Raman instability. The two plasmon instability is sometimes known as two plasmon decay. For this instability, the laser light is not scattered, but is converted to two electron plasma waves. This occurs in the plasma where $n_e \approx \frac{n_c}{4}$. Both instabilities along with resonance absorption generate electron plasma waves. Electron plasma waves will damp and their energy gets transferred to particles within the plasma. This transfer of energy to particles causes the generation of high energy electrons called hot electrons. Resonance absorption is the largest contributor to hot electron production [54].

Hot electrons, also known as suprathermal electrons, are high energy electrons produced in plasma due to laser-plasma interactions. These hot electrons have temperatures in the keV regime for laser-plasma produced with lasers with energy densities between 10^{12} to 10^{15} W/cm^2. Hot electron properties are described in numerous papers along with empirical formulas to predict hot electron temperatures [50, 55–57]. One such formula for the temperature of these hot electrons is

$$T_e = 1.7(I_{14}\lambda_\mu^2)^{2/3}\ keV, \tag{2.13}$$

where I_{14} is the laser power density in W/cm^2 divided by 10^{14}, and λ_μ is the laser wavelength in microns [50]. Using the fundamental wavelength of a Nd:YAG laser at 1.06 μm and a power density of 10^{14}, the temperature of hot electrons is approximately 1.8 keV. It should be noted that a different formulas for hot electrons produce a value that is 4 keV for a laser with an intensity of 10^{14} W/cm^2 and 1.7 keV for a laser with an intensity of 10^{13} W/cm^2 [26]. It is clear that the equations used to predict hot electron temperatures are not consistent. However, they do offer an estimate for the temperature of the hot electrons generated by resonance absorption. Hot electrons with a mean temperature in the low keV region will have a high energy tail near 13 keV. The number of electrons with energies greater than 13 keV is important to know if one wants to exclude other reactions that can produce the isomeric state. It should also be noted that hot electrons produce an electron temperature distribution that is not a Maxwellian. A Maxwellian distribution was assumed for the electron temperatures for both NEET derivations.

2.5 Competing Reactions

NEET is not the only reaction that can excite ^{235}U into its isomeric state. In fact, the most common production method for ^{235m}U is from the alpha decay of ^{239}Pu. For this experiment, three other competing reactions that can excite ^{235m}U exist. These reactions are photoexcitation, inelastic electron scattering, and nuclear excitation by electron capture (NEEC). Due to the extremely narrow natural linewidth for the ^{235}U isomeric state, approximately 10^{-19} eV, the likelihood of these reactions directly populating the isomeric state is

very small. However, the second excited state at 13 keV directly feeds the isomeric state. The linewidth for this state, $\approx 10^{-6}$ eV, is significantly larger than the isomeric state and these competing reactions could directly excite the second excited state which would then decay to the isomeric state.

As mentioned earlier, photoexcitation of the isomeric state is unlikely. This is clearly seen when one calculates the photoexcitation cross section. The photoexcitation cross section can be calculated using the equation

$$\sigma(E_\gamma) = \frac{\pi}{2}\frac{2I_e+1}{2I_i+1}\lambda^2\frac{\Gamma_\gamma\Gamma_t}{(E_\gamma - E_N)^2 + \Gamma_t^2/4}, \tag{2.14}$$

where I_e and I_i are the nuclear spins for the excited state and initial state respectively, λ is the transition wavelength, Γ_γ is the gamma decay width, Γ_t is the total decay width, E_γ is the photon energy, and E_N is the excitation energy [25]. In the case of the isomeric state, both Γ_t and Γ_γ are very small numbers. This is also true for the first excited state at 13 keV. Calculations for the excitation rate of the isomeric state due to photoexcitation of higher lying states yield a rate of less than 10^{-17} s^{-1} [25]. This predicted rate assumes a laser plasma with a plasma temperature of approximately 100 eV. These conditions are similar to those predicted for this experiment. The photoexcitation rate is significantly less than the excitation rate predicted for NEET. However, the 100 eV plasma temperature does not account for hot electron production within the plasma. These electrons are significantly more energetic than the electron temperature distribution used to calculate the photoexcitation rate found in [25]. The production of hot electrons must be prevented in order to keep the photoexcitation rate small. This is difficult since one needs a laser powerful enough to generate a 100 eV plasma while not having a power density high enough to generate hot electrons. One possible solution is by having the laser light polarized in such a way to prevent the resonance condition that generates hot electrons. This can be done by having the laser light be mostly s-polarized. While it would not completely eliminate resonance absorption, it would minimize it.

Another possible reaction that can create the isomeric state in ^{235}U is inelastic electron scattering (IES). Previous ^{235}U NEET experiments had to contend with high energy electrons. In the case of a laser produced plasma with a temperature of approximately 100 eV, there are not enough high energy electrons to excite the isomeric state. An estimate for the excitation rate within a 100 eV plasma was done by [25] and resulted in an excitation rate of approximately 10^{-16} s^{-1}. This is a very small excitation rate that is orders of magnitude smaller than the predicted NEET rates. Once again, the predicted excitation rate fails to account for hot electrons produced by resonance absorption in the plasma. The issue of hot electrons changing the inelastic electron scattering rate was discussed in [26]. High energy electrons may excite the second excited state at 13 keV. Assuming a laser intensity of 10^{14} W/cm^2, it was found that there would be little change to the inelastic electron scattering excitation rate found in 100 eV plasma. This was attributed to the difficulty of exciting the nucleus from the ground state to the second excited state with an M2 transition.

The most probable competing reaction that could generate the isomeric state is NEEC. NEEC of ^{235}U is described in [25, 26, 58]. While NEET is equivalent to inverse bound internal conversion, NEEC can be considered the inverse of internal conversion. Instead of having an electronic transition from a bound state to another bound state, NEEC involves the capture of a free electron. Predicted NEEC excitation rates for ^{235}U can be found in [25] and [26]. These rates vary depending on the plasma conditions and the theory used to derive the rate. The NEEC rate reported in the Harston and Chemin paper for a laser produced uranium plasma was of order 10^{-11} s^{-1} [25]. This rate is smaller than the lower end of the predicted NEET rate of 10^{-9} s^{-1}. For the LTE plasma used by Morel et al., the NEEC rate was never larger than 10^{-6} s^{-1}. This value is smaller than the their predicted NEET rate shown in Figure 2.2. Table 2.2 shows the theoretical excitation rates for the reactions within a plasma that can excite ^{235}U to its isomeric state.

	NEET rate (s^{-1})	Photoexcitation rate (s^{-1})	IES rate (s^{-1})	NEEC rate (s^{-1})
Harston and Chemin [25]	$10^{-9} - 1$	$< 10^{-17}$	$10^{-17} - 10^{-16}$	10^{-11}
Morel et al. [26]	$10^{-6} - 10^{-4}$	6×10^{-25}	–	$< 10^{-6}$

Table 2.2: Theoretical excitation rates for the reactions that can generate ^{235m}U within a plasma.

2.6 Previous ^{235}U NEET Experiments

Over the past forty years, three experiments have attempted to measure NEET of ^{235}U. These experiments have yielded conflicting results. All three of the research groups attempted to make a uranium plasma using a high power laser. One group additionally attempted to create a uranium plasma using an electron beam. This section describes in detail those three experiments. Explanations for the claimed observations of NEET or the lack of observations are given.

2.6.1 CO_2 Laser Experiment

The very first experiment looking for NEET of ^{235}U was done in 1979 by Izawa and Yamanaka [33, 34]. Using a TEA CO_2 laser operating at 10.6 μm, a metallic sample of natural uranium was irradiated with 100 ns long pulses with a pulse energy of 1 J. After 100 laser pulses on target, the electrons coming from the target were measured using a channel electron multiplier. A grid with a retarding potential was in front of the detector in order to ascertain if low energy electrons were the source for any decay observed. A decay curve

was observed from their experiment. The decay curve had both a fast, $t_{1/2} = 1.0 \pm 0.1$ min., and a slow component, $t_{1/2} = 25.7 \pm 0.4$ min., along with a background. The fast decay was thought to be due to alpha emission from the other uranium isotopes evaporated from the target that were not collected on the collection plate. The background was attributed to alpha emission from the uranium ions that were on the collection plate. By biasing the grid to 90 V, the slow decay disappeared. The electrons creating the slow decay were attributed to the decay of ^{235m}U. An attempt to estimate the cross section for the reaction was done using numerous assumptions about the uranium plasma generated. The main plasma assumption being the electron density where the reaction occurs is the cut off density for the laser used. For a CO_2 laser, the cut off density is approximately $n_e = 10^{19}\,cm^{-3}$. They calculated a Maxwellian averaged cross section of $< \sigma_N v >= 1.4 \times 10^{-20}\,cm^3/s$. In addition to using a CO_2 laser, an experiment was done using a Nd:YAG laser. The 1.06 μm wavelength for the Nd:YAG laser allows the laser to penetrate deeper into the plasma. The cut off density for a Nd:YAG laser is approximately $n_e = 10^{21}\,cm^{-3}$. Using the Nd:YAG laser, the production of ^{235m}U via NEET was larger than the amount created using the CO_2 laser.

The conclusion that the experiment saw NEET in ^{235}U was premature. The explanation for the fast decaying component being due to α emission from uranium isotopes evaporated off of the target is unlikely. Ablated uranium not caught by their catcher plate would plate onto other surfaces quickly. In addition, the total mass ablated by the laser shots was a few hundred nanograms up to a couple of micrograms. The activity for 1 μg of natural uranium is 0.03 Bq. That low activity would not account for the order of magnitude increase in counts shown in their paper. The half-lives for both ^{238}U and ^{234}U are also significantly longer than one minute. Alpha decay of the ablated uranium does not explain the fast decay. There are two possible explanations for the fast decaying component. Laser light and the UV photons generated by the plasma could possibly cause the channeltron detector used during the experiment to fluoresce. This effect would decay with time and be the cause for not only the fast decay observed, but it may explain the longer decay. The fast decay may also be due to exoelectrons. Exoelectrons are low energy electrons released by surfaces that have undergone some form of disturbance. This disturbance can be irradiation by light, irradiation by particles, vacuum changes, and heating of the surface. A thorough description of exoelectrons can be found in [59]. The low energy exoelectron emissions have half-lives that depend on surface material, oxide layers, temperature, and pressure. For this experiment, the catcher plate and the chamber itself were bombarded by electrons, ions and intense light. Both the fast and slow components could be attributed to exoelectrons. The 25.7 minute decay observed, while similar to the expected half-life of ^{235m}U, may in fact be a coincidental value that is actually due to exoelectrons. The only information known about the electrons being measured was that they had an energy less than 90 eV. Exoelectrons, with energies of a few eV, cannot be excluded as the source of both the fast and slow decay components.

A separate issue for this experiment were the plasma conditions assumed for the calculations. First, it was assumed that the electron density for the plasma was equivalent to the cut off density. In the case of light from a CO_2 laser at 10.6 μm, the cut off density is

approximately $9.8 \times 10^{18}\text{cm}^{-3}$. The higher density region of the plasma would have a lower electron temperature. This lower temperature would mean that the probability of NEET occurring would be lower. However, this assumption only works if one assumes that the temperature desired is the plasma temperature at the critical density. This was not known and no explanation was given for why they assumed the temperature was correct at the critical density. In addition, a plasma generated by a laser would consist of a range of densities and temperatures. One cannot assume a homogenous plasma with the same density and temperature throughout. A volume for the plasma was also given. No explanation was provided for how that value was determined. The ion density was assumed to be equivalent to the electron density. This yielded an ion density for ^{235}U that was 140 times less than the electron density due to the low abundance of ^{235}U found in natural uranium. This assumption for the ion density also ignored multiply ionized uranium. It is unlikely the uranium would have been only singly ionized. Higher levels of ionization would decrease the value of n, the ion density. The equation used to determine the NEET cross section was

$$N = n_e n V < \sigma_N \nu > \Delta t, \tag{2.15}$$

where N is the number of isomers produced per laser pulse, n_e is the electron density, n is the ^{235}U density, V is the volume of the plasma, σ_N is the NEET cross section, ν is the electron density, and Δt is the laser pulse length. Almost all of the values used in this equation were dubious assumptions. Thus it is difficult to accept the value for the NEET cross section determined from the equation assuming the observed signal was in fact NEET. To convert the above cross section to an excitation rate, one can use the equation

$$\lambda = \frac{N}{nV\Delta t}, \tag{2.16}$$

where λ is the excitation rate, N is the number of isomers produced per laser shot, V is the volume of the plasma, and Δt is the pulse width [25]. Using the above parameters, one calculates an excitation rate of approximately 0.14 s^{-1}. Assuming the ion density was smaller due to multiply ionized uranium yields an even higher excitation rate. Based on this information, it is difficult to conclude that NEET was observed during this experiment. The electron signal observed was most likely from exoelectron emission and the assumed plasma conditions would not allow an accurate calculation of the NEET rate.

2.6.2 Electron Beam Experiment

A group based at the I.V. Kurchatov Institute of Atomic Energy attempted to replicate the positive results from the original experiment [35]. Using a 5 J CO_2 laser with a 200 ns pulse width, they irradiated a 6% enriched UO_2 ceramic target. A channel electron multiplier was used as the detector to count internal conversion electrons that would be the signal for NEET. No signal was observed even though the material was enriched in ^{235}U. From this experiment, they concluded the NEET cross section was $\sigma_{\text{NEET}} < 10^{-32}\,\text{cm}^2$. The

lack of observation of a NEET signal can be explained. Let's assume that NEET was in fact observed during the Izawa and Yamanaka experiment. This experiment used a laser that was five times more powerful, but it had a pulse width that was twice as long. The power generated by this laser compared to the earlier experiment was roughly 2.5 times larger. In addition, the sample was enriched to 6%, which is 10 times larger than the previous experiment. Both of these facts would make it seem like the confirmation experiment would clearly see a NEET signal. The lack of signal could be attributed to the plasma conditions created by the laser. The NEET rate in ^{235}U is strongly dependent on plasma conditions. Although the enrichment was higher and the laser was more powerful, the focusing of the laser could have been significantly different than the Izawa and Yamanaka experiment. A difference in spot size would create a different plasma and that in turn would influence how many uranium isomers get produced. This work also mentioned an experiment performed by a different group looking for the excitation of ^{235}U by an electron beam [36]. Using a 600 eV electron beam with a current of 20 mA, a sample of ^{235}U enriched to 99.99% was irradiated for 30 minutes. They found an excitation cross section on the order of $\sigma_e \sim 10^{-32}\,\mathrm{cm}^2$. However, it should be noted that there were large errors in the measured half-lives from the sample. Based on the large error, one cannot conclude the isomer decay was observed.

Due to the inconsistencies in the previous measurements, a different experiment was performed using a relativistic electron beam. An electron beam with electron energies of approximately 500 keV and a beam current of 150 kA was shot at a variety of uranium targets. The beam pulse had a duration of approximately 30 ns. The uranium targets were foils on aluminum backing and had a variety of enrichments spanning depleted uranium (0.003% ^{235}U) to highly enriched uranium (99.99% ^{235}U). After irradiation, the collector was moved in front of a secondary electron channel multiplier to count electrons coming off of the collector. There were five uranium targets and each target had between five and twenty experiments performed on them. Only two of the targets, the ones with 93.4% ^{235}U and 99.99% ^{235}U, showed evidence of a decay. In addition, not all of the experiments on those targets showed evidence of a decay. It should be noted that the half-lives for the decays measured had large uncertainties and their values spanned a range of 17.8 min. $< t_{1/2} <$ 44 min. These half-lives should be compared to the currently accepted value for the half-life of $^{235\mathrm{m}}$U of $t_{1/2} \approx 26$ min. The paper concluded that the decays were due to the decay of $^{235\mathrm{m}}$U based on the measured half-lives, the fact it was only seen in the samples with high enrichment of ^{235}U, and that the decay curve depended on the focusing of the electron beam on the target. An estimate was made for the excitation cross section based on the efficiencies and the experimental data. The estimated excitation cross section for the production of $^{235\mathrm{m}}$U was calculated to be $\sigma_e = 1 \times 10^{-32} - 1 \times 10^{-31}\,\mathrm{cm}^2$.

The question is whether NEET was observed during the electron beam experiment, or were other mechanisms creating the observed decay? In order to compare this experimental result with other results, the predicted cross section was converted to an excitation rate. The conversion yielded an excitation rate of $\lambda_{NEET} = 3 \times 10^{-5}\ \mathrm{s}^{-1}$ [25]. Unlike the laser experiments that used either CO_2 lasers or Nd:YAG lasers, this experiment used a very powerful electron beam. 500 keV electrons have a high enough energy that other mechanisms

could have created the signal observed. Inelastic electron scattering would have been able to populate the higher excited states found in ^{235}U. In addition, photoexcitation of the higher lying states due to the bremsstrahlung from the electron beam could create the isomer. Calculations found in [25] predict excitation rates of approximately $\lambda_{IES} = 10^{-7}$ s^{-1} for inelastic electron scattering and $\lambda_P < 10^{-7}$ s^{-1} for photoexcitation. Both of these predictions do not account for the observed rate. What can be concluded is that whatever created the decay in the sample could not be due to both inelastic electron scattering and photoexcitation. This does not automatically make NEET the prime explanation. Based on the data presented in the paper, it is hard to claim the isomer was produced at all. The two targets that are claimed to show the decay of the isomer are labeled A and D. The paper states that between five and twenty experiments were performed on each target. Yet for target A, only two experiments showed any decay at all. The half-lives measured in those decays had uncertainties of 50%. For the target D, only five experiments showed a decay. The half-lives and the uncertainties for the half-lives for the decay varied significantly for each experiment. The first four experiments for target D were combined to generate an averaged half-life of $T_{1/2} = 24.8 \pm 6.7$ minutes. While this half-life is consistent with the decay of ^{235m}U, no explanation was given for why the fifth experiment on target D was excluded from the combined data. It was claimed that the variation seen between the experiments was directly dependent on the level of focusing for the beam. While that would account for the total number of decaying systems, it does not explain the large variation found in the half-lives. No attempt was made to measure the energy of the electrons being emitted. Without that information, it is difficult to conclude that the isomeric state was created. The possibility of exoelectrons creating the signal does exist. Why exoelectrons were not observed for the lower enriched targets is not known. At best, the electron beam experiment has an inconclusive result.

2.6.3 Nd:YAG Laser Experiment

The most recent experiment searching for NEET of ^{235}U was done in 2004 [37]. A 1 J Nd:YAG laser operating at 1.06 μm was used to irradiate a 93% enriched uranium metal target under vacuum. The target was at a 45° angle and the estimated power density on target was around 10^{13} W/cm^2. The spot size for 80% of the power was estimated to be 50 μm. The number of shots on target was less than 30. This was done to minimize the thickness of the uranium coating on the collection plate. Due to the low energies of electrons from the isomeric decay, a thick layer of uranium would prevent many internal conversion electrons from leaving the catcher plate. The target was translated after each shot so that a clean surface was exposed for each subsequent shot. The collection plate was made of gold and the detection system consisted of a channeltron detector with a biased grid between the detector and the collection plate. In order to reduce electron background, a coincidence circuit was made using silicon detectors and a CsI scintillator. These detectors were used to veto electrons that came from alpha decays in order to reduce the electron background during the experiment. Multi-electron events were seen in their electron multiplier. A cut in

the data was made in order to only accept single electron events. It is important to note that there were two vacuum chambers used during the experiment. One chamber was used for the irradiation, while the other was used for the detection of internal conversion electrons. Following irradiation, the catcher foil was moved to the detection chamber. The vacuum levels within the two chambers were different. Changes in pressure are known to have effects on electron multiplier detectors.

The experiment yielded a result of non-detection. An upper limit was set for the NEET rate. This was done by adding a decay curve to the data and seeing the minimum number of ^{235m}U that can be created and still be seen in the data. This information combined with the estimated number of uranium atoms collected, the detection efficiency, and the width of the laser pulse, allowed for an upper limit for the NEET rate to be calculated. The upper limit was found to be $\lambda_{NEET} < 6 \times 10^{-6}\,\mathrm{s}^{-1}$. Two values used in the calculation for the upper limit warrant further discussion. The first is the laser pulse width. The value used was the FWHM of the laser, approximately 5 ns. It should be noted that the paper does not mention whether the laser FWHM was measured. The value may only be the value for the laser pulse width provided by the laser manufacturer. The second interesting value in the upper NEET rate calculation is the efficiency. This was a difficult measurement to make. The detection efficiency was determined using a ^{239}Pu source since ^{239}Pu decays to ^{235m}U nearly 100% of the time. The difficulty in measuring the efficiency was that the ^{235m}U generated from ^{239}Pu decay has a high recoil energy of approximately 86 keV. This is unlike the ^{235m}U created in the plasma which would have energies of only a few hundred eV. ^{235m}U created from plutonium decay would embed into the catcher material deeper than ^{235m}U coming from a plasma. The electrons from the decay of ^{235m}U deeply embedded in the catcher would not be able to escape. Claverie et al. were able to correct this by slowing the uranium recoils from plutonium decay in nitrogen gas. The gas pressure used was chosen to slow down the uranium recoils to an energy that was similar to the energy expected for the ions in the plasma. Correcting the efficiency due to the bias voltage on the collector yield a detection efficiency of 5%.

Unlike previous experiments, some measurements of the plasma conditions were performed. These measurements at least offer a glimpse of the conditions that yielded this null result. Using a time of flight detector, the ion velocity was measured to be $C_s = (7 \pm 1) \times 10^6\,\mathrm{cm/s}$. Using a simple plasma model, the temperature for the plasma was estimated to be $T = 400 \pm 90$ eV. In addition, a picture was taken of the evolving plasma using a CCD camera and a probe beam. From the picture, the region of the plasma where the electron density was larger than the critical density was estimated to be of order 100 μm [37]. The temperature measurement closely matched the value predicted in earlier plasma simulations. The hydrodynamic simulation predicted a maximum temperature of 400 eV for the plasma. The focal spot size from the simulation was set to a FWHM of 50 μm, which is near the size of the plasma seen using the CCD camera. However, it is difficult to accurately compare the spot size from the plasma simulation and the image taken using the CCD. This is because the image only shows the over dense region of the plasma and not the entire size of the plasma. No measurements were done to measure the actual spot size of the laser. This

is important since the spot size determines the power density for the laser, which in turn determines the main characteristics for the plasma. While it was assumed the power density was of order 10^{13} W/cm^2, no measurements were done to confirm this value. The sensitivity of focal spot size to the position of the focusing lens was not mentioned. Variations in the position of the focusing lens of order 100 μm can vastly change the power density of the laser.

The Nd:YAG laser experiment did not see a NEET signal. Even with a 93% enriched sample and a comparable plasma to the one generated in the Izawa and Yamanaka experiment, no signal was seen. One possible explanation is that the plasma created using the Nd:YAG laser, while comparable to the one created by a CO_2 laser, was different enough to not have NEET occur. As mentioned earlier, the NEET rate is highly dependent on the plasma conditions and slight differences in plasma conditions can result in large differences in the amount of ^{235m}U produced. The other possible explanation for the lack of signal when compared to earlier experiments is that the earlier experiments did not observe NEET. Those experiments either created the isomeric state via competing reactions like inelastic electron scattering, or the observed decay was due to exoelectrons. The problem of exoelectrons was investigated during the Nd:YAG experiment. Following the collection of the plasma, there was evidence of a decay occurring. The decay rate was found to vary depending on the catcher material. The decay was also observed when a gold plasma was collected on a gold catcher plate. This suggests that the source of some of these electrons was not from radioactive decay, but from another mechanism. In addition, it was claimed that the decay was observed to stop when 2 V was applied to the catcher plate. However, the plot supplied in their paper clearly shows a short decay still occurring. The isomeric decay would produce a range of electrons energies with many electrons having a energy above 10 eV. Having the decay disappear with a 2 V wall suggests that the decay is not from the decay of the isomer. Interestingly, the decay seen could not be characterized by a single half-life. Two components were observed with half-lives of 2.9 minutes for the fast component and 25.5 minutes for the slow component [37]. The slow component has a half-life similar to the half-life for ^{235m}U. The similarity of the half-life observed to the half-life of the isomeric state can explain the discrepant results seen in all the previous experiments. It does seem amazingly coincidental that exoelectrons could produce the same signature as the isomeric state.

Chapter 3

Experimental Setup

Chapter 3 covers the scientific equipment used during the experiment. First, the properties of the Nd:YAG laser used during the experiment are discussed. This is followed by descriptions for the various optical configurations used throughout the experiment. The vacuum chamber design is explained along with the internal components. This is followed by a section describing the design and testing of the electrostatic focusing lens and microchannel plate (MCP) detector. Lastly, the electronics used during the experiment are discussed.

3.1 Laser Properties

The laser used for this experiment was a Spectra-Physics Quanta-Ray DCR-2A pulsed Nd:YAG laser. The fundamental wavelength for this laser is 1064 nm. This specific laser does have a harmonic generator that can be used to generate other wavelengths via frequency doubling crystals. During this experiment, only the 1064 nm wavelength was used. 1064 nm is located in the near-infrared (NIR) portion of the electromagnetic spectrum. It is invisible to the naked eye, thus IR laser cards were needed to see where the beam was during tuning and operation. A picture of the laser head with the various parts labeled is shown in Figure 3.1.

The initial population inversion is created by the oscillator. Xenon flash lamps pump the Nd:YAG crystal at a rate of 10 Hz. The reflector is a high reflectivity mirror located past the Pockels cell. The output reflector is a smaller mirror than the reflector that reflects a portion of the light back towards the reflector. This design is essential since the laser cavity is an unstable resonator. Unlike stable resonators that have a low diffraction losses for the beam, an unstable resonator has high diffraction losses. However, the diffracted beam that goes around the output reflector is what becomes the output for the laser itself. This laser has two portions where the Nd:YAG crystal is pumped. The oscillator provides the initial pumping of the rod in order to create the population inversion necessary for lasing. Past the output reflector is a single pass amplifier. The outgoing beam is further amplified before passing through the harmonic generator. When the Q-switch is off, the laser outputs long

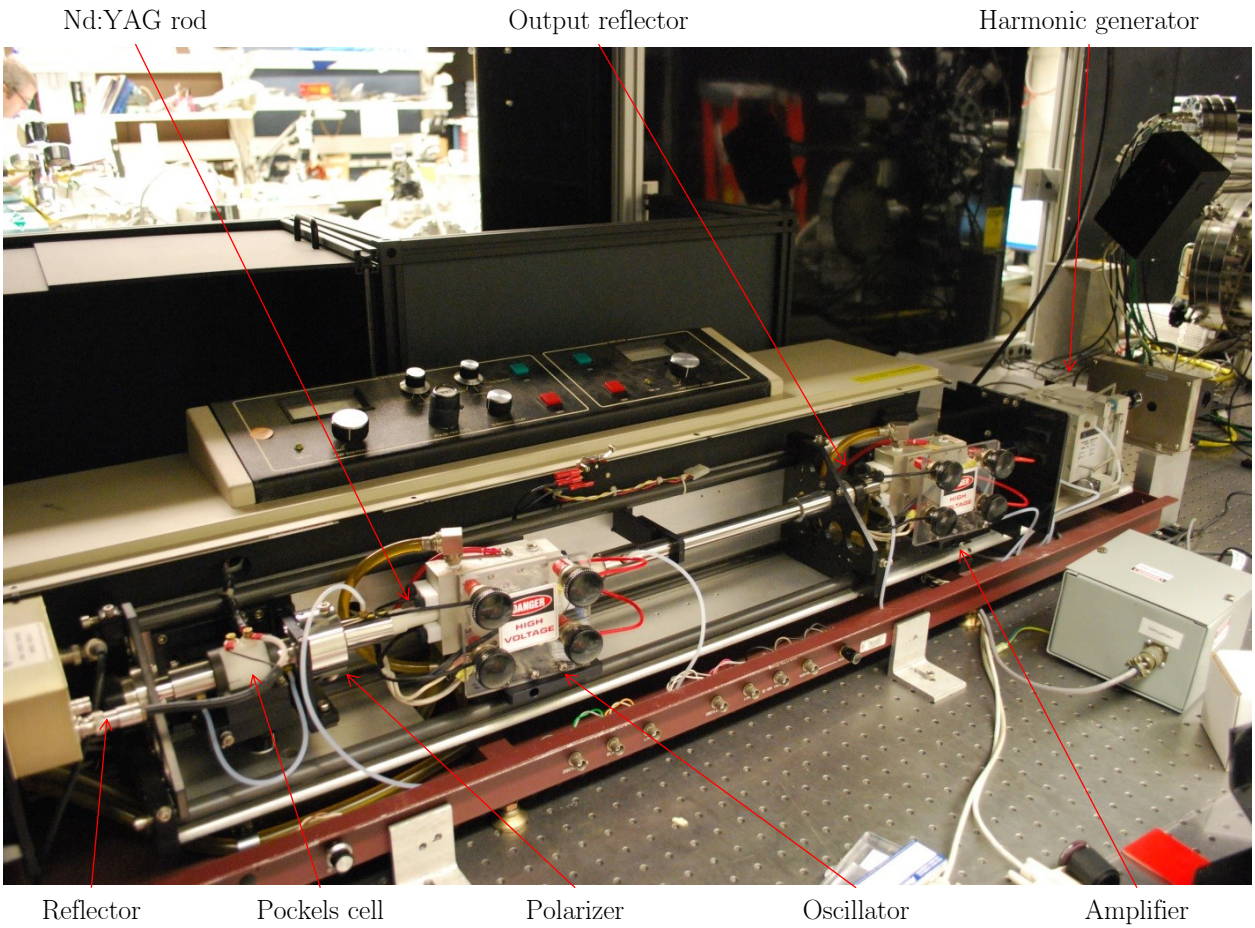

Figure 3.1: Picture of the internal components for the laser. There is an oscillator, an amplifier, a Q-switch, two mirrors and a harmonic generator. The Q-switch consists of both the Pockels cell and the polarizer.

pulses with a FWHM of order 50 μs at a rate of 10 Hz.

This laser can also be Q-switched. Q-switching is a mechanism that allows for very fast, high intensity pulses to be generated. Q is called the quality factor for the lasing medium and it is defined as

$$Q = \frac{2\pi f U}{P}, \tag{3.1}$$

where f is the laser frequency, U is the stored energy, and P is the power dissipated. A high Q factor means there is a lot of stored energy in the system and very little loss, while a low Q factor has high loss and very little energy stored in the lasing medium. In Q-switching, one changes the quality of the lasing medium from low to high. This change is what allows for the high intensity pulse to be generated. Q-switching can be achieved many different ways, for this laser, the Q-switching is achieved by a Pockels cell coupled with a polarizer. This form

of Q-switching is known as active Q-switching since it is externally controlled. A Pockels cell is an electro-optic that becomes birefringent when an electric field is applied. With an applied electric field, the Pockels cell behaves like a quarter-wave plate. The effect on light is described as follows. Vertically polarized light passes through the polaraizer. When it encounters the Pockels cell with an electric field, the light becomes circular polarized if the Pockels cell is oriented at 45°. The light reflects off the reflector back into the Pockels cell where it then becomes horizontally polarized. When the horizontally polarized light encounters the polarizer, it is dumped out of the lasing cavity. The Pockels cell prevents lasing of the cavity when it is on. This is how the Q-switch works. While the flash lamps are pumping the medium, the Pockels cell prevents lasing by causing the light to be dumped out by the polarizer. The Pockels cell turns off quickly allowing for lasing to occur. The population inversion is depleted and you get a short, intense pulse out of the laser [60].

3.1.1 Laser Beam Characterization

Due to the age of the Nd:YAG laser used, it was not known how closely the laser light would match the manufacturer's specifications. All measurements were done using 1064 nm laser light. Numerous tests were performed to characterize the basic properties of the laser light. Two detectors were used for laser characterization and diagnostics. First, a thermal power sensor was used to measure the power output for the laser. The power meter was a Thorlabs S370C power meter, which is designed for high power Nd:YAG lasers. The data from the power meter was readout either from an external display or a program running on a Windows computer. A 5 GHz InGaAs photodetector was also used to measure the beam characteristics during the various tests. The detector used was a Thorlabs DET08C detector, which has a rise and fall time under 70 ps and is sensitive to light from 850-1700 nm. The detector was attached to an oscilloscope in order to measure the temporal pulse shape for the laser pulses. In addition, the photodetector was used to count the total laser pulses produced.

Since it was not known how well aligned the laser cavity was, an initial alignment was performed to increase the laser's output power. Realignment of the laser cavity increased the output power by 10%. While investigating other sources of power loss, it was discovered that the xenon flash lamps were discolored and opaque. Replacement of all four xenon flash lamps increased the power by an additional 10%. Total power output of the laser when in long pulse mode was 10 W. This would equate to 1 J per laser pulse when the laser was at a repetition rate of 10 Hz. However, Q-switching introduces losses to the system that reduces the total pulse energy. In order to measure the pulse energy, the laser's power was reduced. The thermal power meter's damage threshold was lower than maximum pulse power able to be produced by the laser. This was discovered when the original power meter's absorption glass was cracked due to full power shots. For the pulse energy tests, only the oscillator amplifier was operational. This reduced the total power output of the laser to 3.15 W. Turning on Q-switching reduced the power output to 2.63 W. With Q-switching on, the repetition rate of the laser was 10 Hz. This gives an energy per pulse of 263 mJ with only the

oscillator amplifier operating. The reduction in power output suggests that the total power output of the laser while it has the Q-switch on is only 83.5% of full power. To determine the energy per pulse of the laser while both amplifiers were operational, the total output power was measured and then multiplied by 83.5%. With the total non-Q-switch output power being 9.45 W, the energy per pulse for the laser in Q-switch mode was 789 mJ. This compares favorably to the laser manual's value of 800 mJ per pulse.

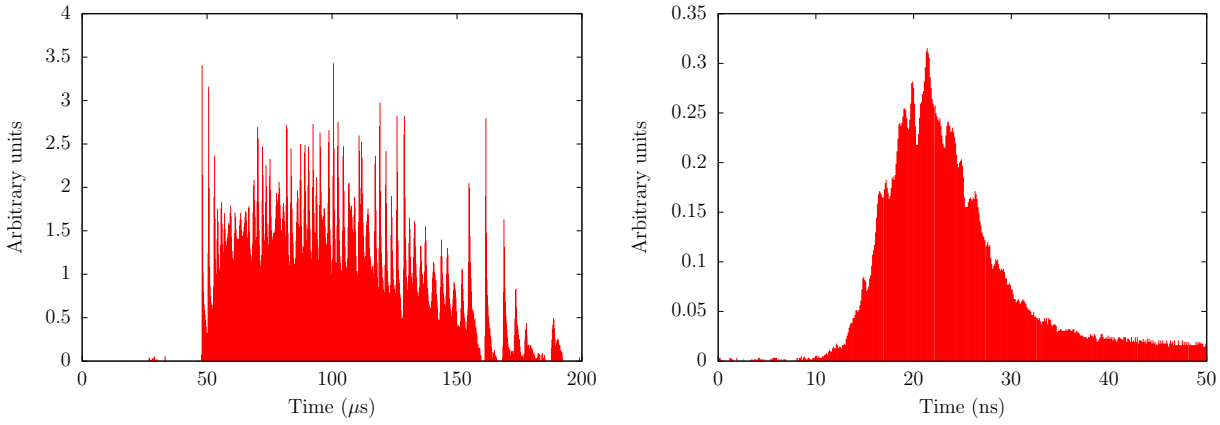

(a) (b)

Figure 3.2: Laser pulse temporal profile. Image (a) shows the temporal profile for the laser pulse with the Q-switch off. Image (b) shows the temporal profile for the laser pulse with the Q-switch on. Note the difference in time scales between the two pulses.

In order to determine the power output of the short laser pulse, the temporal characteristic of the pulse were measured. The InGaAs photodetector was used to measure the light output as a function of time. The fast response time of the detector allowed for a good resolution measurement of both the short pulse and the long pulse. An example for the temporal pulse shape for the laser is shown in Figure 3.2. Part (a) shows the long pulse generated by laser when the Q-switch is not on. These pulses exhibit clear spiking behavior that is common for Nd:YAG lasers. The full width at half maximum (FWHM) of the long pulse is approximately 50 μs. Part (b) shows the short, high-intensity pulse generated when the Q-switch is on. One can see the output is not a smooth, Gaussian like shape. In addition, while the FWHM of the pulse is approximately 9 ns, the total length of the pulse is 30 ns. The laser pulses had different temporal shapes that were nevertheless very similar. Figure 3.3 shows the average temporal shape for the fast laser pulses.

One aspect of the laser light that was difficult to determine was the polarization. A quarter wave plate located before the harmonic generator on the laser allowed for some control over the output polarization. However, it was determined that the laser beam was not linearly polarized but was elliptically polarized. Because of this, the quarter wave plate only offered the ability to either maximize the amount of p-polarized light or s-polarized

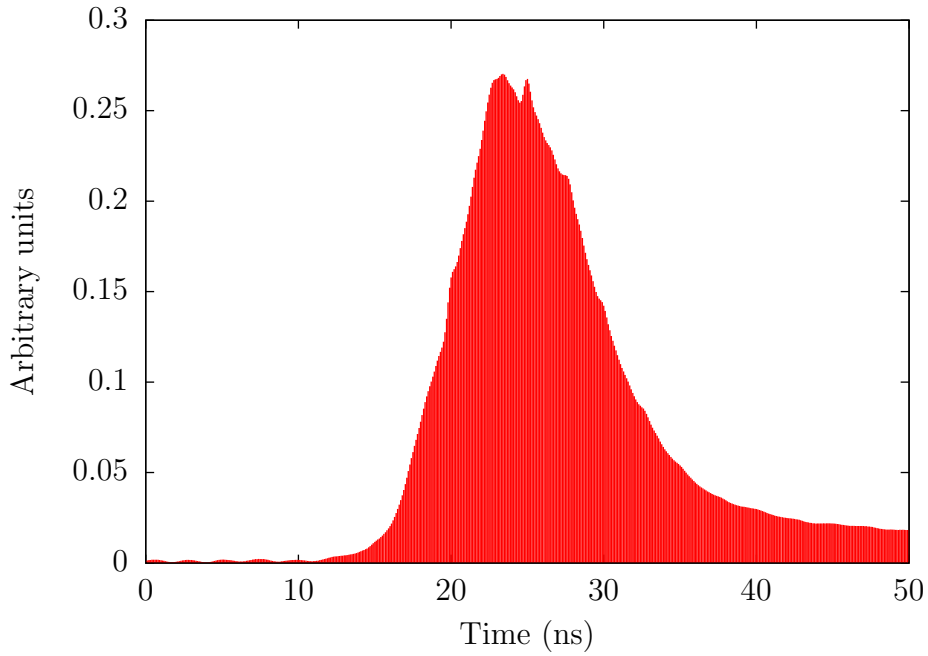

Figure 3.3: Average short pulse temporal profile. The FWHM for the short pulse was calculated using this profile.

light leaving the laser cavity. A polarization plate beam splitter was used to determine the polarization of the laser beam. The beam splitter was a Thorlabs PBSW-1064. It transmits 99.3% of p-polarized light while only transmitting 0.0055% of s-polarized light. By using two power meters, the total amount of p-polarized light compared to s-polarized light was calculated. The quarter wave plate attached to the laser was rotated in order to maximize the amount of s-polarized light. The polarization was initially tested with only the oscillator amplifier on. This test determined that the laser light was 97.2% s-polarized and 2.8% p-polarized. The test was then run with the laser at full power. The results of this test were different than the lower power test. For the full power test, the laser light was 91.5% s-polarized and 8.5% p-polarized. By using the single pass amplifier, the proportion of p-polarized light compared to s-polarized light increased by a factor of three. The addition of the single pass amplifier increases the total power output by a factor of three. This suggests that the single pass amplifier has some effect on the polarization of the beam. The s-polarized light was maximized for the output of the laser during the experiment for two reasons. First, most of the optics were designed to work with s-polarized light. By having the beam be mostly s-polarized, losses due to the partial transmission through mirrors and reflecting off of optical surfaces were minimized. The second benefit for using s-polarized light is that it minimizes resonance absorption.

The final aspect of the laser beam that was characterized was the beam diameter. The manual stated that the laser outputs a 6.4 mm diameter beam. To measure the output beam

diameter, burn paper was used. A full power laser pulse was fired at the burn paper. The resulting burn pattern was measured to determine the beam diameter. A picture of the burn pattern produced can be seen in Figure 3.4. The total diameter of the spot was measured to be 9.8 mm. Assuming a Gaussian beam, this equates to a $1/e^2$ width of approximately 3.2 mm. This value matches the value specified within the laser manual. One aspect of the laser beam not mentioned in the manual was that the beam consisted of numerous laser modes. This produced a pronounced ring structure in the beam. Part (b) of Figure 3.4 shows a burn pattern where the ring structure is clearly visible.

(a) (b)

Figure 3.4: These two images show the laser spot produced on burn paper. Image (a) shows the spot for a single full power laser shot on the burn paper. Image (b) shows the ring structure of the beam.

3.2 Optics

3.2.1 Optical Components

After exiting the laser, the first optical component for all optical layouts was the laser shutter. The laser shutter consisted of the LSTXY-W8-1 laser shutter and CX3000B shutter controller from nmLaser products. The shutter requires power to stay open, thus any power loss to the system closes the shutter. The shutter was controlled by two switches. One switch was on the shutter controller box located next to the laser. This switch allowed for easy control over the shutter from a safe area. The second switch was located on the NIM module for the shutter interlock located in the NIM crate with all the other electronics for the experiment. One of the major optical components used were laser mirrors. The mirrors served multiple purposes. Besides being used to redirect the laser beam, the laser light that was transmitted through the mirrors was used for diagnostics. The initial mirrors used did not have the damage threshold necessary for this experiment. They were damaged by the laser beam after a few uses. These mirrors were replaced by Nd:YAG laser mirrors sold by CVI Melles Griot (Y1-1025-45P). These mirrors had a higher damage threshold and high reflectivity for 1064 nm, s-polarized light. The measured reflectivity for these mirrors using

the Nd:YAG laser's output was 99.9%. These mirrors were 25.4 mm, fused silica glass and were situated in 45° mirror holders.

In order to have a tighter laser beam focus, a beam expander was used to expand the laser beam. Initially, a beam expander made specifically for high power Nd:YAG lasers was used. However, it was damaged by either a back reflection from the focusing lens or by the laser itself. To simplify the design for the beam expander and to more easily repair it if the lenses become damaged, the beam expander was built from individual lenses and not a prebuilt system. The beam expander was a Galilean telescope. This design was chosen since there would be no focusing occurring within the expander lens system. Due to the high power of the laser, any focusing of the laser within the beam expander could lead to air breakdown and damage to the beam expander. The beam expander consisted of two 50.8 mm lenses. Both lenses were made from N-BK7 glass with a C-coating to prevent reflections of the 1064 nm light. The first lens was a plano-convex lens and the second lens was a plano-concave lens with focal lengths of 250 mm and -100 mm respectively. The distance between the lenses was 200 mm. This gave the beam expander an expansion ratio of 2.4X.

The expanded beam was focused using a plano-convex lens. The focusing lens was a 25.4 mm, N-BK7 glass lens with a v-coating to reduce the reflection from the surface. The focal length of the focusing lens depended on the optical setup. The focal length varied from 150 mm up to 400 mm. Multiple laser windows were used during the various experiments. A laser window was needed in order for the laser beam to enter the chamber while the chamber was at vacuum. The laser windows were attached to a 2.75" conflat flange. The windows consisted of 38.1 mm, UV fused silica glass with a C-coating to reduce reflections. Additionally, 25.4 mm laser windows were used in certain setups in order to block material blown off from the target. These windows were 1064 nm v-coated in order to reduce reflections.

The thermal power sensor and the photodetector were used for laser diagnostics. The power meter's position was dictated by which experiment was being performed. For the initial characterization, the laser power meter was located in the direct beam path. For the ablation tests, the power meter was located near the first mirror. It was used to measure the laser power being transmitted through the mirror. This allowed for power measurements while the beam was irradiating a target. The total power of the laser while the beam was irradiating the target was calculated using the equation

$$P_T = \frac{P_M}{9.1 \times 10^{-4}}\,, \tag{3.2}$$

where P_T is the total power of the laser light and P_M is the measured power of the laser light that was partially transmitted through the first mirror. The InGaAs photodetector was attached to an oscilloscope in order to measure the temporal pulse shape for the laser pulses. In addition, the number of laser shots on target was measured by counting how many pulses occurred on the oscilloscope. During the main experimental shots, the photodetector signal was sent to a discriminator and then to an Ortec 875 counter. This allowed for an accurate counting of all laser shots entering the chamber.

3.2.2 Optical Setup

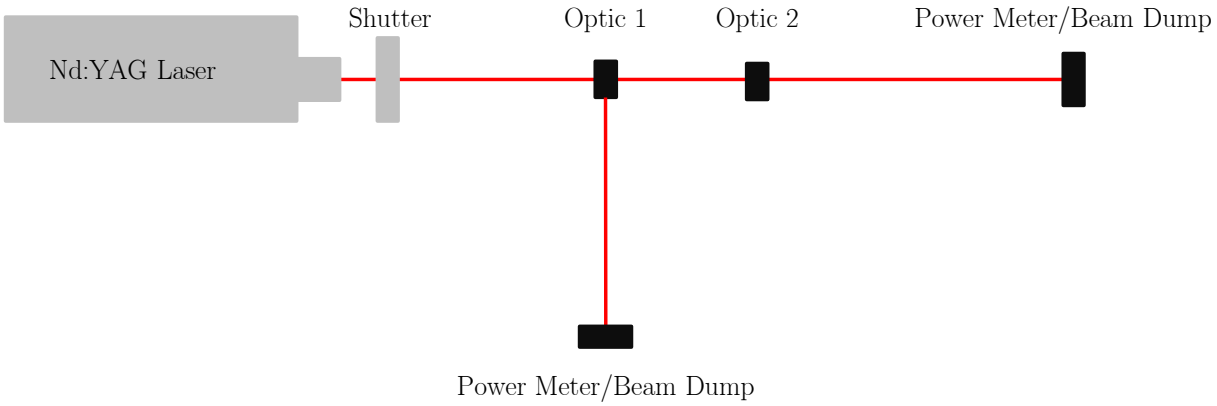

Figure 3.5: Optical setup for laser and optics characterization. Optics were placed at positions one and/or two. The optics were tested using this setup along with the power meters and the photodiode. The laser was also characterized using this setup.

The optical layout used varied depending on the application. There were three layouts that were used consistently. Setup 1 was used for laser and optics characterization. Setup 2 was used for the initial ablation tests. Setup 3 was used for the final ablation tests and the experiment itself. Setup 1 can be seen in Figure 3.5. The laser light exits the laser and goes through the shutter. Following the shutter, multiple optical components were tested. In some cases only one optic was tested with the beam stop being either the power meter or the beam dump. In other cases, two optics were tested with the beam ending in either the power meter or beam dump. In the position for optic 1, some optics that either deflected part of the initial beam or reflected the initial beam were tested. This opened up another beam path that was terminated by a power meter or beam dump. The testing for the photodiode required a small amount of the beam to enter the entrance window. This was achieved by using a piece of white foam. The foam scattered the laser light, thus allowing only a small amount of light to enter the photodiode.

Setup 2 can be seen in Figure 3.6. This optical setup was used to test metal ablation within a test chamber. In addition, this chamber was used to measure the spot size for the laser after it is focused through a plano-convex lens. In this setup, the laser is redirected using two mirrors. The mirrors helped to reduced the risk for back reflection into the laser cavity. The transmitted light through the first mirror is used to measure the power of the laser. The power measurement only worked when the laser was near maximum power since the percentage of transmitted light was small. The transmitted light through the second mirror was blocked using a beam dump. The light was then sent through the beam expander. The expanded beam was incident on a plano-convex focusing lens. The lens was attached to a linear translation stage. A dial indicator was positioned near the translation stage. This

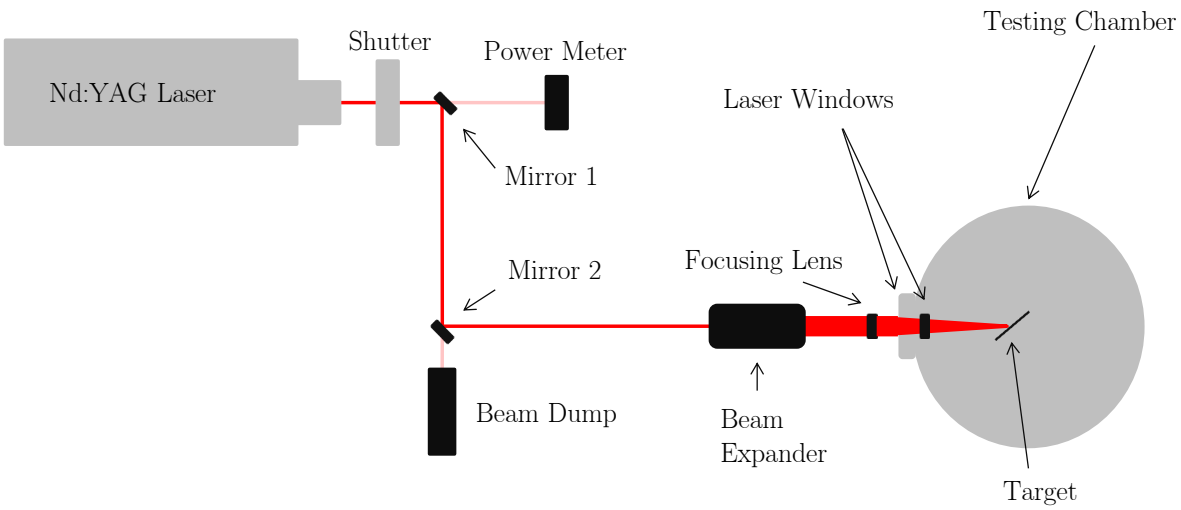

Figure 3.6: Optical setup for ablation measurements. This setup allows for laser ablation experiments to occur in the test chamber. The second laser window in the chamber was used to prevent ablated material from blocking and damaging the entrance laser window.

indicator was used to measure the movement of the translation stage with an accuracy of 0.001". By moving the focusing lens, the spot size on the target would change. The indicator allowed for the focusing lens to be moved a set distance and returned to its original position. Following the focusing lens, the laser entered the chamber through a laser window attached to a 2.75" conflat flange. Inside the chamber there was another laser window before the target. This window was used to block ablated material from embedding into the first laser window.

Setup 3 can be seen in Figure 3.7. This was the optical setup used for the main experiment along with the final laser testing before the main experiment. In this layout, the laser is directed into the main chamber using three mirrors. The three mirrors used were helpful in preventing any back reflections from going into the laser. Similar to setup 2, the transmitted light through mirror 1 and mirror 2 were blocked using the power meter and beam dump respectively. The transmitted light through mirror 3 was incident on white foam. The white foam scattered the light. A small portion of the scattered light was incident on the photodiode detector. This detector was able to measure the temporal shape of the pulse while counting each pulse sent into the chamber. The beam expander was located after the third mirror. A plano-convex focusing lens was after the beam expander. Like setup 2, the focusing lens was attached to a linear translation stage in order to control the spot size and the focal point location. Following the focusing the lens, the laser light entered the chamber through a laser window attached to a 2.75" conflat flange. Unlike setup 2, there was no second laser window within the chamber. The need for the second window was reduced by the placement of a containment box within the chamber. This box was built to contain the

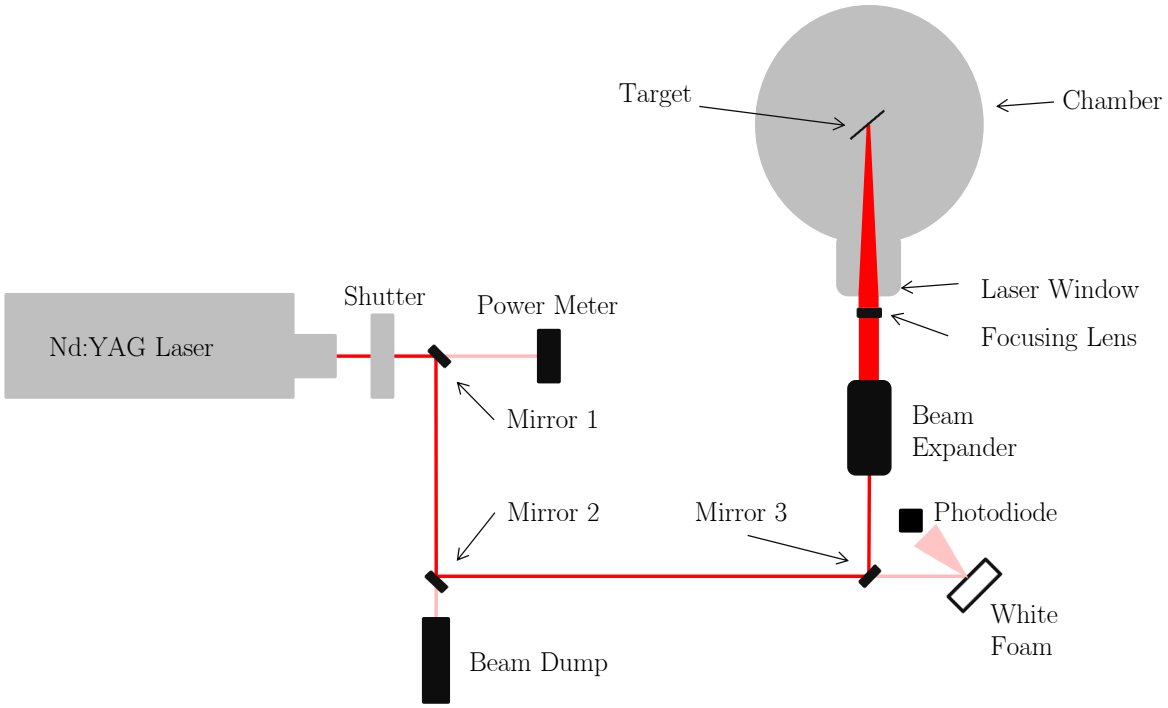

Figure 3.7: Optical setup for the main experiment. This setup allows laser ablation experiments to occur in the main chamber, while allowing for laser diagnostics using the power meter and the photodiode.

ablated material and had a small hole to allow the laser light to enter the box.

3.2.3 FRED Modeling

The program FRED Optical Engineering Software was used to model the laser light path from the laser output until its focal point on target [61]. One major issue during the experiment was optical component failures. It was not known what was causing the various optical lenses to fail. Four reasons for the optical failures were investigated. First, damage threshold of the lenses were investigated. Some of the initial failures were attributed to the laser power being too high through the optical glass. The high peak power density from the Q-switched laser was causing the glass to crack and even leave a burn mark in one component. To prevent this from occurring again, optics with higher damage thresholds were purchased. The second cause for optical damage was thought to be dust on the optics absorbing light and heating the glass. This was controlled by spraying Techspray duster on the optics before turning the laser on. In addition, the optics table was covered by the light box that helped minimize the amount of dust landing on the table. The third possible cause

for optical damage was from hot spots coming out of the laser head. If the laser was brought up to full power too quickly, the output beam would occasionally have hot spots due to the laser rod heating causing some focusing of the light. To ameliorate the problem, the laser was brought up to full power over the course of 10-15 minutes. The optics were not exposed to full power Q-switched laser shots until the laser was fully warmed up. The final possible cause for optical component damage was discovered using the FRED software.

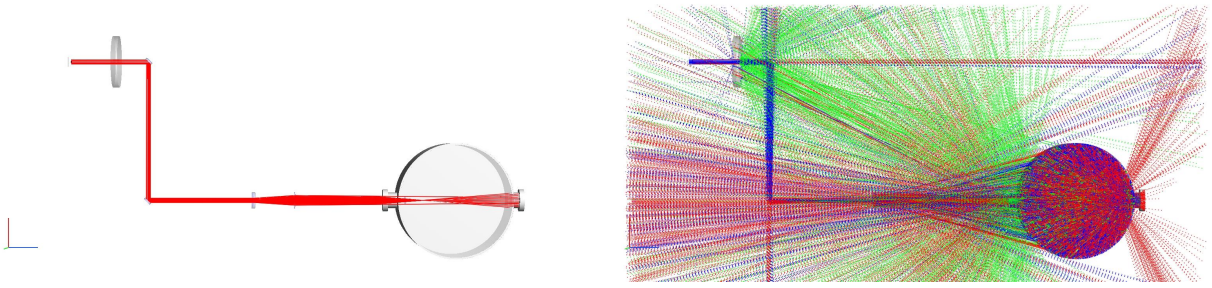

(a) FRED simulation showing beam path (b) FRED simulation showing all light paths

Figure 3.8: Image (a) shows the path of the laser light from the laser head to the test chamber. Image (b) shows the same path with reflections off of surfaces and scattered light turned on. In image (b), red light is transmitted light, blue light is reflected light, and green light is scattered light.

FRED was used to model the optical setup to help determine what may have caused the optics failures. The program allows for the laser light to be modeled along with the optical components and the chamber. FRED uses ray tracing to model how the light propagates and interacts with surfaces. Reflections and scattering of the laser light off of all the parts is included in the model. A benefit of this software is that it allows for various coatings to be applied to the optics. The full optical setup was able to be modeled including all the anti-reflection coatings and the laser characteristics. FRED was used to model Setup 2 that is seen in Figure 3.6. The optical setup modeled by FRED can be seen in Figure 3.8. Image (a) of the figure shows the laser path through the optical setup. For this simulation, only the initial light rays are shown. Light rays generated by reflections off of surfaces or scattering are not allowed to propagate. Image (b) of Figure 3.8 shows the model with the reflections and scattering turned on. It was the reflection data that explained why the optics were often breaking. From the simulation, it was determined that back reflections from the optical surfaces was causing the failures of various components. Although many of the optics had anti-reflection coatings with small reflectance due to the v-coating ($R < 0.2\%$), the small amount of laser power that was back reflected caused significant damage. After the laser light passed through the focusing lens, it encountered the laser window that entered the chamber. The reflectance of the laser window was approximately 0.2%. However, due to the high power of the laser, the back reflection of that small amount of light was focusing approximately 7 cm in front of the focusing lens. The power density of the laser light at this

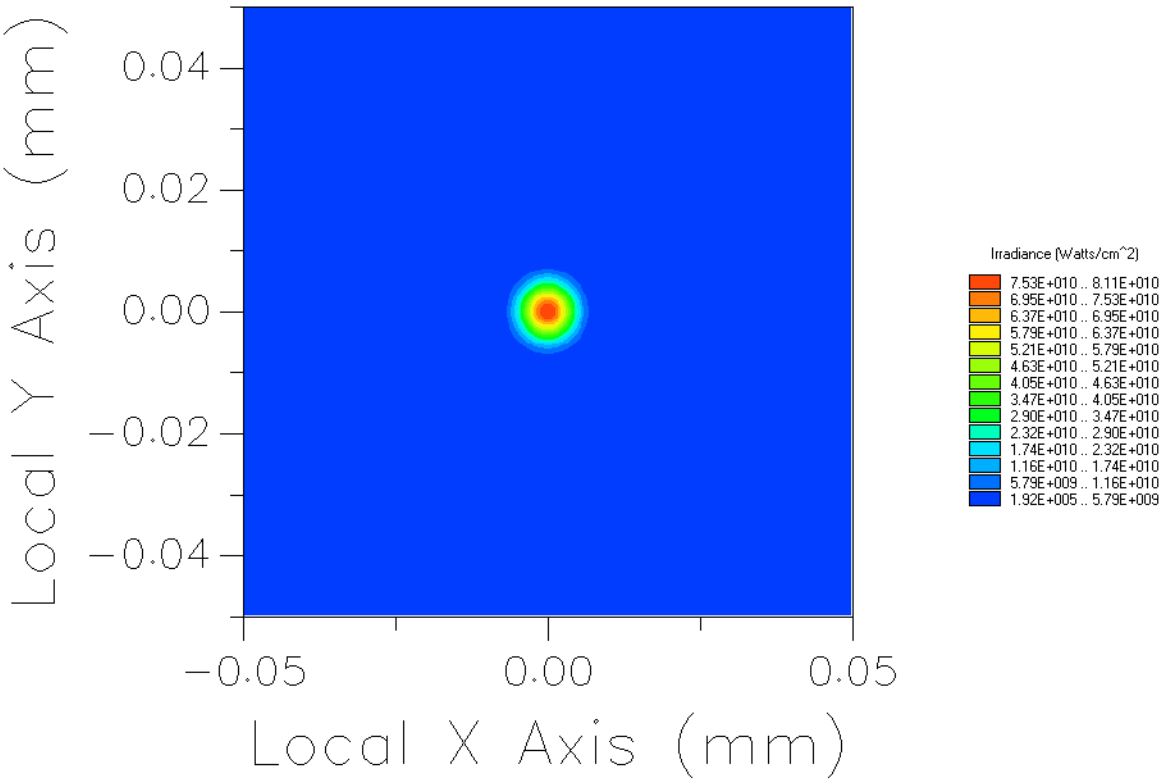

Figure 3.9: FRED calculation showing the intensity of the back reflected laser light at the focal point.

focal point was approximately 10^{10}-10^{11} W/cm^2. Any optic that was near this back focused spot was encountering a laser power density far above its damage threshold. The discovery of this back focused spot led to a change in the optical setup. The optical component that preceded the focusing lens was moved farther away to ensure the back focused spot would not be near the optical surface. Following this fix, no other optical component damaged occurred due to the laser light.

3.3 Experimental Chamber

The experimental chamber for the NEET experiment can be seen in Figure 3.10. The chamber for the experiment was divided into two sections, the lower section and the upper section. The lower section was designed for the laser ablation portion of the experiment. The upper section was the detection part of the chamber. The upper section consisted of a turbomolecular pump, the electrostatic focusing lens, Microchannel plate (MCP) detector, residual gas analyzer (RGA), cold cathode gauge, and linear translation arm. The RGA

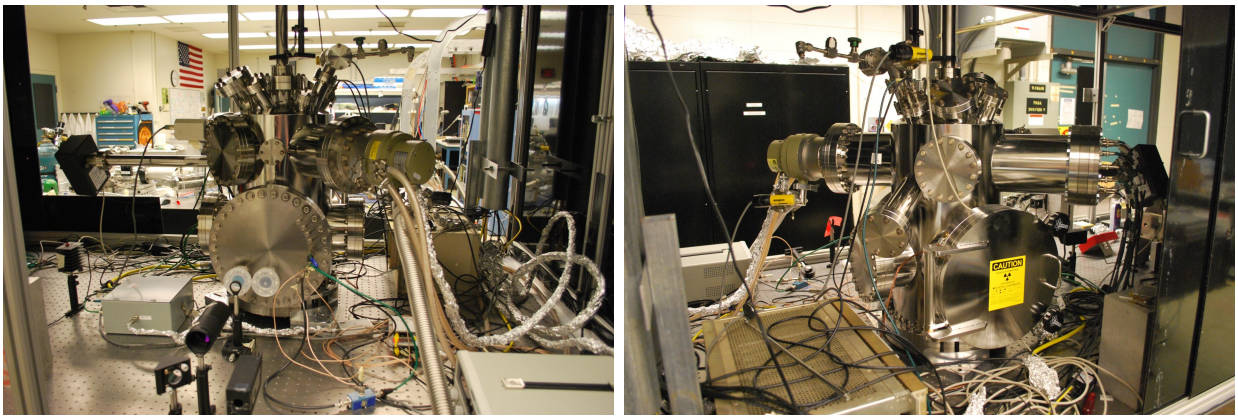

(a) Chamber front (b) Chamber rear

Figure 3.10: Front and rear view of the experimental chamber.

was an Extorr model XT100. It consisted of a Pirani gauge, an ion gauge and quadrupole magnet. The RGA served multiple purposes. First, it was used to measure the pressure within the chamber. Second, it was used for leak detection after the chamber was initially assembled. In addition, the ability to detect ions up to 100 amu allowed for the determination of contaminants within the chamber. The RGA was not run during the laser ablation experiments due to the large number of electrons emitted by the filament. The electrons would overwhelm the MCP detector. An Adixen ACC 2009 cold cathode was also used to measure pressure. The cold cathode was not run during the laser ablation experiments due to the electrons from the cold cathode hitting the MCP. The turbomolecular pump was a Pfeiffer Balzers TPU-170 with a maximum pumping speed of 170 l/s. The pressure was measured with both the RGA and the cold cathode and was $< 5 \times 10^{-7}$ torr after one day of pumping. The electrostatic lens system along with the MCP detector were attached to the chamber via an 8" CF flange. Opposite the electrostatic lens port, the turbomolecular pump was attached. A linear translation arm was attached to the top of the chamber. The translation arm was built by Transfer Engineering and had a travel length up to 24 inches. This translation arm transported the catcher plate from the bottom of the chamber to the top. The total movement time for the arm to move from the collecting position to the detection position was under 10 seconds. The translation arm was encoded allowing for the arm to consistently move between the collecting and detecting positions.

The chamber was divided in half by a carbon layer coated aluminum baffle. The baffle was held in position by two legs and was located approximately 2" from the bottom of the electrostatic rings. The bottom of the baffle was painted with Electrodag 502 paint in order to absorb stray laser light and any light generated by the plasma. A square slot was machined in the center of the baffle to allow the catcher plate and translation arm to move between the top and bottom of the chamber. Attached to the top of the catcher plate assembly

was a sliding aluminum plug. When the catcher assembly was located at the bottom of the chamber, the plug closes the hole in the baffle and prevents light from entering the top portion of the chamber where the detector is located.

The bottom section of the chamber was where the laser ablation portion of the experiment occurred. The bottom section consisted of a laser window, a large O-ring quick entry door, translation stage, target assembly, and containment box. The large door was essential for the experiment. It allowed easy access to the bottom portion of the chamber for quick replacement of targets, catcher plates, and for troubleshooting experimental problems. Two windows were located opposite the quick entry door. One window was the laser window and consisted of a piece of UV fused silica glass with a C-coating to reduce reflections. The other window was a plain window that allowed for viewing of the inside of the chamber. Two Newport 9067 translation stages were attached to each other within the chamber. This allowed for 2 dimensional movement of the target assembly. Since the translation stages were not encoded, a circuit for returning the translation stage to its original position was designed. A small arm was attached to the end of the translation stage. This arm would impinge on a switch keeping it pressed when the translation stage was in its original position. A simple circuit was designed that would cut the power to the translation stage motor when the switch was closed. To allow the translation stage to move again, a switch outside of the chamber was moved to the power position. In this position, the translation stage motor had power even when the switch within the chamber was pressed. To return the translation stage to the starting position, the outside switch was moved to the interlock position. Once the arm impinged on the switch within the chamber, the power to the motor was cut and the translation stage would stop moving.

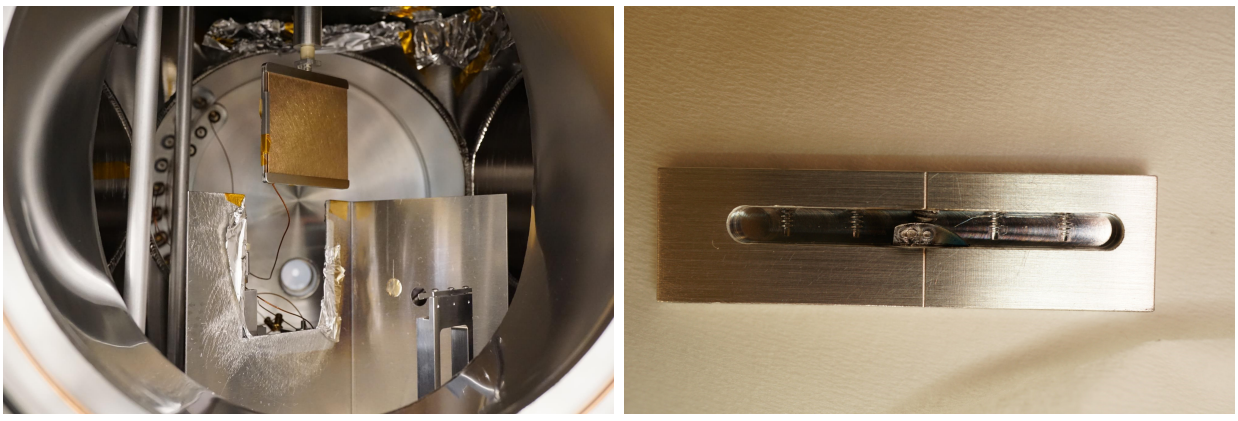

(a) Target assembly (b) Sample holder

Figure 3.11: Image (a) shows the target assembly and half of the containment box. The gold coated copper catcher foil is also visible. Image (b) shows the enriched uranium target post irradiation within the sample holder.

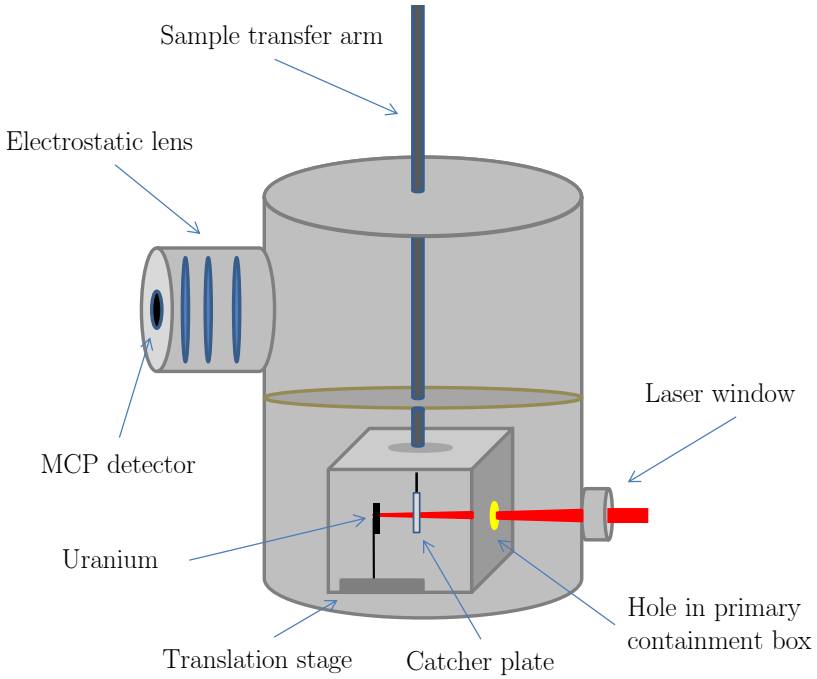

Figure 3.12: Diagram detailing the inside of the experimental chamber.

Attached to the translation stage was the target assembly. The target assembly was designed to hold various samples. This was achieved by having a variety of sample holders with the same dimensions. The target assembly attached to the translation stage and an example sample holder can be seen in Figure 3.11. Sample holders were designed to either hold irregular shaped metal pieces or samples in the shape of a puck. Surrounding the target holder in the chamber was an aluminum containment box. The box was designed to allow the laser to enter the box and for the catcher plate to move into the box from the top of the chamber. This box served two purposes. First, it was to contain any ablated uranium that was not caught on the catcher plate. This was to prevent contamination of the chamber and of other pieces of equipment within the chamber. The containment box was also meant to contain the light from the laser and the resulting plasma. It was originally thought that the box would have been sufficient to block the light from the detector in the top portion of the chamber. However, after numerous tests it was determined that too much light was escaping the box and causing the detector to register a signal. The aluminum baffle was machined in order to correct for this problem. A diagram showing the configuration within the experimental chamber is shown in Figure 3.12.

3.4 Electrostatic Lens

In order to accelerate and focus the internal conversion electrons from the ^{235m}U decay, an electrostatic lens system was built. The lens served two purposes. First, to accelerate the electrons coming from the catcher plate. The internal conversion electrons have very low energy, less than 77 eV. The efficiency of microchannel plate detectors varies depending on the energy of electrons striking it along with the angle of incidence. For electrons with the energy between 200 eV and 2000 eV, the detection efficiency is between 50% and 80%. Higher energy electrons, between 2 keV and 50 keV, have an efficiency between 10% and 60% [62]. The highest efficiencies occur at electron energies between 500 eV and 4 keV [63, 64]. The lens was designed to accelerate the internal conversion electrons to approximately 1.5 keV by the time they hit the detector. The second purpose for the lens system was to help focus the internal conversion electrons onto the detector while preventing background electrons from hitting the detector. The catcher plate was located 28 cm from the detector face. Without a focusing system, electrons coming off of the catcher plate would have a small probability of hitting the detector due to the small solid angle coverage. In addition, electrons in the chamber that are not coming off of the catcher plate could reach the detector and add a steady background to the experiment. The lens system was designed to repel electrons that are outside of the lenses and electrons that are not coming from the catcher plate.

The lens system consisted of 5 metal electrode rings and 1 metal grid ring. The rings were attached together by insulating, ceramic posts. This allowed each ring to be biased to a different electric potential. The final ring was attached by ceramic posts to an aluminum pedestal. This pedestal also had the microchannel plate detector attached to it. The pedestal was attached to an 8" CF flange. Twelve SHV feedthroughs were attached to the 8" flange. All of the wiring for the lens and the MCP detector was attached to the pins on the flange. This allowed the entire lens system including the MCP detector to be inserted into the chamber as one piece. A picture of this setup can be seen in Figure 3.13. Ring 1 and ring 5 were 25 mm in length, while Rings 2-4 were 40 mm in length. The lens grid consisted of a metal mesh with 30 wires per inch and an open area of approximately 93%. Rings 1, 2 and 5 were kept at a negative potential. Ring 1 and ring 2 had a negative potential in order to prevent outside electrons from entering the system along with helping to focus electrons towards the center of the ring. Ring 5 had a negative potential in order to help focus the electrons onto the microchannel plate detector. Ring 3 was held at a large positive potential. Ring 4 was kept at ground. To determine the optimal potentials, the program SIMION was used.

3.4.1 SIMION

SIMION is a charged particle simulation software [65]. It was used to help optimize the electrostatic lens system in order to achieve the highest efficiency possible for electrons coming off of the catcher plate. The chamber was modeled within the program along with the entire lens system and the microchannel plate detector. Figure 3.14 shows both a 3D

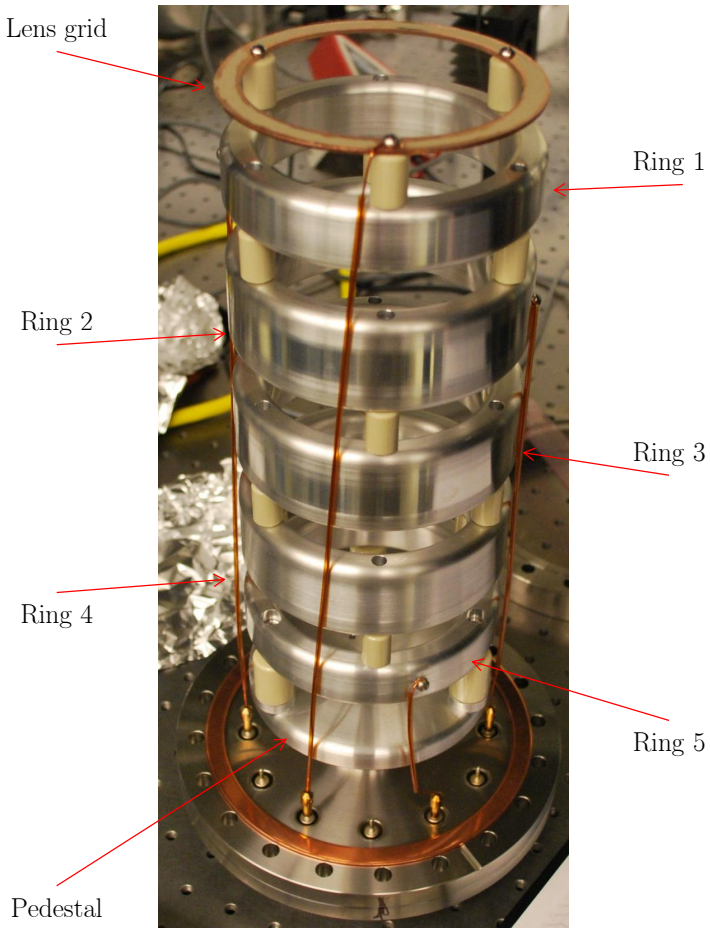

Figure 3.13: The electrostatic lens system. Five aluminum rings along with a mesh grid are attached to a pedestal that holds the MCP detector. The rings were biased in order to focus and accelerate internal conversion electrons coming from the catcher plate.

cutaway of the simulated chamber along with a cross section of the lens system. Electrons were programed to start on the catcher plate and fly off at energies between 0.025 eV and 77 eV. By varying the voltages on each of the rings, one can observe the changes in electron trajectories coming off of the catcher plate. The difficulty with this design was allowing for higher energy electrons from the catcher plate to reach the detector while simultaneously preventing low energy electrons from the catcher plate and the chamber itself from reaching the detector. In addition, since the electron energy spectrum from ^{235m}U was not known, an approximate electron distribution was made. The electron distribution used was a Gaussian distribution of electron energies centered at 40 eV with a FWHM of 10 eV.

In order to optimize the lens system, a program was written using the programming language Lua to test multiple lens parameters. The percent of electrons from the catcher plate hitting the microchannel plate detector was recorded along with the lens potentials.

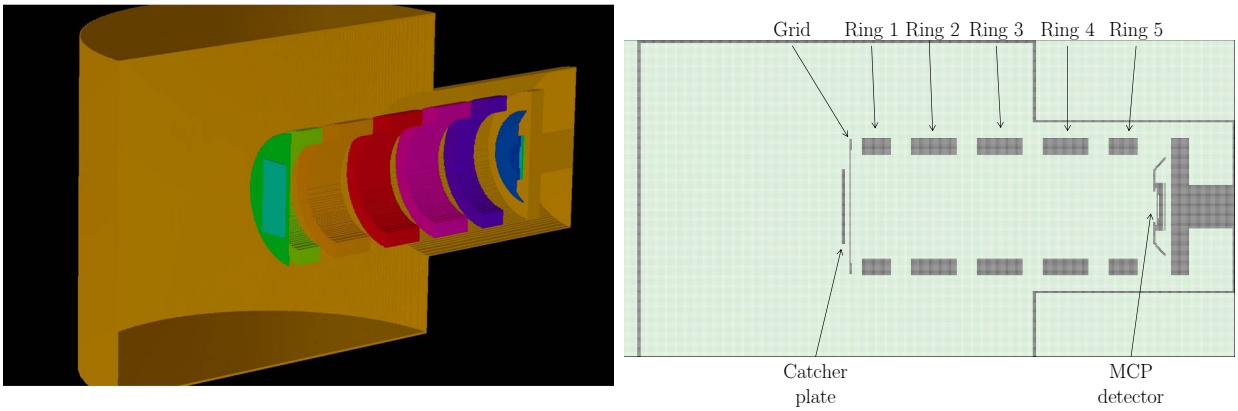

(a) 3D image (b) Cross section

Figure 3.14: SIMION simulation for the electrostatic lens design. Image (a) shows a 3D picture of the chamber and lens system cut in half to display the various components. Image (b) shows a cross section for the lens system.

Based on the results of this program, the optimal ring potentials were determined. These potentials were then tested using a ^{239}Pu source, which is explained in detail in 3.4.2. To prevent the low energy electrons originating on the catcher plate from reaching the detector, a small positive potential on the catcher was required. For the experiment, the catcher was held at 4 V. Following the catcher, a grid potential held at ground was used. By grounding the grid, the electric field from the rings was prevented from affecting electrons on and near the catcher. During the experiment, Ring 1 was held at -30 V. This served two purposes. First, it helped bend electrons coming from the catcher plate towards the center of the lens system. Second, it helped repel electrons from outside the lens system. The simulation suggested that Ring 1 should have been set to -20 V. It was discovered that setting the ring to that potential increased the background rate in the detector. The increase in efficiency was matched by the increase in background. Therefore, there was no change in the signal to noise ratio. Because of this, Ring 1 was set to -30 V. Ring 2 was held at a -5 V. Ring 2 being at at a small negative potential caused the largest reduction in background counts in the detector.

The most important ring in the electrostatic lens was Ring 3. Interestingly, the simulation suggested that a high positive voltage on Ring 3 was needed to increase the efficiency of the lens system. This at first appeared counterintuitive. Earlier tests using ^{235m}U created by a ^{239}Pu source to measure the effectiveness of the ring system showed that high positive voltage on Ring 3 or Ring 4 attracted all the electrons. Even a couple of hundred volts on Ring 3 severally diminished the signal. The electrons within the lens system only have tens of eV of energy and it was not surprising that a large positive potential on one ring would attract

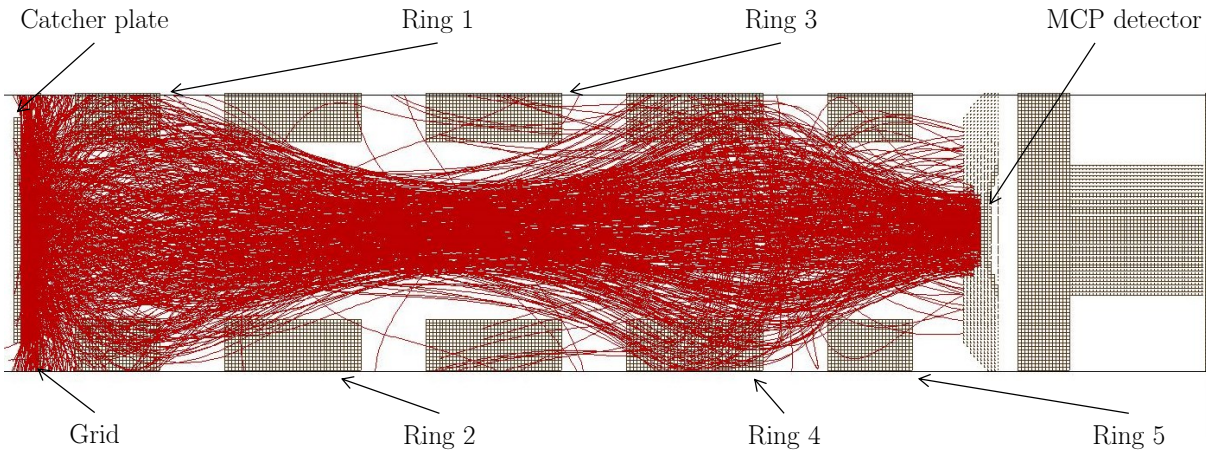

Figure 3.15: SIMION simulation of the electron trajectories from the catcher plate to the MCP detector. Although the simulation makes it appear that electrons are moving through the metal electrodes, they are in fact stopped when they hit the electrodes.

the electrons and prevent them from hitting the detector. However, these earlier tests had significantly different voltages on the catcher, grid and first two rings. The simulation was suggesting that Ring 3 should be set to 3000 V. To test this, a variety of voltages between 0 V to 3200 V were applied to Ring 3 and the count rates in the detector were measured. These tests demonstrated that 3000 V on Ring 3 does in fact help to focus and accelerate electrons towards the MCP detector. Ring 4 was held at ground. No voltage on Ring 4 was shown to increase the ability of electrons to reach the detector. The final ring, Ring 5, was set to -140 V. The negative potential helped to focus the electrons onto the front face of the detector. An example run from a SIMION simulation is shown in Figure 3.15. The run consists of 10,000 electrons with a Gaussian distribution around a mean energy of 40 eV and a FWHM of 10 eV. The lens efficiency, defined as the total number of electrons hitting the detector divided by the amount of electrons leaving the catcher, was calculated from the simulation to be 14%.

Once the optimal lens voltages were determined, SIMION was run with a range of electron energies to determine the efficiency of detecting electrons from the catcher plate leaving with specific energies. Figure 3.16 shows the results of the simulation. Three cases were tested. The first case consisted of running the simulation with the lens system off to determine the efficiency of seeing electrons due to only solid angle. This is shown as the oranges dashed line. One can see the efficiency from solid angle alone is very low. This is due to the large distance between the catcher plate and the MCP detector. The second case consisted of having the ring system turned off while having the MCP detector on. The front face of the MCP detector was held at 1500 V. This case is shown as a blue, long dashed line. There is

clearly an increase in the efficiency due to the MCP detector attracting the electrons. The final case, shown as a solid black line, shows the efficiency of the lens system with all parts at their optimal voltage. Having the catcher plate at 4 V prevents low energy electrons from escaping, thus the efficiency drops for low energy electrons. The peak of the efficiency curve occurs between 10 eV and 40 eV. A significant portion of the internal conversion electrons from ^{235m}U decay will have energies in this range. Between 10 eV and 40 eV, the efficiency for having electrons hit the detector is between 14%–16%. It should be noted that these numbers do not take into account the efficiency of the MCP detector. The MCP detector efficiency is between 50%–70%. Using the simulation and taking into account the MCP detector efficiency, the expected detection efficiency for observing electrons from the decay of ^{235m}U leaving the catcher plate is between 7%–9%.

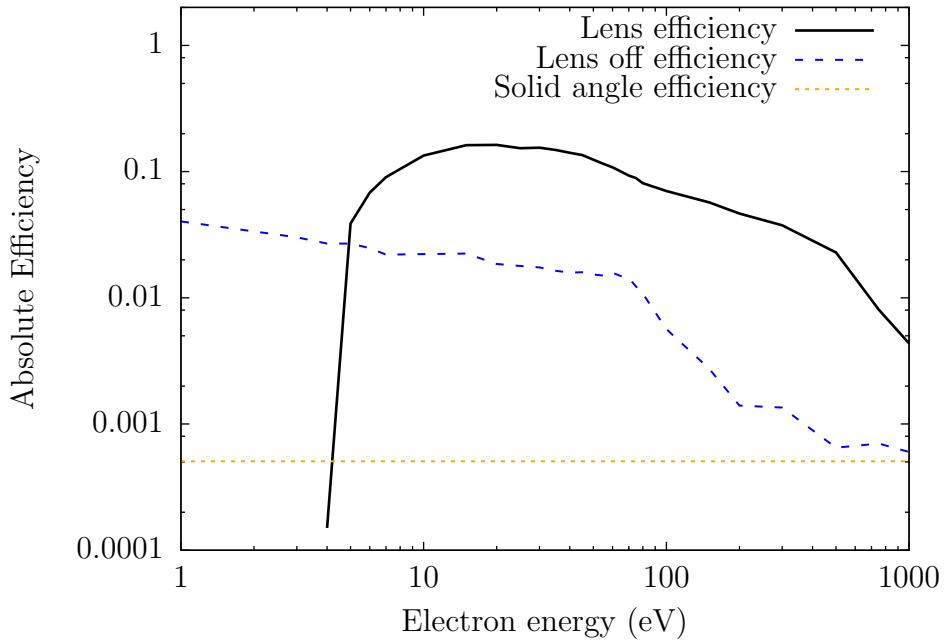

Figure 3.16: Efficiency of the electrostatic lens system from SIMION simulation.

3.4.2 Electron Detection Efficiency

To determine the efficiency for detecting internal conversion electrons coming from the catcher plate, a ^{239}Pu source was used. ^{239}Pu decays to ^{235}U by the emission of an alpha particle and has a half-life 24,110 years. Nearly 100% of ^{239}Pu decays proceed through the ^{235m}U state either by directly decaying to the state or arrive there via a gamma decay. Recoiling ^{235m}U nuclei from this decay have an energy of approximately 86 keV following the alpha decay. The ^{239}Pu was electroplated onto aluminum and had a source strength of 5.4

μCi. The source was placed 1.6 inches in front of the catcher plate in the chamber. ^{235m}U ions leaving the ^{239}Pu source were collected on the catcher plate. The same collection plate materials were used for both the uranium laser tests and the ^{239}Pu decay collections. The ^{235m}U was collected on a catcher plate that had a moderate negative potential of between -100 V to -240 V. Collection times varied, although most collection times were between thirty minutes and two hours. Collecting for thirty minutes produced 55% of the maximum signal, one hour produced 80% of the maximum signal and collecting for two hours produced 96% of the maximum signal. Following collection on the catcher plate, the plate was moved to the top of the chamber to the detection position. Internal conversion electrons from the ^{235m}U decay were accelerated and focused onto the microchannel plate detector.

Two methods of collection were done. The first method had the chamber at vacuum while the collection was occurring. The vacuum pressure was similar to the pressure used during the laser irradiation, P$< 10^{-6}$ Torr. Since the ^{235m}U leaves the source with over 80 keV of energy, many of the ^{235m}U nuclei will embed themselves into the catcher surface. Since the internal conversion electrons have energies less than 77 eV, many of the ^{235m}U nuclei were embedded too deeply for the low energy electrons to escape. The uranium ions produced in the laser plasma do not have energies as high as 80 keV. The typical energies of the uranium ions would be in the 10s of eV up to 100s of eV. In order to emulate these conditions using the ^{239}Pu source, a buffer gas was used. The purpose of the gas was to slow the ^{235m}U nuclei to the energies more representative of uranium from a laser plasma. This second method of collection used argon gas as the buffer. The argon gas slowed the ^{235m}U and allowed for improved collection. Various pressures were tested and the pressure used for the efficiency measurements was 2 Torr of argon gas. Collection times were similar to the times used during vacuum collection. A disadvantage of using argon as a buffer gas was that the MCP detector could not be on while collecting. During vacuum collection, no time was lost due to turning on the MCP detector since it could be on the entire time. Following collection in argon gas, the gas had to be pumped out. Once the pressure was less than 5×10^{-6} Torr, the MCP detector was turned on. It took approximately twenty minutes for the MCP to turn on following the start of pumping on the chamber. Using the argon collection method, one half-life would occur before the start of measurements. Although half the signal is lost due to the time delay, the initial count rate from argon collection compared to vacuum collection was approximately 10 times larger for the former. This can be attributed to the ^{235m}U being on the surface of the collection plate rather than being embedded too deeply for the internal conversion electrons to escape. The decay of ^{235m}U produced from ^{239}Pu decay can be seen in Figure 3.17.

The efficiency for the detection system was determined using the data found in Figure 3.17. The method for determining the efficiency is as follows. The ^{239}Pu source was placed 1.6" from the catcher plate. The catcher plate was held at -240 V. The solid angle between the Pu source and the catcher plate was determined to be 1.5 sr. This was calculated knowing the distance between the catcher plate and the ^{239}Pu source in addition to the surface area for both the catcher plate and the source. The ^{235m}U recoils were slowed in 2 Torr of argon gas for two hours. The range of uranium recoils in 2 Torr of argon is 0.9", thus stopping the

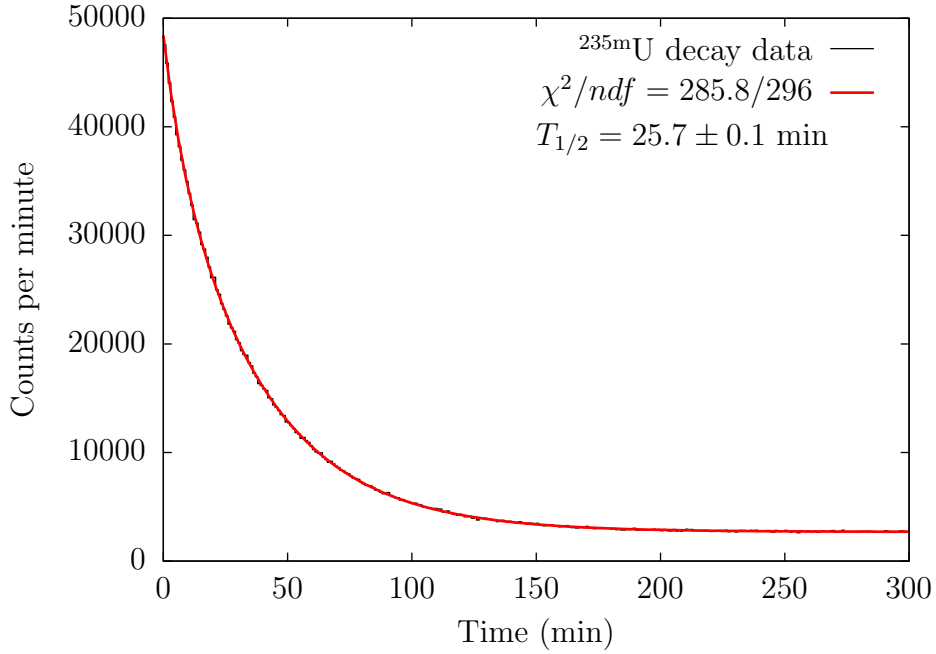

Figure 3.17: The decay of ^{235m}U produced by the decay of ^{239}Pu. The uranium recoils were slowed in argon gas and were collected for two hours.

recoils near the surface of the catcher plate. The ion range was calculated using SRIM [66]. After two hours, the catcher plate was raised to the top of the chamber and the internal conversion electrons from the decay of ^{235m}U were measured. The total efficiency for seeing the decay of ^{235m}U was determined to be 0.62%. In order to determine the efficiency of the detection system, the collection efficiency had to be taken into account. This was done by accounting for the solid angle losses. With a solid angle of 1.5 sr, only 12% of the uranium recoils from ^{239}Pu decay were collected on the catcher plate. Dividing the total efficiency of 0.62% by the collection efficiency of 12% yields the detection efficiency for seeing ^{235m}U decay on the catcher plate. The measured detection system efficiency for seeing ^{235m}U decay was determined to be 5.1%. This value can be compared to the value obtained using SIMION of between 7%–9%. The measured value is a little more than half of what the simulation predicted. The discrepancy is most likely due to an incorrect modeling of the lens geometry that was used in SIMION.

3.5 Microchannel Plate Detector

A microchannel plate (MCP) detector was used during the experiment to detect the electrons emitted from ^{235m}U decay. This detector was chosen due to its high efficiency of detecting electrons and its low dark count rate. An MCP is an electron multiplier. Charged

particles and photons with energies greater than 5 eV are able to start an electron cascade within the plate and the resulting signal is large enough to be measured. Depending on the detector design, the gain can be from 10^4 to 10^8. A MCP consists of a piece of glass with thousands of tiny channels with a slight pitch [62]. The diameter of these channels is typically around 10 μm. A high voltage is applied across the plate in order to create the large electron multiplication. When a charged particle or photon hits the wall of a channel, electrons are emitted. The high electric field causes a cascade of electron emissions. These electrons are then collected on an anode and the resulting signal is measured.

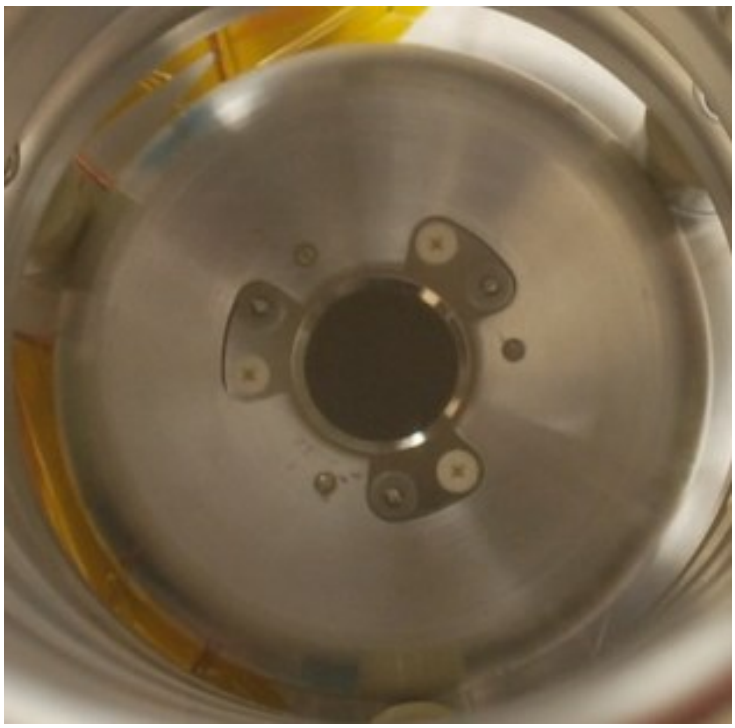

Figure 3.18: Picture of the front face of the MCP detector with the electron shield attached.

The MCP detector used for this experiment was a Photonis APD 2 MA 18/12/10/8 D 60:1 Grid. Figure 3.18 is a picture of the MCP detector. This detector had an active diameter of 18 mm and a grid in front of the MCP. In addition, this detector used a chevron design. A chevron design consists of two microchannel plates with their angled channels offset by 90°. There is a small separation between the plates. Electrons exiting the first MCP are able to enter multiple channels on the second. This causes multiple cascades to occur within the second plate. This arrangement greatly increases the gain for the detector. The detector used for the experiment had a gain that was larger than 10^7.

In order to properly bias the MCP detector, a resistor network was built. The resistor network applied the correct voltage to all parts of the MCP detector in addition to picking off the signal generated by the anode. Figure 3.19 shows the circuit diagram for the resistor box.

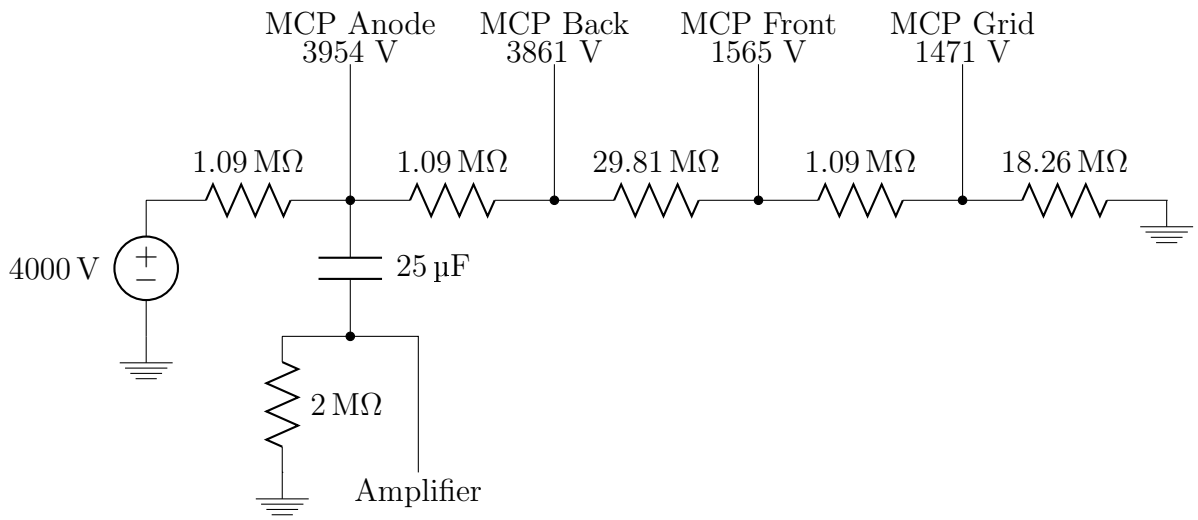

Figure 3.19: Resistor network circuit.

Only one high voltage supply was necessary to fully bias the MCP detector. The high voltage supplied to the resistor was 4000 V. Since the particles being detected were electrons, the front grid of the MCP detector was set to a high, positive voltage. The efficiency of the MCP detector is heavily dependent on incident electron energy. Therefore, high voltage helped to not only accelerate the electrons towards the detector, but it guaranteed the electrons striking the detector had an energy corresponding to a high efficiency. For this design, the grid voltage was measured to be 1471 V. Following the grid, the front face of the first MCP was set to 1565 V. By having the grid voltage be slightly less than the front face of the MCP, it forced any electrons generated on the surface of the MCP to be redirected back towards the detector. The voltage on the back face of the second MCP was measured to be 3861. This meant that the voltage across both microchannel plates was 2296 V. This was slightly under the limit set by the manufacturer of 2400 V. The anode of the detector was held at 3954 V. A steady resistor network current of 81 μA was measured during the experiment.

The signal generated by an electron striking the MCP detector was a short, negative pulse with a FWHM of 5 ns. Due to a mismatch between the MCP impedance (426 MΩ) and the impedance of the cables (50 Ω), pronounced ringing of the signal was observed. Instead of having a fast, large negative spike, there were numerous positive and negative spikes that decayed back to baseline after a couple of hundred nanoseconds. In addition to the signal pulses, there were large pulses coming out of the MCP detector that had a unique, long shape. Unlike the fast pulses seen when electrons hit the MCP, these pulses had a width on the order of 100 ns. These pulses would occur sporadically and had the exact same energy every time. A large proportion of these longer pulses were positive. This suggests that they were produced directly by the anode and were not from electron cascades occurring in the channels. Due to the complexity of the signals coming out of the MCP detector, numerous iterations of electronics configurations were tested.

3.6 Electronics

Multiple electronic configurations were used throughout the experiment. The goal was to be able to readout the MCP signals and obtain an energy spectrum. An energy spectrum was desired over just using a scaler because it was important to be able to cut out the low energy noise and the high energy background events. There were numerous difficulties for the electronics setup. First, the signal out of the MCP detector was very fast. An amplifier able to quickly shape the signal was necessary. In addition, the MCP signal had significant ringing. Since the signal was being sent to a discriminator, false counts could be registered if the discriminator fired due to one of the smaller peaks. The large positive signals generated by the MCP detector also caused problems. The setup had to prevent these signals from triggering the discriminator. For these reasons, creating an electronics setup that can overcome these signal features was difficult.

Initially, a preamp was used following the MCP resistor network. The first preamplifiers tested with the system were fast preamplifiers. The first one tested was the Ortec VT-120A. This preamp amplified the signal 200 times and was non-inverting. The problem with this preamp was the amplification was too large. The pulses coming out of the voltage box were approximately -30 mV. The output for this preamp was limited to -5 V. Therefore, the output was saturated a significant amount of time. This was eventually corrected by using the Ortec VT-120C that only had 20 times amplification. However, with a goal of getting the energy spectra for the MCP, it was thought that a charge sensitive preamp may perform better. The A1424 scintillation preamp from CAEN seemed to fit. Initial testing produced mediocre results. The output from the preamplifier was a fast rise time signal with a slow decay. However, that signal was riding on a wildly varying baseline. This caused some issues with setting an appropriate threshold. This preamp was used for a couple of weeks until it unexpectedly failed. What caused the failure is not known. Following the failure and numerous unexplained shut offs of the high voltage supply, no other preamplifiers were used. It was determined that preamplifiers were not needed. The signal directly out of the resistor box was large enough to use in a timing filter amplifier.

For the next electronics setup, the signal out of the resistor box went directly to a timing filter amplifier (Ortec 474). The timing filter amplifier shaped and amplified the MCP signal. The output of the timing filter amplifier was a short, negative pulse. This pulse was then sent to a passive splitter box. The box split the signal with one part going to a shaper and the other going to a discriminator. The discriminator used was a Phillips Scientific Model 710. The threshold was set to -22.1 mV. The purpose of the discriminator was to set a gate for the analog to digital convertor (ADC). Due to the issue of ringing of the MCP signal occurring, an artificial dead time was introduced in the system. This was done to prevent multiple signals from the same electron cascade being digitized by the ADC. The dead time was set to 15 μs. A gate would be generated if the signal was above the threshold value in the discriminator and the gate could not be re-triggered for 15 μs. The second signal from the passive splitter was sent to a Mesytec MSCF-16 shaper. The shaper had a shaping time of 250 ns and produced a positive Gaussian shaped signal which was then sent to an ADC.

The final electronics setup had the MCP signal going directly to the passive splitter. One output of the splitter went to an Ortec FTA 820 fast amplifier. This signal was then sent to the discriminator and then a gate and delay generator in order to generate a gate. Similar to the previous setup, a 15 μs dead time was used. The second output of the passive splitter was sent to an Ortec 450 research amplifier. The signal was shaped into a positive Gaussian and was sent to the ADC. A diagram of the final electronics setup is shown in Figure 3.20.

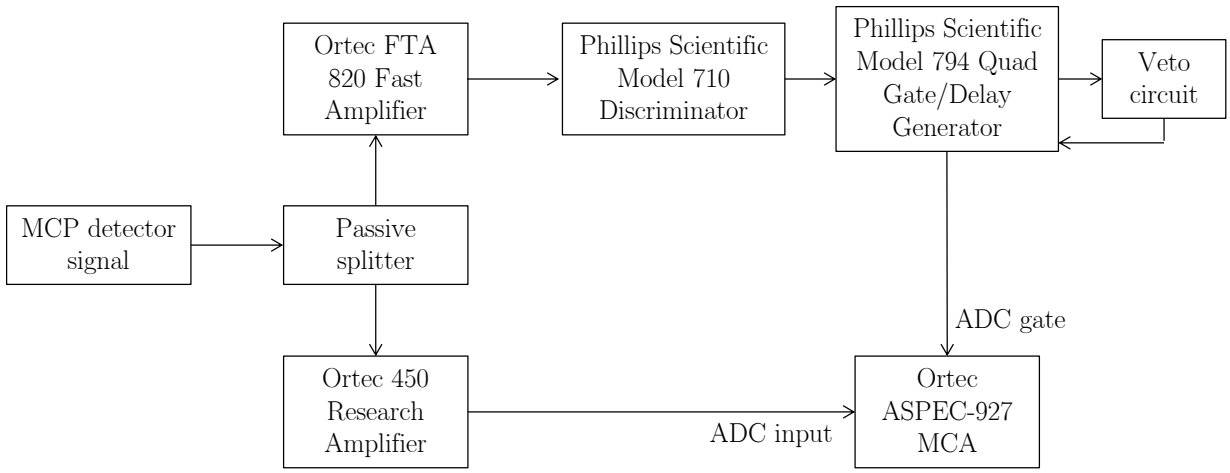

Figure 3.20: Diagram of the final electronics setup.

The ADC used in this experiment was an Ortec ASPEC-927 MCA. The signal entering the ADC was gated in coincidence with the gate generated by the discriminated signal. The MAESTRO-32 program was used to take the data. The ADC was set to 4,096 channels (12 bit resolution). The ADC's lower threshold was set to be slightly higher than the discriminator threshold. An example energy spectrum obtained during the experiment is seen in Figure 3.21. The data was collected using an automated job file. The job file set the ADC to record individual spectra for one minute and save each spectrum to a specific file. The total number of spectra created by the job file varied, but the majority of runs saved 950 individual spectra. This equates to a total of approximately 16 hours of data per run. The total number of counts in each spectrum used during the data analysis was determined by integrating the counts from channel 40 through channel 200.

This final electronics setup was able to solve the numerous issues initially plaguing the experiment. First, the discriminator was able to cut out the electronic noise by preventing the system from triggering. Second, the 15 μs dead time prevented two known issues. It prevented any additional triggers due to the ringing. It also prevented correlated electrons from a single event from triggering the system. Additionally, the discriminator would not fire due to positive signals. This meant that the large, positive signals coming out of the MCP

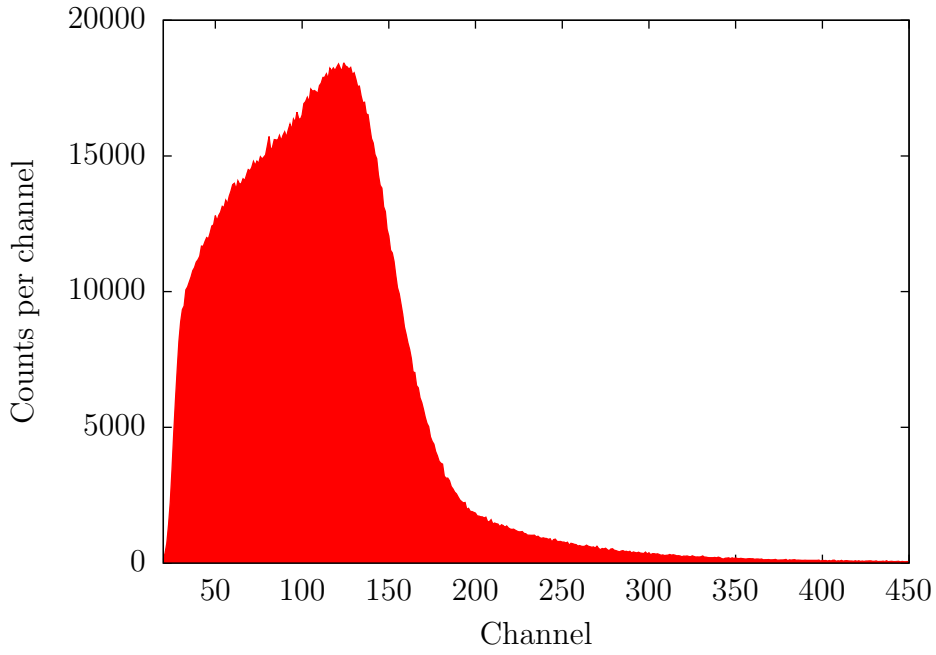

Figure 3.21: An example energy spectra from the MCP detector. Each electron event saturates multiple electron channels in the MCP detector due to the large gain in each channel. This produces the spectrum shape visible in this figure. Channels 40 through 200 were used for the data analysis.

detector were prevented from triggering the system. Once a stable setup was assembled, no changes to the electronics were made.

Chapter 4

Metal Ablation Experiments

This chapter discusses the laser ablation experiments conducted to determine the properties of materials undergoing laser ablation. The initial ablation tests were performed on nonradioactive materials. The goal was to understand the amount of material ablated from the target in addition to determining the spot size of the laser on the metal targets. The chapter also includes the results of laser plasma simulations that were run in order to predict the amount of NEET occurring in the uranium plasma. These simulations were performed using both ytterbium and uranium targets.

4.1 Laser Plasma Simulations

In order to better understand the plasma generated from the laser, plasma simulations were performed. The simulations were run by Scott Wilks in the Theory and Modeling Group at Lawrence Livermore National Laboratory. The laser plasma was modeled using HYDRA. HYDRA is a multidimensional hydrodynamic plasma simulation code. Visualization of the simulation along with analysis were done using VisIt [67]. Simulations were performed using a variety of laser conditions and spot sizes. Due to classification issues, most of the simulations were done using ytterbium (Z=70) as the target. Ytterbium was chosen due to its high Z. Once the laser conditions were finalized, simulations were run using a uranium (Z=92) target in addition to a ytterbium target. The uranium simulations were run using a similar code to HYDRA. The simulations showed the plasma generation and evolution over 40 ns. Both simulations were run in three dimensions with cylindrical symmetry.

The main goal for the plasma simulations was to predict the number of uranium isomers produced within the plasma. Due to my inability to analyze the uranium simulation, the initial analysis was done using the ytterbium simulation. The procedure to calculate the number of isomers generated was developed by treating ytterbium as if it was uranium. Once the procedure was developed, it was applied to the uranium simulation to obtain the predicted number of isomers generated. Both simulations had the exact same laser conditions, the only difference between the two simulations was the target material. The

laser properties used during the simulations can be seen in Table 4.1. The laser intensity 10 nanoseconds after the start of the laser pulse is shown in Figure 4.1. One can see the max intensity of the simulated laser was $7.4 \times 10^{11}\, W/cm^2$.

Parameter	Value
Wavelength	1064 nm
Pulse energy	780 mJ
Spot size	50 μm $\times$ 100 μm
Pulse shape	Trapezoidal
Pulse rise time	10 ns
Pulse flattop time	1 ns
Pulse fall time	10 ns
Lens focal length	350 mm

Table 4.1: Laser properties used during both the ytterbium and the uranium simulations.

The number of uranium isomers produced was calculated using the simulation data. The number of isomers produced, N_I, can be calculated using the equation

$$N_I = \frac{\rho N_A \lambda_{NEET} V \Delta t}{A}, \tag{4.1}$$

where ρ is the density of the plasma, N_A is the Avogadro constant, λ_{NEET} is the NEET excitation rate, V is the volume of the plasma, Δt is the length of time the plasma is in the correct ionization state, and A is the atomic mass. All parameters in the equation except for λ_{NEET} were obtained from the simulation. The simulation data was divided into three dimensional cells. The number of isomers produced was calculated within each cell and the cells were added together to obtain the total number of isomers produced. A cut in the simulation data was made to only accept cells that had the correct ionization. In the case of uranium, only cells with an ionization of 10^+ or 23^+ were accepted. The ion density and volume for the cells were calculated within the simulation. Δt was determined by the time step for the simulation data. The two plasma properties that greatly affect the number of isomers generated are the ionization of the plasma and the density of the plasma. Figure 4.2 shows the ionization of the ytterbium plasma 10 nanoseconds after the start of the laser pulse. One can see the red region consists of ytterbium ionized to between 20^+ and 23^+. The green region consists of ytterbium ionized to between 8^+ and 15^+ charge states. It takes a similar amount of energy to ionize ytterbium to a 22^+ charge as it takes to create 23^+ uranium. Additionally, it takes a similar amount of energy to ionize ytterbium to a 10^+ charge state as it does to create a 10^+ uranium ion. The figure shows a large region where the correct ionization states exist for NEET to occur. The density of the plasma 10 nanoseconds after the start of the laser pulse can be seen in Figure 4.3. The regions that

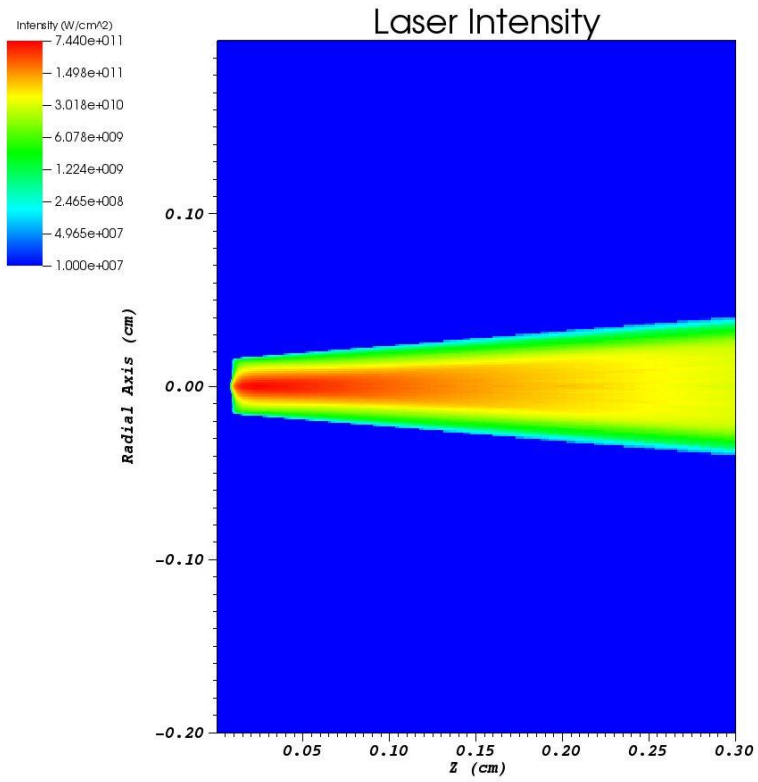

Figure 4.1: Power density of the laser 10 ns after the start of the laser pulse.

have ionization of around 23^+ and have a high density contribute the most to the production of the isomer.

To estimate the number of isomers produced using the uranium simulation, the NEET excitation rate had to be set. The NEET excitation rate was set to different values to generate 3 cases. The rates used were the rates found in [25]. The first case used a conservative estimate for the NEET excitation rate. The second case used excitation rates that would produce the most isomers. The third case used excitation rates that are near the limit set by [37]. The excitation rates used for each case can be seen in Table 4.2. For the most conservative case, Case 1, the predicted number of isomers produced was 0.139 per laser shot. This is a very small number of isomers generated. Using typical experimental run conditions of 30 laser shots per collection period, the simulation predicts only 4 isomers would be produced. The decay of 4 isomers would not be visible above the background. Case 2 shows the opposite case due to the high excitation rates. The simulation predicted 67,100 isomers produced per laser shot. A run of 30 laser shots would produce 2,013,000 isomers. The activity for that many isomers would be 900 Hz. That signal would be easy to see over a background of a few Hz. It should be noted that Case 2 has the 23^+ NEET excitation rate set to 1 isomer per second. That is the rate claimed to be measured by the

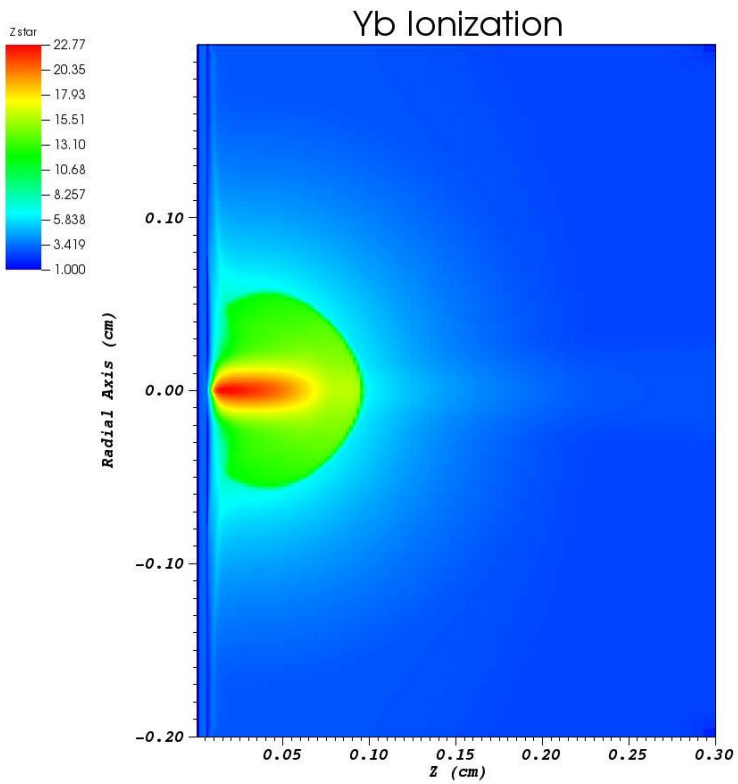

Figure 4.2: The ionization of the Yb plasma 10 ns after the start of the laser pulse. The maximum ionization was approximately 23^+ and occurs near the surface at the point of maximum power density.

first experiment in 1979 [33]. The last case has the NEET excitation rate similar to the limit set in [37] and the simulation predicted 2.58 isomers produced per laser shot. A run of 30 shots would produce 77 isomers. The activity for that sample would be only 0.03 Hz. That would be difficult to see above a background of a few Hz. It may be possible to see that signal if multiple independent measurements were performed and the background was well known. The limit set in [37] was done using the data from 10 independent measurements.

4.2 Metal Ablation Experiments

As described in section 3.2.2, a test chamber was used to perform a variety of experiments. The metal ablation experiments were done in the test chamber with the optical setup shown in Figure 3.6. There were multiple goals for these ablation experiments. First, to determine the spot size of the laser on the target. The spot size is defined as the diameter of the laser spot. The spot size determines the power density and would influence the charge states

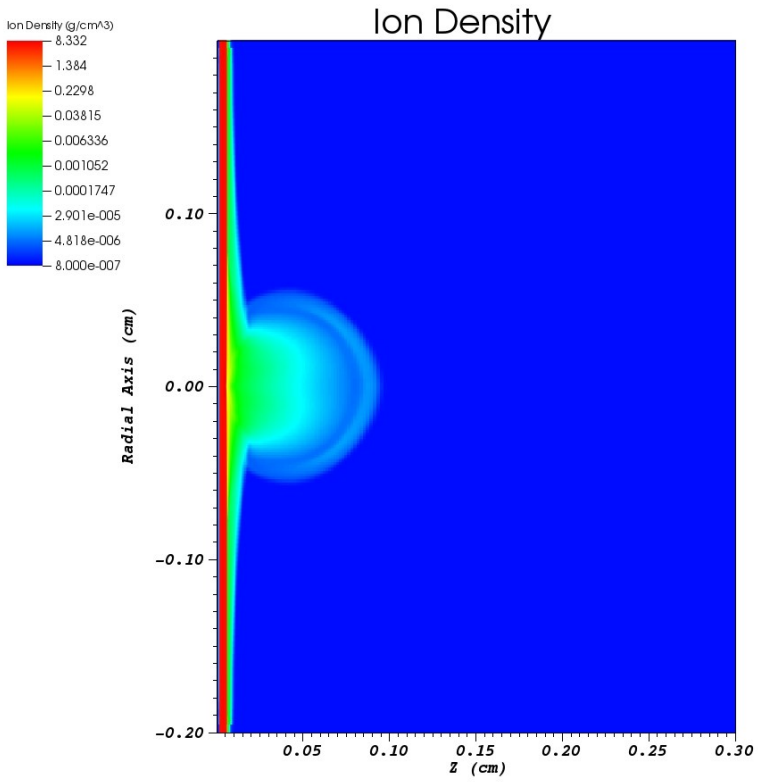

Figure 4.3: The ion density of the Yb plasma 10 ns after the start of the laser pulse.

produced in the plasma. Second, the ablation tests helped determine the spread of the ablated material over the catcher plate. The plasma plume created by a laser is forward peaked with a significant amount of ablated material ejected normal to the surface [68]. It was important to know the amount of material that came off normal to the surface versus the other directions. Since the experiment was limited by the ability of low energy electrons

Case number	U^{10+} λ_{NEET} (s^{-1})	U^{23+} λ_{NEET} (s^{-1})	^{235m}U produced per laser shot
Case 1	10^{-9}	10^{-6}	0.139
Case 2	10^{-4}	1	67,100
Case 3	10^{-6}	10^{-6}	2.58

Table 4.2: The three cases used during the uranium simulation in order to predict the number of isomers produced per laser shot. These cases span the predicted NEET excitation rate found in [25].

to escape a thin layer of uranium, knowing how much material covered the catcher plate was crucial. In addition, the material that was not ejected towards the catcher plate would contaminate the surrounding components. The amount of material lost due to contamination of the surrounding components was also important to know. The third goal was to determine the differences in ablation due to different materials. The initial tests were done on materials that were easy to obtain quickly in the lab. These were materials like aluminum, copper and steel. Following those tests, materials were chosen due to similar physical properties to uranium. Ytterbium was chosen since the simulations used ytterbium. Tungsten and tantalum were chosen due to their high densities and high melting points. Carbon steel was chosen due to its high melting point. A full list of the materials chosen and their basic chemical properties can be found in Table 4.3. The final goal for these tests was to determine how quickly the laser went through the material. This was needed to determine the size and thickness necessary for a uranium target.

Metal	Atomic Number	ρ (g/cm^3)	T_{melt} (°C)	T_{boil} (°C)	c_p ($J/(g \cdot K)$)	λ ($W/(m \cdot K)$)
Al	13	2.70	660	2519	0.12	237
Cu	29	8.96	1085	2560	0.385	401
Yb	70	6.90	824	1196	0.155	38.5
Ta	73	16.4	3017	5455	0.140	57.5
W	74	19.3	3414	5555	0.132	174
U	92	19.1	1135	4131	0.116	27.6
Stainless steel	–	7.9	1425	–	0.483	15
Carbon steel	–	7.86	1515	–	–	52

Table 4.3: Metal targets used for the ablation tests along with basic physical properties [69]. The properties listed in the table have the following meanings: ρ is the density of the metal, T_{melt} is the melting point, T_{boil} is the boiling point, c_p is the heat capacity, and λ is the thermal conductivity.

The initial tests involved placing the various metals into the test chamber in order to determine the spot size of the laser after it went through a plano-convex focusing lens. For these measurements, no catcher plate was used. The initial measurements had the metal targets perpendicular to the laser beam. This initial design was found to be problematic. The ablated material would leave normal to the surface and embed into the laser window attached to the test chamber. This left metal spots on the laser window that would reflect incoming laser light, thus reducing the laser intensity entering the chamber. Additionally, the metal spots on the laser window caused back reflections of the laser light. To reduce the possibility of the ablated material contaminating the laser window, the target holder was placed at a 45° angle to the beam path. A picture of the initial setup with the target

holder at a 45° angle is seen in Figure 4.4. It was determined that this position still allowed for ablated material to hit the laser window. To further reduce the possibility of material embedding into the laser window, an additional, easily replaceable laser window was placed inside the chamber. A picture of this setup is shown in Figure 4.4. The metal block in the back of the chamber was added to prevent the laser from hitting the chamber and ablating the chamber wall. The right picture in Figure 4.4 shows an anodized piece of aluminum placed on the chamber wall. This was the first test involving a catcher plate to determine the directionality of the plasma plume.

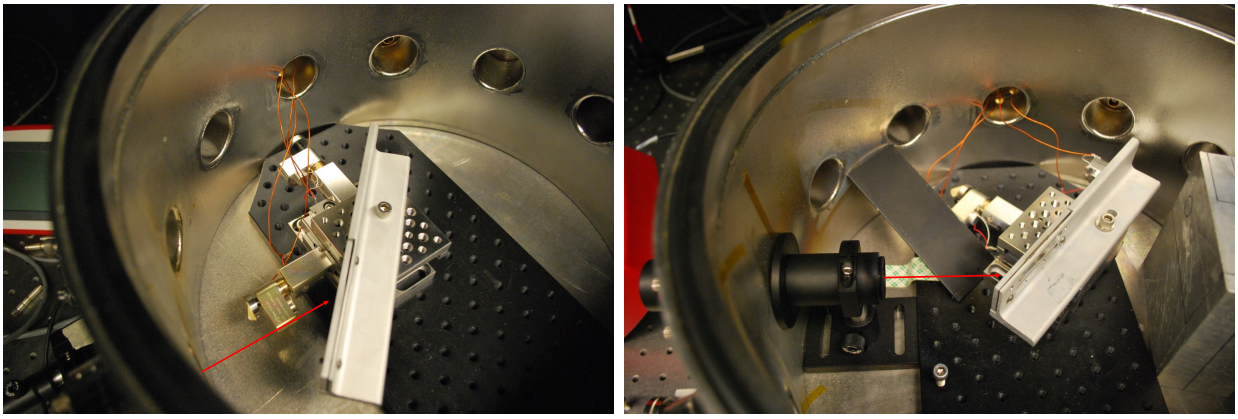

(a) Initial test chamber setup (b) Improved test chamber setup

Figure 4.4: Picture (a) shows the test chamber setup with the target holder at 45° to the beam path. The beam path is shown by the red arrow. Picture (b) shows the test chamber setup with a laser window within the chamber to prevent ablated material from embedding into the vacuum laser window. An anodized aluminum catcher plate is leaning against the chamber wall. The beam path is shown by the red arrow.

Most of the initial tests were to determine the spot size of the laser on the target following the focusing lens. In order to obtain the highest power density possible for the laser, the metal target had to be located at the beam waist of the laser. The beam waist would generate the smallest spot size. The following calculations assume a Gaussian beam. Although the laser beam used during this experiment was not Gaussian, the calculations demonstrate the importance of accurately knowing the distance between the focusing lens and the target. For a Gaussian beam, the effective diameter for a focused beam can be approximated as

$$d_0 \approx \frac{2f\lambda}{D}, \tag{4.2}$$

where f is the focal length of the lens, λ is the wavelength of the laser, and D is the diameter of the laser entering the focusing lens [60]. The effective diameter is the $1/e^2$ width of the

laser. It contains 86% of the laser power. For this test experiment, the focal length of the plano-convex lens was 150 mm, the wavelength was 1064 nm, and the diameter of the laser exiting the beam expander was 22 mm. This would give an effective spot size of 15 μm. One can see the importance of knowing the distance between the focusing lens and the target when calculating the Rayleigh range. The Rayleigh range is defined as

$$z_R = \frac{\pi\omega_0^2}{\lambda}, \tag{4.3}$$

where ω_0 is the radius at the beam waist ($d_0 = 2\omega_0$) [60]. At a distance of z_R, the spot size of the laser spot is equal to $\sqrt{2}d_0$. For the values given above, the Rayleigh range is 150 μm. If the target is 150 μm away from the waist, the spot size would be 20 μm. The power density when the target is at the beam waist is nearly 1.7 times larger than when it is at the Raleigh range. That difference in power density would greatly affect the plasma generated. In order to determine the smallest spot size, a modified setup was used. The modified setup placed the focusing lens on a manually controlled translation stage. This allowed the distance between the focusing lens and the target to be varied. To know how much distance the lens traveled, a gauge was attached to the stage with a resolution of 0.001".

The spot size for the laser was determined by irradiating the metal targets with the focusing lens located at different distances from the target. The lens was moved in increments of 0.01" (254 μm). The target was translated after each laser shot in order to have a clean surface and to measure the spot size for a single laser shot. Once it was determined which spot had the smallest spot size, the test was run again using 0.005" (127 μm) increments. The tests used to determine the smallest spot size were performed on numerous metal samples. How the smallest spot size was determined along with how much material was ablated is described in the following section.

4.3 Sample Diagnostics

Numerous methods were used to determine the spot size of the laser on the metal targets in addition to measuring the ablation properties. The quickest method was a visual inspection of the target. If the target was far from the beam waste of the light exiting the focusing lens, the spot size would be large and shallow. Additionally, one can see the directionality of the plume by the presence of iridescence on the catcher plate due thin-film interference caused by the ablated material. More thorough investigations of the spot size and ablation rate were done using a variety of scientific instruments. The instruments used and their results are described below.

4.3.1 Microscope Analysis

The most straightforward method used to determine the spot size was using an optical microscope to measure the crater sizes. A stage micrometer with 10 μm divisions was used

Figure 4.5: This picture shows the craters created on a copper target by the laser. The smallest spot size occurs in the middle of the image.

to calibrate the viewing lens for the microscope. The materials that were shot with the laser were observed using a variety of magnifications to determine the size of the crater. The craters were composed of three regions. The central region was a deep, circular pit in the material. The second region consisted of an annulus of raised material that surrounded the central pit. The third region was the area outside of the annulus that consisted of melted material. The central region that consists of the deep pit was defined as the spot size for this experiment. An image of multiple craters caused by the laser irradiating copper can be seen in Figure 4.5. One can see that the middle craters are smaller suggesting they were produced when the target was close to the beam waist. All three regions are visible in the picture. The central pit is surrounded by an annulus. There is a large, circular region surrounding each hole that consists of melted material. This region is clearly different than the material not affected by the laser seen at the top and bottom of the image. This method of determining the spot size suffered from the inability to focus the lens to a level adequate enough to truly determine the size of the pit. The pits measured using this method ranged in diameter from 60 μm up to 250 μm. No pits were measured with a diameter near the value of 15 μm calculated above. This is most likely due to the fact that the beam was not a Gaussian beam and did not focus as well as a Gaussian beam. It was discovered that the ability to observe the marks left by the laser was dependent on the material that was shot. Materials with low melting temperatures and low densities like copper and aluminum generated more visible marks than materials with high melting temperatures and high densities like tantalum and tungsten. For this reason, it was not possible to determine the spot size for the materials

with high density and high melting points using a standard optical microscope.

In order to determine the spot size for the shots on tantalum, a scanning electron microscope (SEM) was used. Multiple images with varying magnifications were produced. Figure 4.6 shows an image of one of the spots along with measurements for the spot size. The shortest length is for the diameter of the pit produced (region 1). The middle length is the diameter of the annulus surrounding the pit (region 2). The largest length is for the area of melted material surrounding the annulus (region 3). The spot size for this pit matched the smallest spot size found using the optical microscope. Figure 4.7 shows two regions of the tantalum surface. The left image is an area on the surface of the tantalum that was not affected by the laser. The entire surface of the tantalum before the laser irradiation looked like left image. The right image shows the surface at the center of a pit generated by the laser pulse. There is clear evidence of melting seen in the right image that was caused by the high power density of the laser. The microscopes were able to determine the spot size which was needed to understand the power density of the laser. A drawback of using both the scanning electron microscope and the optical microscope was the inability to measure how deep the pits were. The depth was needed in order to determine how much mass was ablated with each laser shot. The depth was determined using a profilometer.

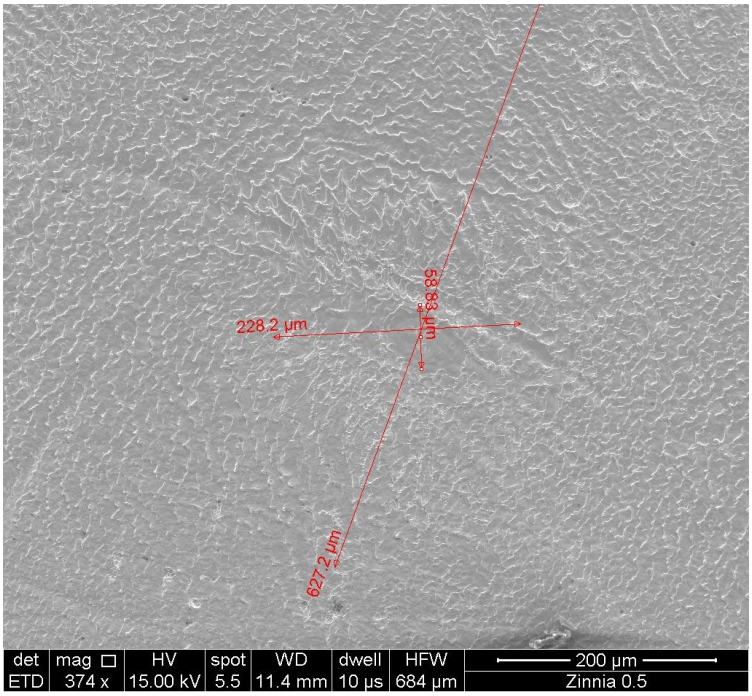

Figure 4.6: A SEM image of a laser spot on tantalum. Region 1 has a diameter of 59 μm. Region 2 has a diameter of 228 μm. Region 3 has a diameter of 627 μm.

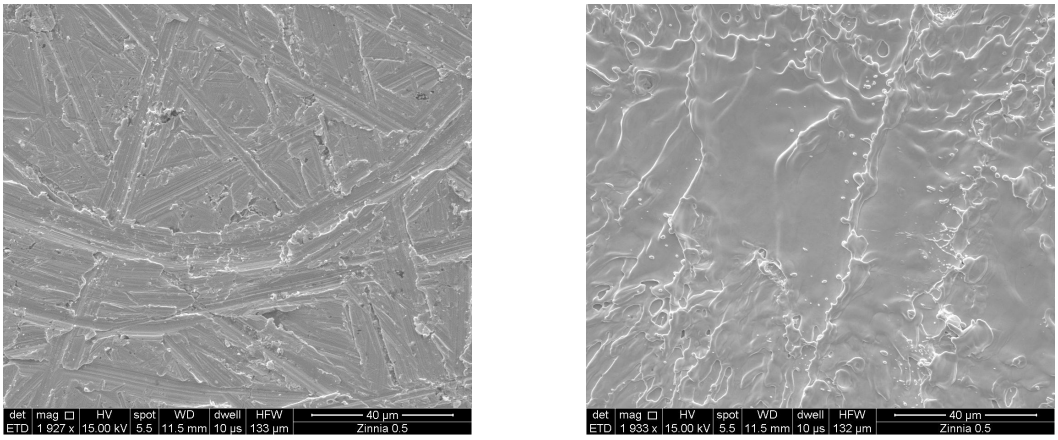

(a) Unirradiated surface (b) Irradiated surface

Figure 4.7: Picture (a) shows the surface of tantalum before laser irradiation. Picture (b) is a highly magnified image of the center of a pit created by the laser pulse. The scratches are no longer visible and there are clear signs of melting due to the intensity of the laser.

4.3.2 Profilometer Analysis

The main use of the profilometer was to more accurately determine the spot size. The profilometer was also able to measure the depth of the pits. The ability to calculate the depth allowed for a measurement of the ablation rate. The profilometer was a Nanovea PS50. It was able to scan the entire surface of the target and generate both two and three dimensional images of the craters. In addition, the program used with the profilometer was able to calculate the volume of the pits. Coarse measurements were initially performed to ascertain general sizes for each of the craters. The smaller craters were measured with a higher resolution in order to determine both the spot size and depth. A depth profile for a crater created on a carbon steel target is seen in Figure 4.8. The pit region has a diameter of 30 μm. This was the smallest spot measured. It was only twice as wide as the Gaussian beam waist calculated in Section 4.2. The annulus region surrounding the pit is also clearly visible in the figure. The depth profile shows that the annular region is raised compared to the background region. Using the depth profile, the volume of material ablated could be calculated. Assuming a 30 μm diameter spot with a depth of 15 μm gives a volume of 10,600 μm^3. For carbon steel, that equates to a mass of 83 ng. A more accurate calculation was done using the program provided with the profilometer. The pit region was defined and the volume for that region was calculated. Figure 4.9 shows the region used to calculate the volume of the pit formed in carbon steel by the laser. The volume was found to be around 15,000 μm, which equates to a loss of 120 ng of material for the one laser spot. This was the first measurement of the ablation rate performed. It was only done for the carbon steel targets. The profilometer was not able to accurately measure the tungsten or tantalum targets due to their shallow depth.

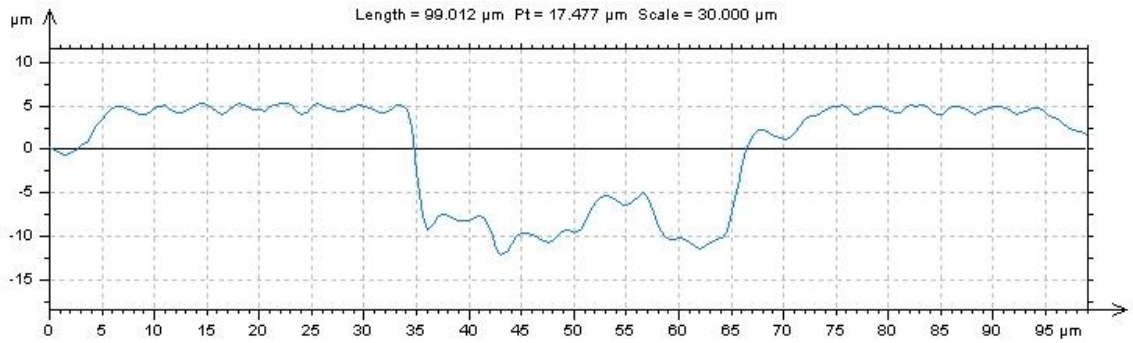

Figure 4.8: The depth profile created using the profilometer. This spot corresponds to a single shot on carbon steel. The pit region and the raised annulus region are visible in the figure.

Using the profilometer to measure the ablation rate had a couple of issues. First, very high resolution measurements of the entire pit region were not able to be performed due to time constraints. That limited how accurate the volume calculation was. Second, each laser shot was not exactly the same. There were differences in the temporal profile and slight differences in the energy. Using one single shot to determine the ablation rate may not be representative of all the laser shots. Regardless of the issues for calculating the mass ablated, the profilometer was able to accurately measure the spot size. In order to measure the mass ablation rate, a new method was devised that used a scale to measure the mass loss of the target after numerous laser shots.

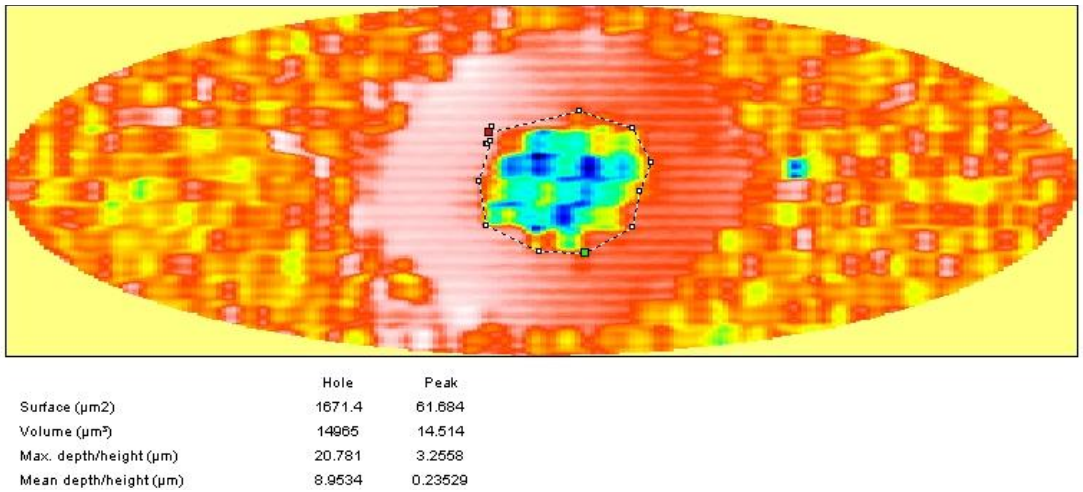

Figure 4.9: Profilometer calculation for the volume of a spot on carbon steel. The colors correspond to the depth of the region. The blue-green colors indicate deeper regions. The raised annulus surrounding the pit is visible in the image.

4.3.3 Mass Loss Analysis

A method was devised to directly measure the mass loss of targets due to metal ablation. All targets were measured using a scale to determine their mass to a tenth of a milligram. Since the amount of ablated material per shot was thought to be in the nanograms or micrograms regime, numerous shots were required to be able to measure any mass differences. The first direct measurement of the mass loss due to laser ablation was done using ytterbium. This initial measurement encountered many difficulties. It was the first measurement involving ytterbium and it was not known how it would behave under laser irradiation. In order to be able to measure a mass change, the laser was set to output a pulse 10 times a second. The target was translated during the laser shots in order to prevent the laser from going through the target. The target was irradiated for 150 seconds. There was no method to directly measure the number of laser shots. It was assumed the laser output a steady 10 Hz and the shutter was closed at the 150 second mark. The result of the two sets of irradiation can be seen in Figure 4.10. The mass difference measured was 0.0105 g. This equates to a mass loss of 7 μg per shot. This value was significantly higher than what was obtained using the profilometer. This may be due to ytterbium's low melting and boiling point. Tests were then performed using aluminum targets. These tests were performed using the manual control of the laser for a more accurate determination for the number of shots hitting the target. The measured ablation rate for aluminum was between 2.2 μg per shot and 2.6 μg per shot. These numbers were needed in order to determine the mass of uranium needed for the experiment. The mass loss measurements performed were also used as test runs before ablation measurements were done using radioactive elements.

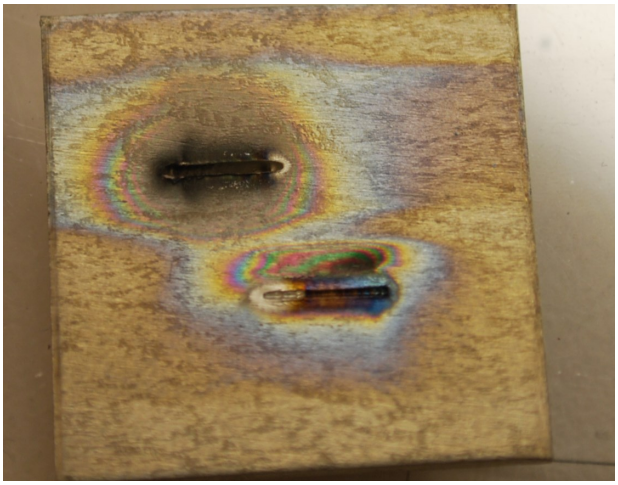

Figure 4.10: Picture of the ytterbium sample after two runs of laser irradiation.

Chapter 5

Initial Depleted and Natural Uranium Experiments

This chapter discusses the laser ablation experiments done on depleted and natural uranium samples. In order to characterize and understand the uranium ablation plasma, tests were performed on depleted and natural uranium targets. Both depleted and natural uranium were chosen as test targets due to their low specific activity and ease in obtaining metallic and ceramic samples. Two types of experiments are discussed in this chapter. First, ablation rate experiments using metallic uranium samples are discussed. These experiments were necessary in order to determine both the amount of ablated material created per laser shot in addition to the direction of the ablated material. The second part of this chapter focuses on the initial null test experiments done using depleted uranium metal, samples produced using additive manufacturing, and ceramic natural uranium.

5.1 Depleted and Natural Uranium Samples

Four types of targets were used during the null test experiments. The characteristics for each of the samples are given in Table 5.1. The sample labeled DU metal was the first sample of uranium obtained for the experiment. It was a small sample of depleted uranium metal with a thin oxide layer on the surface. It had an uneven shape with approximate dimensions of 5 mm by 4 mm by 2 mm. The sample had a metal purity of 99.977% and consisted of 99.8% ^{238}U and 0.02% ^{235}U. The initial uranium tests used this sample of uranium. This included the tests to determine the uranium ablation rate and the plume direction. In addition, the initial null test experiment using uranium within the large chamber utilized this sample. Due to its small size, subsequent tests in the large chamber used the samples created using additive manufacturing. Those samples were larger and easier to align with the laser focal spot.

In order to have a null target for the enriched uranium ceramic puck, two natural uranium ceramic pucks were made. The ceramic pucks had a mass of 507 mg and 297 mg and were 1

cm diameter pucks with a thickness of 1 mm. Due to the pucks being ceramic, the material characteristics were significantly different than the metal samples. These were mixed oxide pucks and contained more than one oxidation state of uranium. The pucks had a density of 6.5 g/cm^3 and 3.8 g/cm^3. This density is lower than uranium's metal density of 19 g/cm^3. In addition, the heat conductivity for the uranium ceramic sample was lower than that of metal. Localized heating due to the laser did not dissipate as quickly. More importantly, the ceramic samples were very brittle and chalky. Although both the enriched ceramic and the natural ceramic were pressed and sintered under the same conditions, the integrity of the samples were not similar. This is being attributed to the difference in grain size for the enriched uranium powder and the natural uranium powder. Due to the structural integrity of the ceramic samples being very poor, only a few tests were performed using them.

The third type of uranium used during the null test experiments was produced using additive manufacturing (AM). The samples were not pure uranium metal. They were a uranium binary consisting of 94% uranium and 6% niobium. Unlike the ceramics, these samples had a density close to the metal density of uranium. The benefit of additive manufacturing was that the targets were created to the exact specifications for my target holder and were metallic. Five samples were produced. All of the samples were pucks with a diameter of 1 cm. Two samples had a thickness of 1 mm, one sample had a thickness of 2 mm, and the final two samples had a thickness of 3 mm.

The fourth and final uranium sample used for the null tests was depleted uranium carbide. Uranium carbide was chosen due to its good heat conductivity, high density, and the ability to turn highly enriched uranium dioxide powder into uranium carbide. Uranium carbide (UC) has a theoretical density of 13.6 g/cm^3, which is closer to the metal density of uranium than the mixed oxide ceramic pucks. The target mostly consisted of UC, but also contained UC_2 and U_2C_3. The sample was a hemisphere with a mass of 410 mg. In order to fit within the sample holder, the sample was broken apart into 5 irregularly shaped pieces. The piece with the largest size was used for the null tests.

Sample Name	Form	Shape	Mass (g)	^{235}U	^{238}U
DU metal	Metal	Cuboid	0.7	0.2	99.8
NU ceramic 1	Ceramic	Puck	0.507	0.7	99.3
NU ceramic 2	Ceramic	Puck	0.297	0.7	99.3
AM metal	Metal	Puck	1.3	0.2	99.8
DU carbide	Ceramic	Hemisphere	0.410	0.2	99.8

Table 5.1: The natural and depleted uranium samples used during the null test experiments. The general characteristics for each sample are given along with the nominal mass fraction isotopics for the two main isotopes within the sample.

5.2 Ablation Rate Experiments

In addition to the metal ablation experiments using nonradioactive metals explained in Section 4.2, uranium ablation experiments were needed to determine how uranium behaves under laser irradiation. Due to the sensitivity of the detector and the small theoretical estimate for the signal, low background was essential for the experiment. A well characterized ablation rate and collection efficiency were needed in order to determine the background caused by the alpha decay of uranium on the catcher plate. These experiments were performed in two parts. The first experiments were done using the small test chamber. These initial experiments determined not only the amount of material being ablated from each laser shot, but also the direction of the ablated material. In addition, the plume spread was measured on the catcher plate. This determined the degree at which the plume was forward peaked. The information learned during these initial ablation experiments guided the design of the large chamber experiment. The second set of ablation experiments were performed on uranium targets within the larger experimental chamber. These experiments were done to validate the earlier results and determine if any modification were needed to the target. The following section describes the uranium ablation experiments in detail.

5.2.1 Initial Uranium Ablation Experiments

The initial uranium ablation experiments were performed using the smaller test chamber. A picture of the inside of the test chamber for this experiment is shown in Figure 5.1. A 2" by 2" copper catcher plate was placed 1.75" from the DU metal target. The target was moved during the irradiation in order to prevent the laser from drilling through the target. Moving the target also allowed for the focal length to be held at a constant value. Having the laser hit one spot creates a deep pit on the target, which in turn causes subsequent laser shots to hit the target with a different spot size. The pressure in the chamber was measured to be 6.3×10^{-5} Torr. 400 laser shots hit the uranium target over the course of the experiment. The copper catcher plate was removed from the chamber and counted using an Ortec Soloist Alpha Spectrometer. The detector was calibrated before counting the copper plate using a 5047 Bq calibrated Ra-226 alpha source. Based on these measurements, the amount of uranium measured on the catcher plate was 152 ± 5 μg. The mass ablated per laser shot was measured to be 379 ± 11 ng . This initial test was only able to measure the amount of uranium caught by the copper catcher. It did not measure the total uranium ablated from the uranium target. It was also not able to measure the distribution of the sputtered uranium on the catcher. An improved experiment was designed to measure the total amount of uranium ablated off of the target.

The second uranium ablation experiment was performed in order to measure the total mass of uranium loss during laser irradiation. A 2.1" by 2.1" aluminum catcher plate was placed 1.75" from the uranium target. In addition, 3 other aluminum plates were placed behind the target, above the target and below the target. The pressure in the chamber at the beginning of the laser shots was measured to be 2.5×10^{-4} Torr. There was a total of

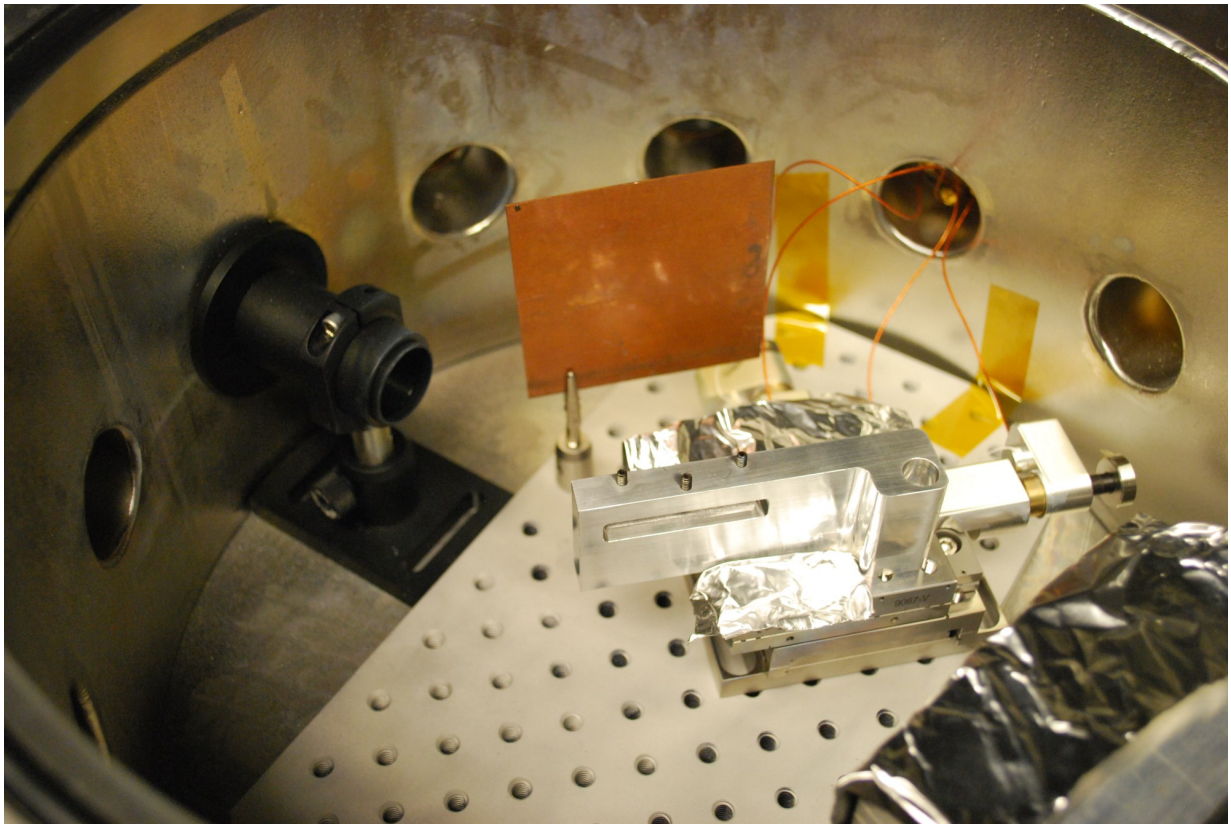

Figure 5.1: Picture of the test chamber setup for the initial uranium ablation experiment.

2042 shots on target. The laser was set at a repetition rate of 10 Hz for this test. Back reflections of the laser occurred during this experiment. These back reflection were due to an improper distance between the optical elements. Following the irradiation, the various aluminum plates were counted in both the Ortec Soloist Alpha Spectrometer and within a separate large vacuum chamber. The large vacuum chamber contained an Ortec B-Series Totally Depleted Silicon Surface Barrier Detector. The silicon detector had an active area of 150 mm^2 and a depletion depth of 200 μm. The distance between the aluminum catcher plate and the silicon detector was 23 cm. This distance allowed the catcher plate to be treated like a point source. From these measurements, the total ablated material on the catcher was found to be 1610 ± 70 μg. This corresponds to a mass ablation rate of 791 ± 36 ng per shot. The total mass measured on the top foil, bottom foil, and back foil combined was 344 ± 12 μg. Although this test was designed to measure the total amount of ablated material, it failed to capture all of the material shot off of the target. In addition, this test was not able to measure the sputtered uranium distribution on the catcher plate. The final

uranium ablation experiment within the small test chamber was preformed to correct for these issues.

The third uranium ablation experiment was designed to measure the total amount of ablated material along with the mass distribution on the catcher plate. A copper catcher plate measuring 2.1" by 2.1" was cut into 9 squares. These squares were then recombined to make the original square copper plate. The purpose for cutting the copper plate and recombining it was that each of the nine individual copper squares were to be measured independently to ascertain the total mass of uranium on each one. This information would allow for the sputtering distribution to be measured. The recombined copper square catcher was placed 1.70" from the uranium target. A five sided box made out of aluminum foil was made to be able to capture ablated material not traveling in the direction of the copper catcher plate. There was no hole on the side of the box to allow for the laser to enter and hit the uranium target. The hole was generated by the laser itself during the initial irradiation. The box was placed in the chamber and completely surrounded the uranium target. The laser was run at a 10 Hz repetition rate. The target was moved during the experiment in order to prevent the laser from cutting through the target. The initial pressure during this experiment was measured to be 3.5×10^{-4} Torr. A total of 1250 shots hit the target. A picture of the copper catcher plate with the copper segments labeled and the aluminum box unfolded following irradiation can be seen in Figure 5.2.

Following the laser irradiation, each of the copper squares were counted individually using the Ortec Soloist Alpha Spectrometer. Each side of the aluminum box were counted individually using the Ortec detector. Due the aluminum foils and the copper squares being distributed sources, a collimator was placed between the sources and the detector. A ^{226}Ra source was placed at various locations within the counting chamber to determine any changes to the efficiency based on location within the chamber. No significant differences in the efficiency were observed. The mass of ^{238}U found on each of the nine copper squares along with the aluminum foil box is shown in Table 5.2. The total mass of ablated ^{238}U found on the copper catcher plate was 1103 ± 16 μg. This corresponds to an activity of 13.7 ± 0.2 Bq. The total mass of uranium ablated per shot caught on the catcher plate, correcting for the ^{235}U content, was measured to be 883 ± 18 ng per shot. The total mass of ^{238}U collected on the aluminum foil box was found to be 988 ± 23 μg. This equates to 790 ± 26 ng of uranium per shot being collected on the aluminum foil, once again correcting for the ^{235}U content. One can conclude that roughly half of the ablated material is collected on the catcher plate located in the forward direction while the rest is distributed along the other four directions.

The plume distribution on the copper catcher plate can be seen by looking at the mass distribution on each copper segment. The majority of the ablated uranium was found on segment 5, which was the center segment. More ablated material was located on segment 4 versus segment 6. This suggests the plume was not centered on the copper catcher plate. In addition, segment 8 had more material than segment 2. Based on this result, the plume was centered on the lower left portion of the copper catcher plate compared to the center of the plate. This is clearly seen in Figure 5.2. 22% of the total ablated material was found on only 2 segments of the copper catcher which accounted for only 4.4% of the surface area of

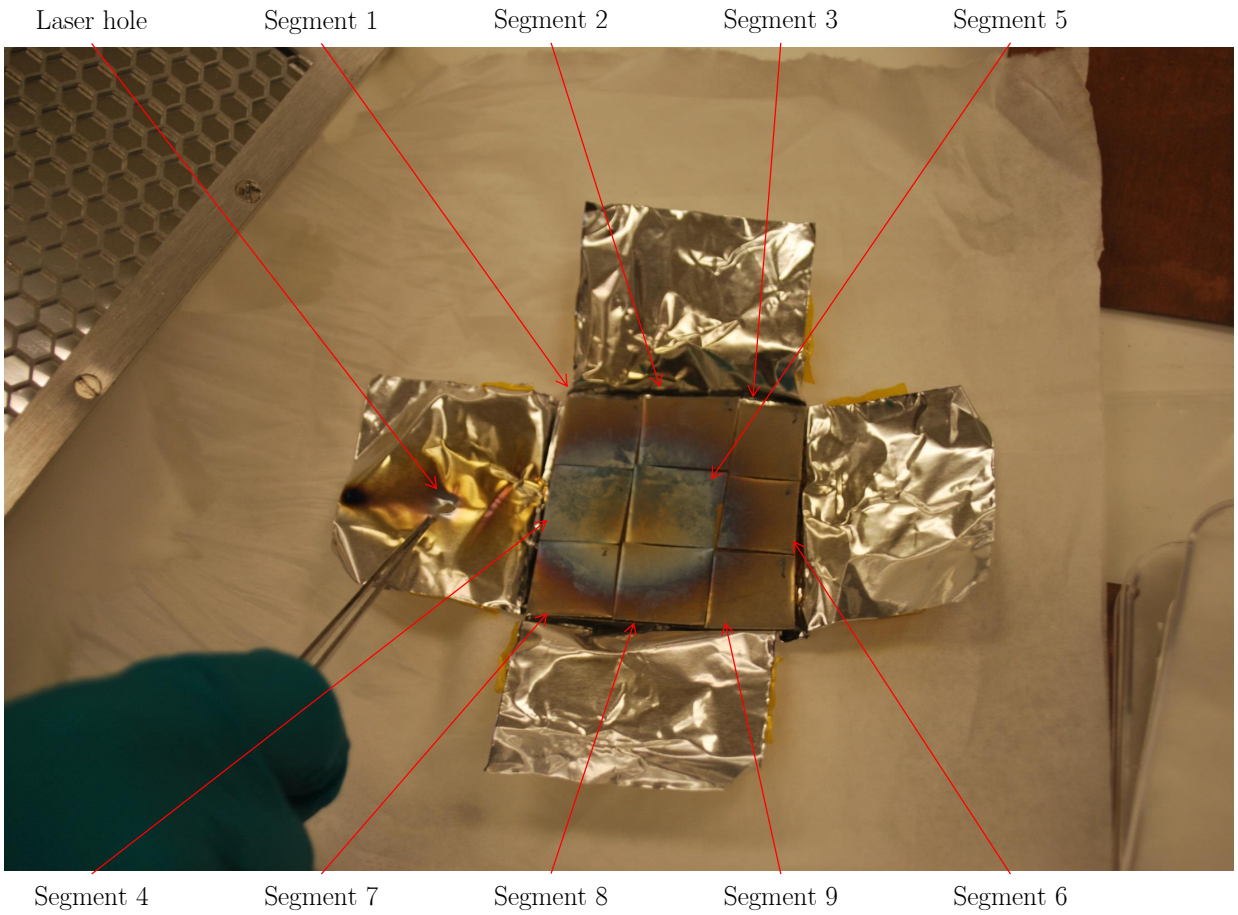

Figure 5.2: Picture of the segmented copper catcher following the third uranium ablation experiment. The discoloration on the copper shows where the ablated uranium landed. The aluminum box that completely covered the uranium target is unfolded. The tweezers are pointing to the hole made in the aluminum by the laser.

the box. This suggests that the uranium plume was forward peaked.

5.2.2 Uranium Ablation Validation Experiment

A uranium ablation experiment was performed using additive manufacturing (AM) sample 1 within the large experimental chamber. A copper catcher plate was used for this experiment. The uranium target was moved during the laser shots. The laser was set to a 10 Hz repetition rate for this experiment. The high repetition rate allowed for a significant amount of material to be ablated off the target. The laser pulse energy was 790 mJ and the spot size for the laser on target was approximately 50 μm by 100 μm. The target was irradiated for approximately 90 seconds for a total of 939 shots. Following the irradiation,

the catcher plate was removed from the chamber. The right side of the plate was significantly darker than the rest of the plate. The right side of the catcher plate being darker suggests that laser was not hitting the uranium at the proper angle. This condition was fixed in following experiments by adding a slight angle to the target holder.

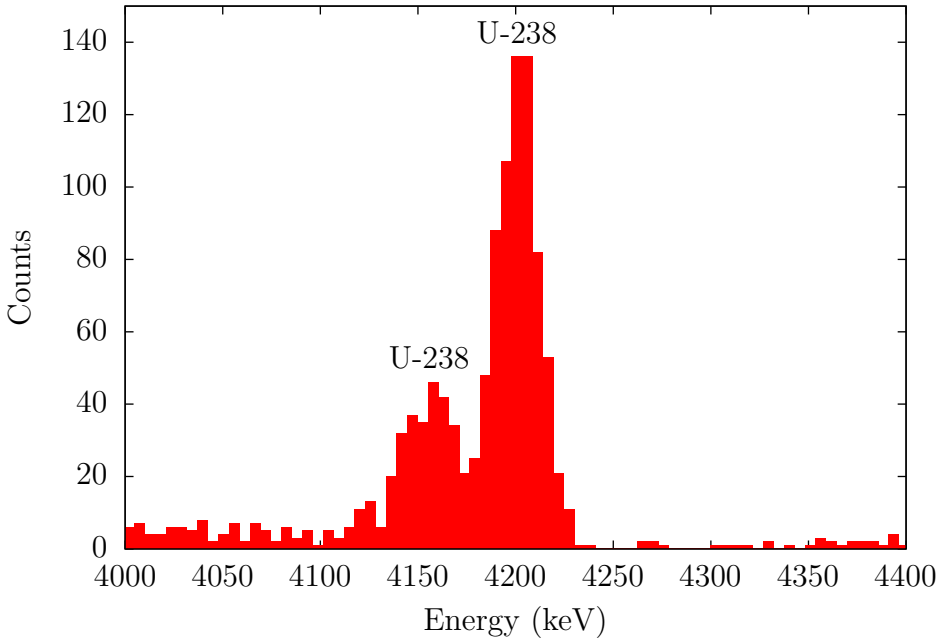

Figure 5.3: Alpha spectrum of the catcher plate following the uranium ablation experiment performed in the large experimental chamber. Both of the dominant alpha energies for ^{238}U are visible.

The catcher plate was moved to a separate vacuum chamber in order to perform alpha spectroscopy. A similar silicon detector to the one used during the initial ablation experiments was used to measure the alpha activity from the catcher plate. The energy calibrated alpha spectra from this measurement is shown in Figure 5.3. The catcher plate was counted in the vacuum chamber for 1 week. The low count rate was due to the small amount of ablated uranium on the catcher, the long half-life of ^{238}U, and the large distance between the catcher plate and the detector. The large distance was necessary in order to treat the catcher plate as a point source to allow for an accurate calculation of the amount of ablated material. Based on this spectra, the amount of ablated uranium on the catcher plate was determined to be 647 ± 23 μg. Since the sample was only 94% uranium, the total mass ablated was 733 ± 26 ng per laser shot. This compares favorably to the results from the previous uranium ablation experiments. The difference can be attributed to the smaller solid angle coverage due to the catcher plate being farther away from the target for the test within the large chamber.

5.3 Null Experiments

In order to determine if NEET of ^{235}U occurs, null tests were needed. A signal that looked like the decay of the isomeric state could possibly be created by other mechanisms not related to ^{235}U excitation. In order to exclude mechanisms not related to the excitation of ^{235}U, tests were performed on natural and depleted uranium samples. These samples had a concentration of ^{235}U that was over 100 times smaller than HEU samples. It was expected that no signal would be observed at these low concentrations of ^{235}U. If a signal was observed while testing natural or depleted uranium samples, tests on HEU samples would produce significantly larger signal. If the HEU targets did not produce a signal that scaled with the ^{235}U concentration, it could be deduced that the signal observed was due to mechanisms not related to NEET. The following section describes the initial null test experiments in detail along with what conclusions can be made about signals observed during the experiments.

5.3.1 Depleted Uranium Metal Experiments

The initial null tests were performed within the large experimental chamber. The setup for this experiment can be seen in Figure 3.7. The target was placed in a sample holder and held in place by a set screw. The sample holder slid into the target assembly that was attached to the translation stage within the chamber. The voltage of the electrostatic lens system for each of the null test experiments can be found in Table 5.3. The initial voltages for the electrostatic lens found in Table 5.3 were determined using SIMION as a guide. They were then optimized to maximize the measured signal of internal conversion electrons from ^{235m}U decay. The second set of voltages found in Table 5.3 were determined using the SIMION optimization program discussed in Section 3.4.1. The electronics setup used for these tests was the initial setup discussed in Section 3.6. As mentioned in that section, there were a lot of issues with the electronics. Unexpected current spikes would occur suggesting sparking within the chamber. The 440 V difference between the catcher plate and the lens grid caused a spark that would trip off the grid. For this reason, the grid was turned off until the catcher was in position. For all of the tests, the focusing lens was attached to a manual translation stage. A gauge with a resolution of 0.001" was connected to measure the change in position of the lens when the lens translation stage was moved. The tests were performed in vacuum with the pressure being less than 5×10^{-7} Torr. The analysis of the data from the null tests was done using ROOT [70]. Before the uranium test was performed, a test run using aluminum was performed. This was to test the movement of the target translation stage in addition to determining the spot size of the laser. The aluminum test produced an elliptical pit with dimensions 50 μm by 100 μm. This was the spot size of the laser. Following the aluminum test, the sample labeled DU metal was placed into the target holder and the chamber was pumped down to vacuum.

The DU metal experiment consisted of four experimental runs. All of the runs used copper as the catcher plate. The initial run consisted of 40 shots on target with the pressure in the chamber being less than 1×10^{-7} Torr. The target was not moved during the initial

Catcher Name	Material	^{238}U Mass (μg)	^{238}U Activity (Bq)
Box 1	Aluminum	448 ± 18	5.57 ± 0.23
Box 2	Aluminum	119 ± 8	1.48 ± 0.10
Box 3	Aluminum	270 ± 9	3.36 ± 0.11
Box 4	Aluminum	151 ± 7	1.87 ± 0.09
Box Total	Aluminum	988 ± 23	12.3 ± 0.3
Segment 1	Copper	85.9 ± 4.1	1.07 ± 0.05
Segment 2	Copper	99.0 ± 3.0	1.23 ± 0.04
Segment 3	Copper	43.8 ± 1.4	0.544 ± 0.018
Segment 4	Copper	208 ± 7	2.58 ± 0.08
Segment 5	Copper	256 ± 10	3.18 ± 0.12
Segment 6	Copper	112 ± 4	1.40 ± 0.05
Segment 7	Copper	102 ± 4	1.26 ± 0.06
Segment 8	Copper	140 ± 6	1.74 ± 0.07
Segment 9	Copper	57.2 ± 2.4	0.711 ± 0.030
Catcher total	Copper	1103 ± 16	13.7 ± 0.2

Table 5.2: Mass distribution found on the copper catcher plate and the aluminum box used during the third uranium ablation experiment performed in the test chamber.

	Electrostatic lens voltage (V)						
Test Name	Catcher	Grid	Ring 1	Ring 2	Ring 3	Ring 4	Ring 5
DU metal	-240	200	-60	-20	1	1	-140
NU ceramic 1	-240	200	-60	-20	1	1	-140
NU ceramic 2	-240	200	-60	-20	1	1	-140
AM metal	4	0	-30	-5	3000	0	-140

Table 5.3: List of the voltages found on each component of the electrostatic lens during the initial null tests. For the DU metal test, NU ceramic 1 test, and the NU ceramic 2 test, the voltages for the lens were chosen to maximize the signal from ^{235m}U decay. The voltages used during the AM metal test were determined using the optimization program discussed in Section 3.4.1.

run, all of the shots hit the same spot. Figure 5.4 shows the decay spectrum from the initial run. The laser shots started at time zero and were finished within the first minute. Part (a) of the figure shows the initial 5 minutes of the test. One can see a large number of counts were measured in the detector when the laser shots were occurring. This can be attributed to the light generated by the plasma causing the MCP detector to fire. The catcher plate was moved to the top of the chamber during the second minute of the test and the lens grid was turned on by the third minute. Part (b) of the figure shows the decay spectrum for 200 minutes. There are some notable features of the spectrum. First, one can see spikes occurring in the spectrum. These spikes are most likely due to sparking within the chamber. Additionally, there is a decay observed within the spectrum. This decay of the signal cannot be fit with one exponential. In fact, it takes two or more exponential curves to fit the data. The fitting equations used for these data were

$$\begin{aligned} Counts = N_1 \exp\left(\frac{-\ln(2)t}{T^1_{1/2}}\right)\left(1-\exp\left(\frac{-\ln(2)}{T^1_{1/2}}\right)\right) \\ +N_2 \exp\left(\frac{-\ln(2)t}{T^2_{1/2}}\right)\left(1-\exp\left(\frac{-\ln(2)}{T^2_{1/2}}\right)\right)+B, \end{aligned} \tag{5.1}$$

and

$$\begin{aligned} Counts = N_1 \exp\left(\frac{-\ln(2)t}{T^1_{1/2}}\right)\left(1-\exp\left(\frac{-\ln(2)}{T^1_{1/2}}\right)\right) \\ +N_2 \exp\left(\frac{-\ln(2)t}{T^2_{1/2}}\right)\left(1-\exp\left(\frac{-\ln(2)}{T^2_{1/2}}\right)\right) \\ +N_3 \exp\left(\frac{-\ln(2)t}{T^3_{1/2}}\right)\left(1-\exp\left(\frac{-\ln(2)}{T^3_{1/2}}\right)\right)+B, \end{aligned} \tag{5.2}$$

where $N_1/N_2/N_3$ are the initial number of decaying systems, $T^1_{1/2}/T^2_{1/2}/T^3_{1/2}$ are the half-lives for the decay, and B is the background. The reduced χ^2 for the two exponential and the three exponential fits are shown in Figure 5.4 and are 1.71 and 1.68 respectively. The data was fit starting 5 minutes after the last laser shot. Fitting the spectrum with either the three exponential fit or the two exponential fit yielded large values for the reduced χ^2. The half-lives from the two exponential fit are 3.49 ± 0.14 min and 20.6 ± 0.7 min. The half-lives from the three exponential fit are 3.01 ± 0.27 min, 11.2 ± 4.0 min, and 28.5 ± 7.5 min. The three exponential fit does have a half-life that is similar to ^{235m}U. However, the uncertainty in that value is large and the reduced χ^2 is poor. The large χ^2 suggests that the data was not purely statistical and may possibly have more decay components. As mentioned earlier, sparking was occurring during the run. In addition, if the electronic setup was not stable, that could introduce noise and create nonstatistical counts in the spectrum. What is clear from the data is that there are multiple decays occurring in the spectrum. What causes

these decays is important to understand since they need to be eliminated in order to observe the 26 minute half-life of ^{235m}U.

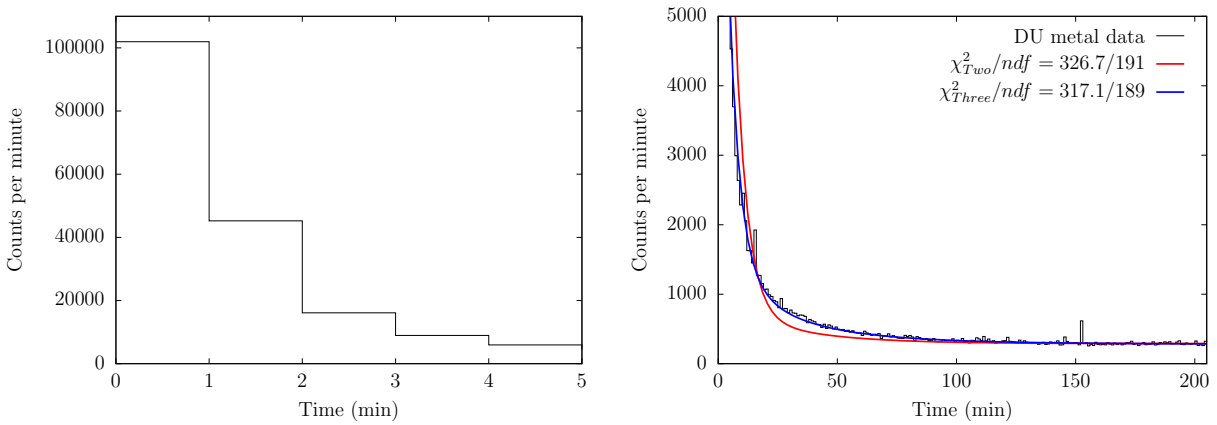

(a) (b)

Figure 5.4: The spectrum labeled (a) shows the first 5 minutes of the DU metal null test. The laser shots occurred during the first minute. The spectrum labeled (b) shows the entire decay for the test. The two exponential and the three exponential fits are shown in red and blue respectively.

There are multiple mechanisms that can cause the observed decays. The first mechanism, exoelectron emission, was briefly described in Section 2.6.1. These are low energy electrons emitted by a surface as it relaxes after the surface undergoes a perturbation. The emission of these electrons would decay over time as the surface relaxes back to its natural state. In the case of the DU metal experiment, there was no method to prevent exoelectron emission. The only method used to mitigate the effect was the copper catcher plate. Exoelectron emission is strongly influenced by oxide layers so copper was chosen since it oxidizes slower than aluminum. In addition to exoelectron emission, the light from both the scattering of the IR laser beam and the UV light generated by the plasma have an effect on the MCP detector. This was evident when shots were performed on metal targets with the catcher plate located at both the top and the bottom of the chamber. A decay signal was observed that could not be attributed to exoelectron emission. A third possible source for the decaying signal is the MCP detector response to changing pressure. The movement of the catcher plate from using the translation arm introduces a small amount of air into the chamber. Additionally, the shooting of the targets also increases the pressure within the chamber. The pressure increase is short due to the turbomolecular pump. A test was performed to understand the MCP detectors response to pressure. A small amount of argon gas was introduced into the chamber while the MCP detector was on. There was no observed change in the count rate suggesting that pressure differences were not a source of the decay signal.

What is clear from the first measurements using depleted uranium metal is that there are

decays that occur that are not due to ^{235m}U. The very first experiment performed looking for NEET of ^{235}U described in Section 2.6.1 used a natural uranium metallic sample [33]. The claim from that experiment was that NEET was observed at a very high excitation rate. What is clear from the data in that measurement is that there were multiple decays observed. A fast decays was observed along with a slow decay. This previous result is very similar to the current result found during the initial tests using depleted uranium metal. The half-lives observed during the depleted uranium tests do not match the 26 minute half-life of ^{235m}U. Although the sample used had half as much ^{235}U as the experiment performed in 1979, no clear signal was observed. This suggests two possibilities. First, the plasma conditions during the depleted uranium tests were not similar to the conditions found in [33] and thus the reaction was off resonance so that no ^{235m}U was created. While it is likely the plasma conditions were not perfectly matched, the second possibility is more likely. The observation of NEET found in [33] is actually either exoelectron emission or due to their detector's response to the light generated during the measurement.

5.3.2 Natural Uranium Ceramic Experiments

In order to have a null test with equivalent properties to the enriched ceramic puck that was made, two natural uranium (NU) ceramic pucks were used. The samples were not robust and caused many problems. As mentioned above, they were brittle and chalky. In addition, they had poor heat conductivity. This made them unable to withstand the laser over the course of numerous experimental runs. Figure 5.5 shows a picture of the natural uranium ceramic after laser irradiation. One can see a hole was drilled into the target after only 200 laser shots. Because of their inability to survive numerous laser shots, only a few runs were performed on each target. Four runs were performed using the sample called natural uranium ceramic 1 and three runs were performed on the sample called natural uranium ceramic 2. The lens system voltages for these tests can be seen in Table 5.3. The targets were placed in a target holder designed to hold the pucks and were held in by a faceplate in order to prevent the puck from cracking and falling out of the target holder. The natural uranium ceramic targets were irradiated by 15 to 30 laser shots per test run. The targets were translated during the runs in order to expose a clean surface for each shot. An example decay spectrum for a natural uranium ceramic run is seen in Figure 5.6.

Once again, multiple decays were observed in the spectra. Both the two exponential fit and the three exponential fit have large reduced χ^2. Spiking is still visible in the spectrum. The spiking made fitting the data difficult. The three exponential fit is significantly better than the two exponential fit, although it still has a large reduced χ^2. The half-lives for the fit are 1.13 ± 0.29 min, 10.5 ± 1.1 min, and 91.8 ± 5.9 min. Similar to the DU metal target, there is a short decay of order a couple of minutes and there is a decay with a half-life of around 10 minutes. A major difference between the DU metal data and the NU ceramic data is the long decay for the ceramic data. The existence of a long decay makes seeing a 26 minute half-life in the data difficult, especially if the amount of ^{235m}U expected to be created is small. After improvements were made to the electronics, the sample called NU ceramic 2

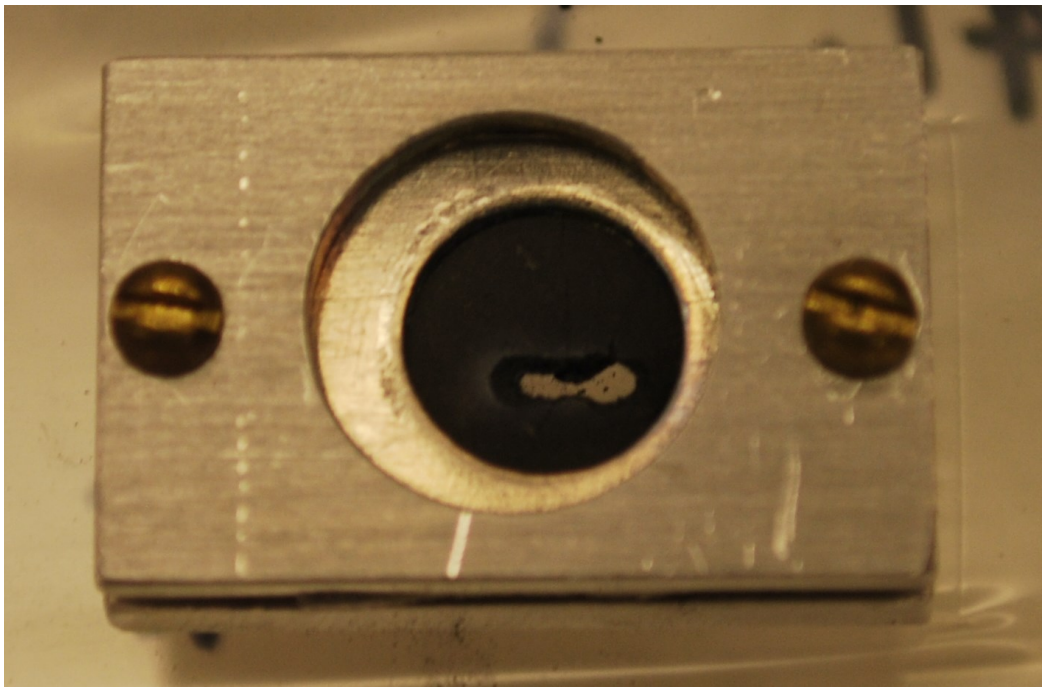

Figure 5.5: Picture of the natural uranium ceramic in the target holder after laser irradiation.

was irradiated by the laser. The sample was moved during irradiation and a total of 30 shots hit the target. A decay spectrum was observed and is shown in Figure 5.6. The fit for the spectrum starts 5 minutes after the final laser shot. One can see that this spectrum extends for hours following the laser shots. This allowed for the background to be established and helped determine if there was a long decay component. Once again, the spectrum consisted of three exponential decays with half-lives of 2.54 ± 0.34 min, 12.6 ± 1.9 min, and 70.1 ± 6.5 min. A long decay is evident in the spectrum. There is no evidence of a 26 minute decay in the spectrum.

5.3.3 Additive Manufacturing Metal Experiments

Following the natural uranium ceramic experiments and prior to the additive manufacturing experiments, attempts were made to reduce the decay signals observed in the spectra. The first change to the experimental setup was the inclusion of an aluminum baffle. For both the DU metal experiments and the NU ceramic experiments, light was able to reach the MCP detector. As described in Section 3.3, a baffle was added to limit the amount of light hitting the detector during the laser shots. The addition of the baffle significantly reduced the signal observed in the detector during the laser shots. The second improvement

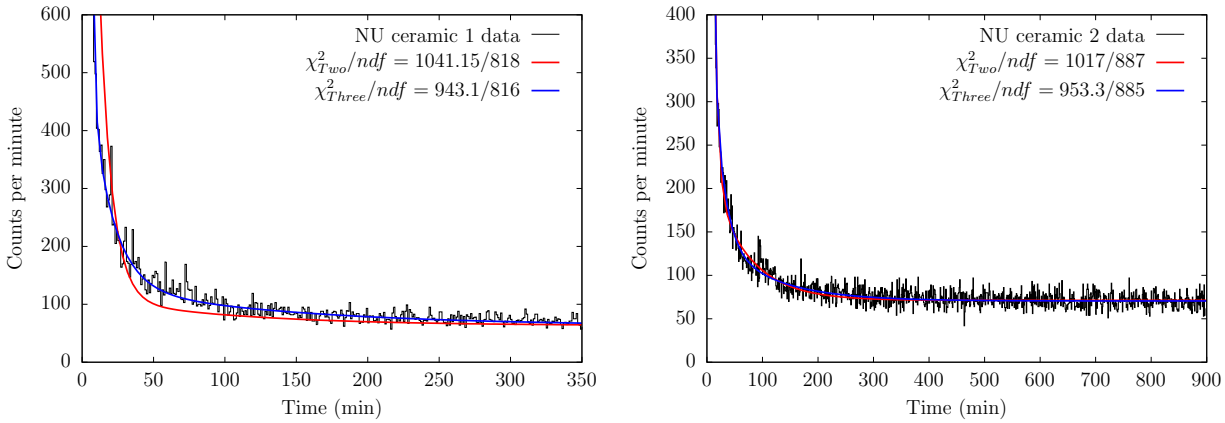

(a) NU ceramic 1

(b) NU ceramic 2

Figure 5.6: Example spectra from the NU ceramic experiments. The two exponential fit and the three exponential fit are shown in red and blue respectively.

to the experimental setup was the optimization of the electrostatic lens. The optimization procedure is described in Section 3.4.1. It was thought that some if not all of the decay signals observed were due to exoelectrons. The prior electrostatic lens setup was designed for maximum efficiency of observing electrons from the catcher plate. If there were exoelectrons emitted by the catcher plate, the lens would focus them onto the detector. In addition, the original lens setup had a very high efficiency for electrons with energies below 10 eV. In order to prevent very low energy electrons from leaving the catcher plate, a small positive voltage was applied. The new electrostatic lens voltages did improve the observed decay spectra. While the total efficiency of the setup was decreased, the new voltages significantly lowered or eliminated the signal from the long decay seen in previous spectra. The third improvement made to the setup was the modification of the electronics. The biggest change was the use of the Mesytec MSCF-16 shaper. This vastly improved the signal sent to the ADC and the idea was that this could eliminate some of the problems that may have caused nonstatistical counts in the spectrum. The last change made to the setup was the replacement of the copper catcher plates with a gold coated copper catcher plate. Since exoelectron emission is related to the oxidation of the surface, it was thought that using a gold catcher plate would improve the spectra. Experiments were performed on pure gold foil and the results demonstrated that using gold resulted in smaller decay signals compared to copper catcher plates. Because of these results, copper catcher plates were then coated with a thick gold layer. All catcher plates used for the rest of the experiment were gold coated copper catcher plates. Following these improvements, the uranium sample labeled AM metal was placed in the target holder.

An example spectrum from an AM metal experiment is seen in Figure 5.7. For this experiment, a gold coated copper catcher plate was used. A total of 38 laser shots hit the

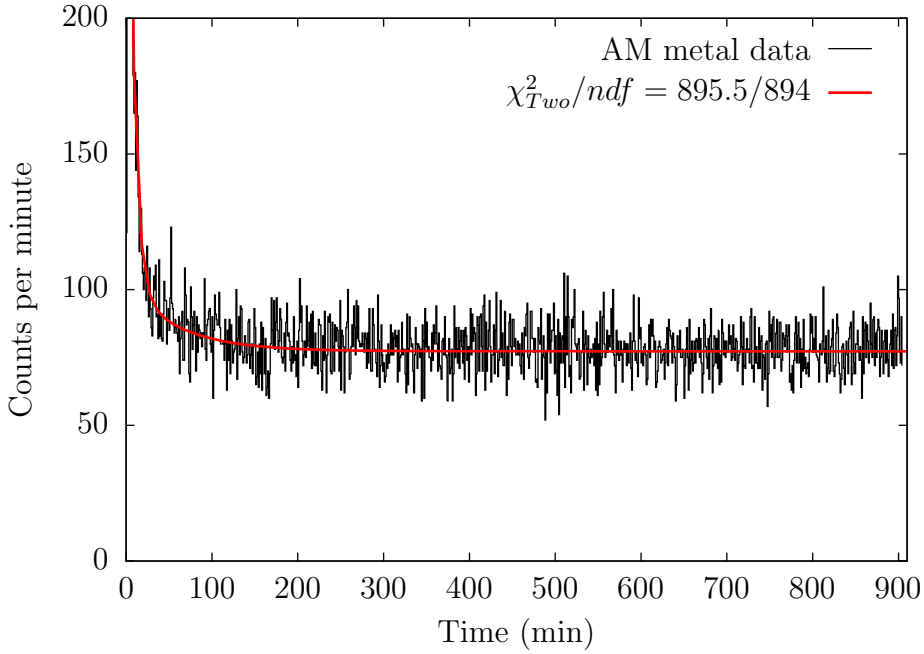

Figure 5.7: Decay spectrum from AM metal experiment. Only a two exponential fit was used due to the lack of a long decay signal.

target. The target was translated during the laser irradiation. Both a two exponential and three exponential fit of the resulting spectrum were performed. Time zero for the data corresponds to the start of the laser shots. There was no observed third decay signal. The lack of the third decay suggests that the improvements made to the setup either completely eliminated the cause of the long decay or at the very least minimized the effect to the point that the decay was below the detectable limit. In addition, the reduced χ^2 for the fit was vastly improved compared to the earlier measurements. The nonstatistical events were no longer observed in the spectra. The long count time for the AM experiments also helped to better understand the background in the detector. Even with the improvements to the setup, two decays were still visible. The fast decay with a half-life of 4.6 ± 0.7 min and a slower decay with a half-life of 40.9 ± 10.7 min. The decays measured during the AM experiments also consisted of both a fast and slow decay. Although still visible, the initial count rate for both of the observed decays was greatly reduced in the AM experiments compared to the earlier experiments. It is clear that the changes made to the experimental setup greatly improved the sensitivity of the measurement.

The long count time for the AM experiments was valuable because it allowed for the determination of the efficiency of the MCP detector in seeing an alpha decay event. In order to determine this quantity, the background on the catcher plate before and after the uranium ablation validation experiment was measured. There was an increase in the background rate of 3.5 Hz after 939 shots. Combining this data with the data obtained by alpha counting

the catcher plate yielded an alpha decay detection efficiency of 44%. This efficiency was used along with the known isotopics of the targets to predict the increase in background from each experimental run. This information was useful in determining problems with the enriched uranium metal experiment described in Chapter 6.

A total of 12 experimental runs were performed using the AM target. No 26 minute decay was observed in any of the spectra from those runs. The AM metal target did contain the least amount of ^{235}U out of all the targets used during this experiment. However, if the results from the 1979 uranium NEET experiment are correct, the isomer decay signal should have been observed even with the reduced ^{235}U content of the sample. There was no evidence of the isomer. More importantly, with all of the improvements made to the experimental setup, decays were still observed. These decays had half-lives that were close to the ^{235m}U half-life. This further bolsters the idea that previous observations of ^{235}U NEET are due to mechanisms unrelated to the NEET process. This is especially true for the experiment found in Arutyunyan et al. using the high energy electron gun [35]. In their data, they had measured half-lives spanning 18 minutes up to 44 minutes with large uncertainties. Their claim that NEET was observed lacks credibility when other mechanisms can create decays with similar half-lives to ^{235m}U in the spectrum.

Chapter 6

Initial Enriched Uranium Experiments

Enriched uranium samples were used in order to have the highest sensitivity for seeing NEET of ^{235}U. This chapter describes the enriched uranium samples in detail. The experiments performed on the enriched uranium oxide and enriched uranium metal samples are discussed along with the decay signals observed. The problems encountered during the initial enriched uranium experiments were similar to the problems encountered during the initial null test experiments. The knowledge gained from both the initial null test experiments and the initial enriched uranium experiments improved the experimental setup for the final set of experiments involving uranium carbide.

6.1 Enriched Uranium Samples

Multiple samples of enriched uranium were obtained for the experiment. The difficulty in obtaining enriched uranium was compounded by the fact that the uranium had to be highly enriched uranium (HEU) with ^{235}U content higher than typical samples of HEU. Typical HEU samples with a large proportion of ^{235}U have an enrichment around 93%. The problem with using 93% enriched uranium is that the enrichment process significantly increases the relative amounts of ^{236}U and ^{234}U. Both ^{236}U ($T_{1/2} = 2.342 \times 10^7$ yr) and ^{234}U ($T_{1/2} = 2.455 \times 10^5$ yr) have significantly shorter half-lives compared to ^{238}U ($T_{1/2} = 4.468 \times 10^9$ yr) and ^{235}U ($T_{1/2} = 7.04 \times 10^8$ yr). The increase in activity due to the other uranium isotopes posed a problem for the experiment. Alpha particles leaving the surface of the catcher plate would knock out electrons. These electrons would be accelerated and focused onto the detector and would contribute to the background. Because of this, the activity of the uranium on the catcher plate had to be minimized. The specific activity for a sample of uranium enriched to 99.44% is 178 Bq/mg with the isotopics given in Table 6.1. This can be compared 2400 Bq/mg, which is the specific activity for a sample of uranium enriched to 93%. The alpha activity on the catcher plate would be 10 times larger using uranium

that is 93% enriched compared to 99.4% enriched mostly due to the ^{234}U content. Because of this, efforts were made to obtain greater than 99% enriched uranium in order to avoid a large alpha induced background on the catcher plate. Table 6.1 shows the isotopics for the enriched uranium samples used during the experiment.

Sample Name	Form	Mass (g)	^{234}U	^{235}U	^{236}U	^{238}U	Specific Activity (Bq/mg)
HEU ceramic	Ceramic	0.275	0.0379	99.44	0.47	0.0497	178
HEU metal	Metal	0.299	1	93	0.5	5.5	2400
HEU carbide	Ceramic	0.290	0.0379	99.44	0.47	0.0497	178

Table 6.1: Enriched uranium samples used during the experiment. The mass fraction isotopics for each sample are given.

The first sample of enriched uranium obtained was an oxide powder. Little was known about the history of the powder, but it consisted of a mixture of uranium oxidation states. Subsequent alpha spectroscopy and mass spectrometry of the sample determined it had an enrichment of 99.44% ^{235}U. A portion of this material was then made into a target. The material was turned into UO_2 powder before being pressed and sintered. The material was then formed into a mixed oxide ceramic puck using the same method used to make the natural uranium ceramic pucks described in Chapter 5. The puck was 1 mm thick and had a diameter of 10 mm. The mass of the puck was 274.6 mg, giving the puck a density of 3.5 g/cm^3. This density is significantly less than uranium's theoretical metal density of 19 g/cm^3. Similar to the natural uranium ceramic pucks, the enriched uranium ceramic puck was brittle and lacked heat conductivity. It was not as chalky as the natural ceramic pucks. While both the natural uranium and enriched uranium ceramic pucks were formed using the same procedure, the natural uranium UO_2 powder had a different particle size compared to the enriched UO_2 powder. This difference in particle size would explain why the natural uranium ceramic puck was far more chalky and not as mechanically stable as the enriched ceramic puck. A picture of the enriched uranium ceramic puck can be seen in Figure 6.1.

Due to the brittleness and lack of heat conductivity for the ceramic target, a metal target was required to continue the experiment. It was not possible to make a metal target using the 99.4% uranium powder. Because of this, a 2 g sample of 93% enriched uranium metal was procured. The exact isotopics for the sample was not known, but the nominal isotopics given in Table 6.1 are a reasonable estimation. Multiple smaller samples were cut from the larger sample. Due to mass and activity limitations of the laboratory, the sample size was limited to below 440 mg. The first and only sample received had a mass of 299 mg. The sample was shaped like a half moon with approximate dimensions of 8 mm by 2 mm by 2 mm. It was known that the uranium sample was going to be cut within a glove box that was plutonium contaminated. Any form of plutonium contamination of the target would introduce excess activity on the sample. Under laser irradiation, the plutonium would ablate onto the catcher

(a) ^{235}U ceramic (b) ^{235}U metal

Figure 6.1: Pictures of the enriched uranium ceramic and the enriched uranium metal targets. The ceramic target is held within its target holder. The picture of the metal target is after the target was cleaned in nitric acid.

plate and introduce a background. Since the half-life of ^{239}Pu is 24,110 years, a small amount of ablated plutonium would cause a large increase in the background due to alpha decay. After the sample was cut, it was sent to the chemistry building. Once there, the sample was cleaned using a strong nitric acid solution in order to dissolve the oxide layer. It was thought that the plutonium existed on the oxide layer and that the cleaning of the surface would remove the plutonium contamination. A picture of the uranium sample following the nitric acid cleaning is seen in Figure 6.1. The clean metal surface free of black oxide is visible.

The last sample of enriched uranium used during the experiment was composed of enriched uranium carbide. It was produced using the same method used to create the depleted uranium carbide target. The sample was made using the 99.4% enriched uranium oxide powder mixed with graphite. The sample's mass was 290 mg and it had a hemispherical shape. The target mostly consisted of UC, but also contained UC_2 and U_2C_3. For the results using this sample, it was assumed the sample was composed of equal amounts of UC and UC_2 in order to calculate the amount of uranium ablated with each laser shot. Figure 6.2 shows a picture of the sample in the target holder. Unlike the depleted uranium carbide sample, the enriched uranium carbide sample was not broken apart.

6.2 Enriched Uranium Experiments

Experiments using the enriched uranium samples were done to look for the signature of NEET. The enriched uranium experiments for each target were performed using the same experimental conditions and the same experimental setup as their corresponding null test

Figure 6.2: Picture of the enriched uranium carbide sample held in the target holder.

experiments. Multiple experimental runs were performed for each sample. All of the data from these experiments were fit using ROOT and Equations 5.1 and 5.2.

6.2.1 Enriched Uranium Ceramic Experiments

The first enriched uranium sample obtained was the enriched uranium ceramic puck (HEU ceramic). The enriched uranium ceramic puck suffered the same problems that the natural uranium ceramic pucks had. It was not able to withstand the laser shots due to its poor heat conductivity, low density, and brittleness. For these reasons, only a few experimental runs using the target were possible. The last run using the target formed a hole. The laser pulses began to irradiate the aluminum backing causing aluminum to coat the backside of the target and the surface of the hole. No further runs were done using the target once the aluminum coating formed. For the HEU ceramic target, the experimental runs were conducted using the exact same conditions and experiential setup as the natural uranium ceramic experiments. Two series of experimental runs occurred. The first series of runs were conducted using the same setup as the NU ceramic 1 runs. The second series had the same setup as the NU ceramic 2 runs. The HEU ceramic 1 run consisted of 23 laser shots with the target moved during the laser irradiation. The HEU ceramic 2 run consisted of 41 laser

shots with the target moved during the laser irradiation. Example decay spectra using the HEU ceramic target for both experimental run conditions are shown in Figure 6.3. Time zero corresponds to the start of the laser shots. The fit begins 5 minutes after the last laser shot.

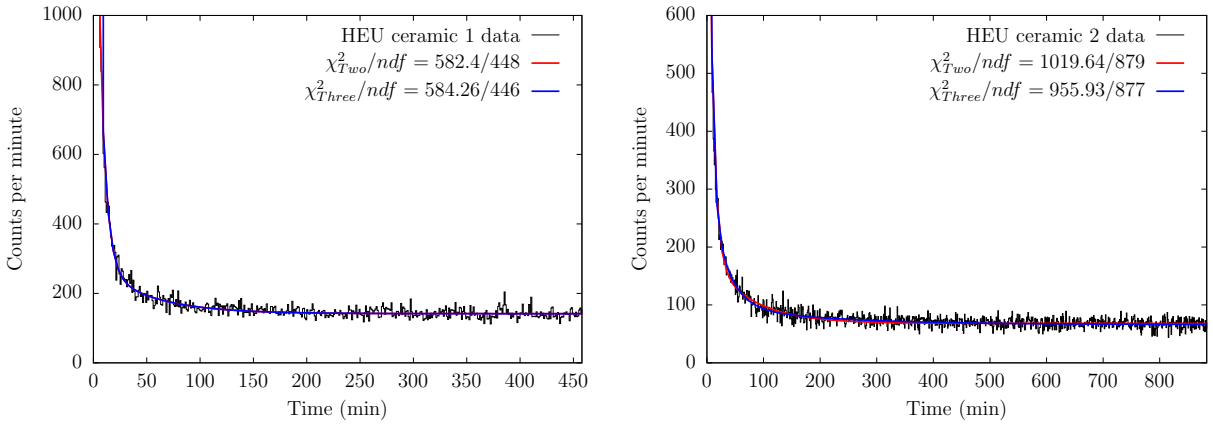

(a) HEU ceramic 1

(b) HEU ceramic 2

Figure 6.3: Example spectra from the HEU ceramic experiments. The two exponential fit and the three exponential fit are shown in red and blue respectively.

The enriched uranium ceramic data suffered from the same problems that plagued the natural uranium ceramic data. Spikes were observed along with unexpected rises in the data. These nonstatistical effects caused problems with fitting the data. Both spectra have poor reduced χ^2 values. The HEU ceramic 1 experimental run was best fit by only two half-lives. The half-lives found from the fit are 4.09 ± 0.27 min and 33.9 ± 3.6 min. For the experimental run called HEU ceramic 2, the three exponential fit had the lowest reduced χ^2. The half-lives from the fit are 3.49 ± 0.44 min, 19.66 ± 3.0, and 130 ± 33 min. Comparing the half-lives found for HEU ceramic 1 to the half-lives from NU ceramic 1 show a major discrepancy. Both the fast and slow decays seen in the HEU ceramic 1 data are significantly different than the half-lives found in the NU ceramic 1 data. The same is also true for the HEU ceramic 2 data compared to the NU ceramic 2 data. The three half-lives found were significantly different.

There are a few possible causes for this discrepancy. First, the nonstatistical counts found in all 4 spectra would affect the fit results. All of the spectra shown have a poor reduced χ^2 because of the spikes in the data along with the nonstatistical rises. The poor fits coupled with small count rates make the half-lives measured by the fit highly dependent on the point in the data where the fit starts. A second possible cause of the discrepancy is a difference in the target itself. While both the natural uranium ceramic and the enriched uranium ceramic were made using the same procedure, the targets were not exactly the same. The grain size for the enriched UO_2 powder was different than the grain size for the natural uranium

powder. More importantly, the amount of oxygen found in the targets were different. This is clear from the difference in density between the enriched uranium ceramic and the natural uranium ceramic. This could affect the electron emission from the catcher plate surface. The final possible cause of the discrepancy is that there was a production of ^{235m}U that was decaying. The extra decay would combine with the previous measured decay that was around 10 minutes to produce a longer half-life. While it is possible that the isomer was generated, the other possible causes for the discrepancy would make any conclusion formed using the ceramic data suspect.

Even with poor fits, the data did not contain a clear 26 minute half-life. The enriched uranium ceramic contained a higher proportion of ^{235}U than the sample used in the first experiment looking for NEET of ^{235}U [33]. However, there was no clear evidence of ^{235m}U decay in the ceramic data. In addition, the multiple decays observed using the enriched uranium ceramic were possibly also observed in the electron gun experiment [35]. Their results were only fit with one exponential, but they may have produced better fits with multiple exponential decays. Due to the nonstatistical counts within the data, the enriched uranium ceramic data is of limited utility. However, the results using the ceramic target offer additional evidence that the previous measurements of NEET of ^{235}U are not repeatable.

6.2.2 Enriched Uranium Metal Experiments

The second enriched uranium experiment used the 93% enriched uranium metal sample. The experimental setup and conditions were similar to the depleted uranium binary experimental runs. A gold coated copper catcher foil was used for all of the experimental runs. Each experimental run consisted of between 20 and 40 laser shots with the metal target translated during the laser shots. An example spectrum using the HEU metal sample is seen in Figure 6.4. A total of 29 laser shots were performed for the experimental run. The voltage on the electrostatic lens was the same as the voltage used during the AM metal run using the depleted uranium binary metal sample. The spectrum had one spike that lasted for two minutes that occurred 40 minutes after the laser irradiation. It is not known what caused this one spike. Both a two exponential and a three exponential fit were performed on the data with the spike in the data excluded from the fit. The two exponential fit has a better reduced χ^2 than the three exponential fit. In addition, the reduced χ^2 for the fit is very good with the data spike excluded. The half-lives from the fit are 1.73 ± 0.55 min and 16.4 ± 3.0 min. Neither of the half-lives measured are close to the 26 minute half-life of ^{235m}U. These half-lives compared to the half-lives found during the AM metal experimental run of 4.6 ± 0.7 min and 40.9 ± 10.7 min once again show a discrepancy. This discrepancy could be due to the difference between the targets. The HEU metal sample was a pure uranium sample, while the AM metal sample was a uranium binary.

The data obtained during the first two experimental runs were unusual. It was known that the 93% enriched uranium would create a large background mostly due to the ^{234}U content. After two experimental runs, the measured background in the detector was higher than expected. The chamber was then opened to determine the cause of the extra background.

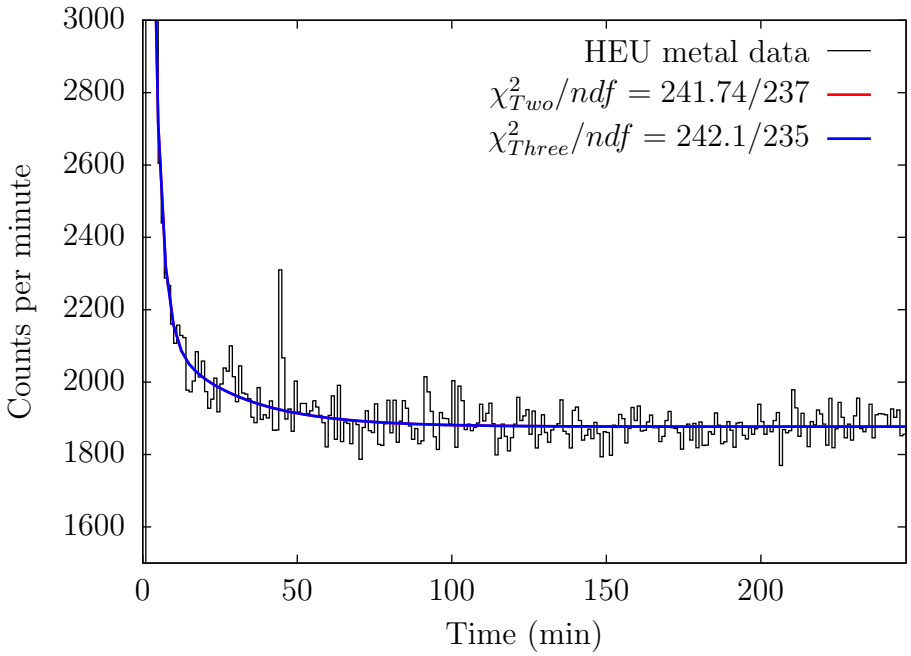

Figure 6.4: Decay spectrum from the HEU metal experiment.

The catcher plate was removed from the chamber and was swiped with a piece of paper. The swipe was placed in the Soloist Alpha Spectrometer in order to perform alpha spectroscopy of the material on the catcher plate. The alpha spectrum observed is shown in Figure 6.5. What is clear from the spectrum is that the metal target still had a significant amount of plutonium activity on it after the nitric acid cleaning. The plutonium was then ablated off of the surface during the laser irradiation and coated the catcher plate. Because of the high specific activity of plutonium, many of components in the chamber that were contaminated were eventually replaced in order to reduce the background within the chamber. In addition to discovering the contamination, opening the chamber following the first two experimental runs revealed that the metal target was able to withstand the laser shots and did not suffer the same problems the ceramic targets had. A picture of the uranium metal target following laser irradiation is shown in Figure 6.6. The metal is clearly visible where the laser shots occurred with the black uranium oxide layer visible along the edges.

There was no clear signal of the isomer in the data from the HEU metal experiments. It is possible the slower decay could hide the signal, which would suggest a small excitation rate. The large background due to the alpha decay of both ^{234}U and ^{239}Pu also limit the ability to see the isomeric decay in the data. With these limitations, what can be concluded using the HEU metal data is that the large NEET excitation rate measured in [33] was not observed. The HEU metal sample contained 130 times more ^{235}U than the sample used during the Izawa and Yamanaka experiment, yet no clear signal was observed. This furthers the point that the first claimed observation of NEET in ^{235}U was in fact not due to NEET.

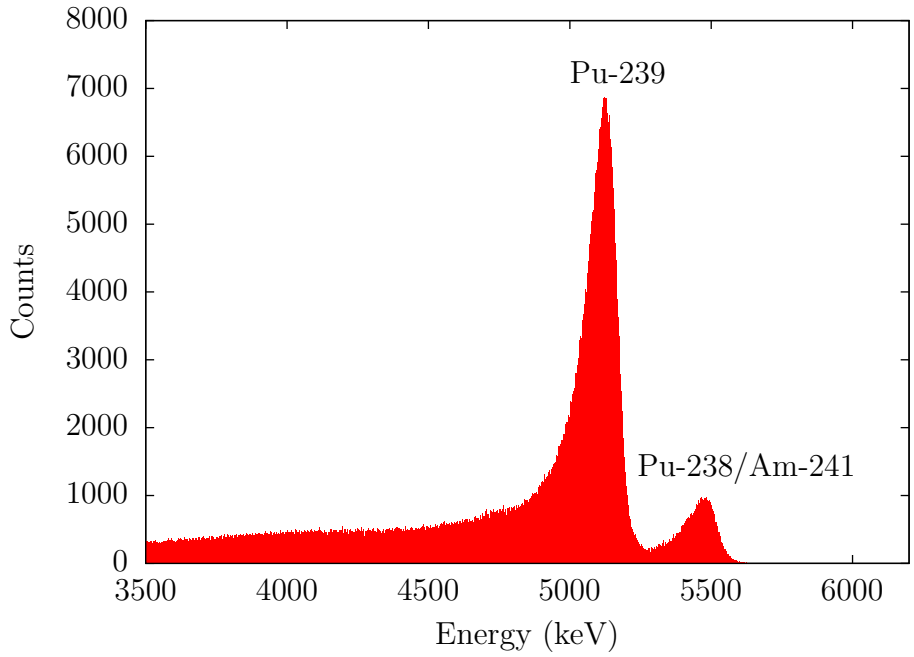

Figure 6.5: Alpha spectroscopy results of the HEU metal experiment catcher plate.

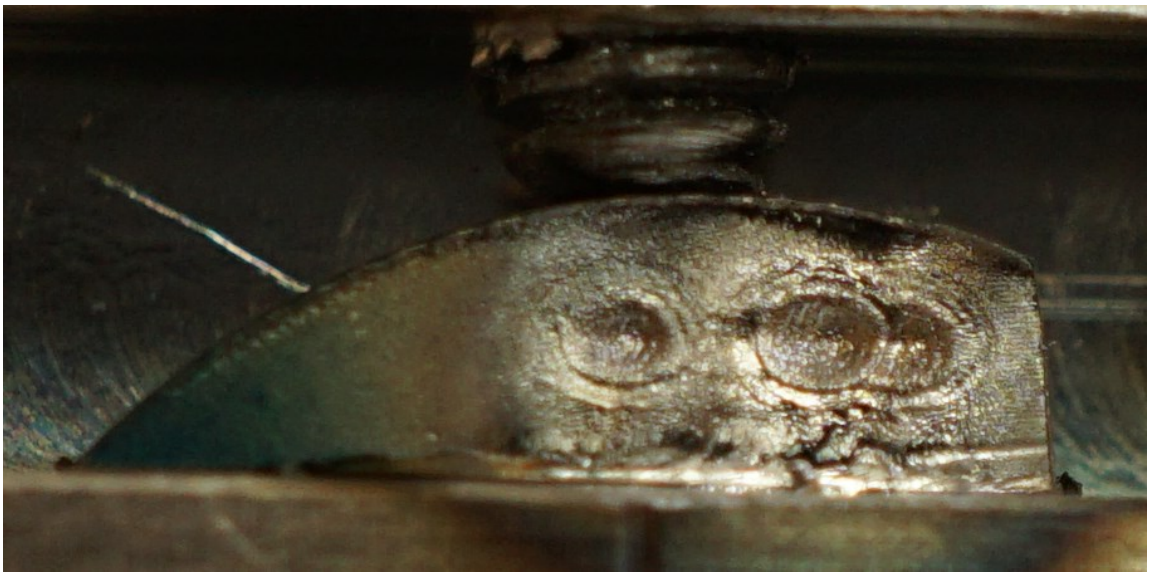

Figure 6.6: Picture of the enriched uranium metal sample after laser irradiation. The silvery metal is visible where the laser shots occurred along with the black oxide around the edges of the sample.

Chapter 7

Uranium Carbide Experiments

The final measurement looking for NEET of ^{235}U was done using the uranium carbide samples. This chapter describes the experiments on depleted uranium carbide and enriched uranium carbide in detail. Due to the low energy of electrons emitted from the internal conversion of ^{235m}U, a correction to the detection efficiency was necessary in order to account for attenuation through the uranium layer. The method used to account for electron attenuation is explained in this chapter. Finally, the statistical analysis used to set the upper limit for NEET in ^{235}U is explained and the result of the analysis for the uranium carbide target is given.

7.1 Depleted Uranium Carbide Experiments

Depleted uranium carbide was the final sample used for the null test experiments. For these experimental runs, the electronics setup was in its final configuration. The electrostatic lens voltage was in its optimal configuration described in Section 3.4.1. The experiment was similar to the ones performed on the other depleted and natural uranium samples. The target was translated during the laser shots. A total of 30 laser shots hit the target per experimental run. A gold coated copper catcher plate was used. A problem that occurred during the DU carbide experiment changed the procedure following the laser irradiation. For the previous null test measurements, the laser irradiation occurred over the course of the first minute. The catcher plate was then moved to the top of the chamber via the translation arm. The analysis began immediately after the catcher plate was in position. In addition, the MCP detector and the electrostatic lens was on the entire time. However, this was not possible with the DU carbide experiment. It was discovered that the movement of the translation arm from the bottom of the chamber to the top of the chamber produced a significant burst of electrons. These electrons were then detected by the MCP detector. The signal would decay with a half-life of approximately 50 minutes. This had not occurred for any of the previous measurements. Attempts were made to ascertain the cause of these electron bursts, but the cause was not determined and it was decided the best approach

would be to mitigate the burst. This was accomplished by introducing argon gas into the chamber. The argon gas would pacify the surfaces and diminish the electron emission. The new procedure was as follows. The MCP detector and the electrostatic lens were off during the laser shots. Following the laser shots, the catcher plate was moved to the top of the chamber. The turbomolecular pump was then turned off and argon was introduced into the chamber. The chamber contained 2 Torr of argon gas. The gas was then pumped out and the MCP detector and electrostatic lens was then turned on. The previous measurements were able to take data looking for the decay of ^{235m}U one minute after the last laser shot. Because the new procedure required the introduction of argon gas and turning on the MCP detector, the data taking could not begin until 13 minutes after the final laser shot.

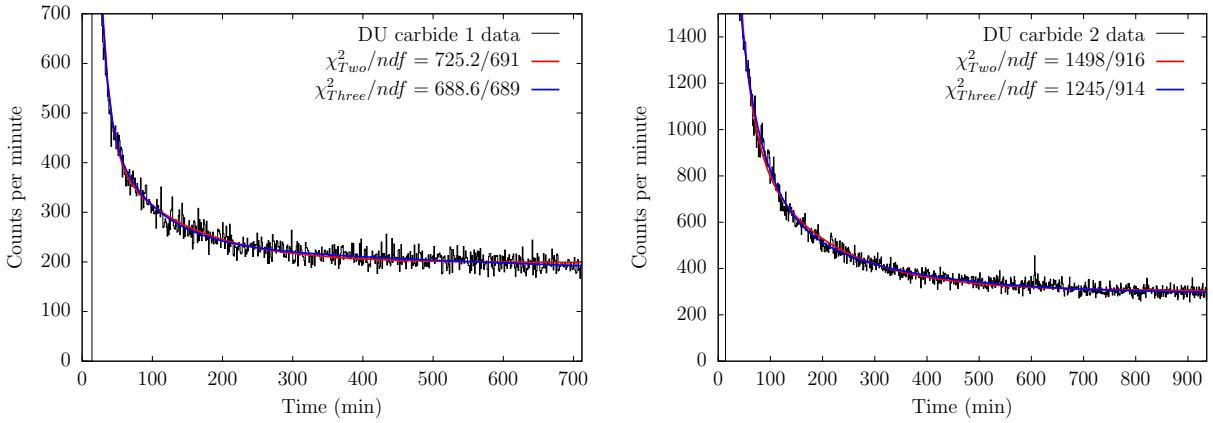

(a) DU carbide 1

(b) DU carbide 2

Figure 7.1: Decay spectra from the DU carbide experiment. Time zero is the start of the laser shots. The detector was fully operational 14 minutes after the start of the laser shots.

Two spectra taken during the uranium carbide measurements can be seen in Figure 7.1. For both measurements, a total of 31 laser shots hit the target. Time zero for the plot occurs when the laser shots started. The data begins 13 minutes after the last laser shot with the fit to the data starting 15 minutes after the last laser shot. Unlike the AM experiment, there were three decays observed in the DU carbide spectra. Both spectra clearly had more than two decaying systems. For the run called DU carbide 1, the half-lives from the fit are 7.16 ± 0.42 min, 47.2 ± 2.6 min, and 775 ± 293 min. Once again, there is a short half-life, a medium length half-life, and a long half-life. It is clear from the data that the longer decay is back, although there is a large uncertainty for both the half-life and the number of decaying systems from the fit. The measurement called DU carbide 2 also was best fit with three decays. The half-lives from the fit are 6.15 ± 0.52 min, 31.8 ± 1.8 min, and 151 ± 9 min. Although the fit parameters for the DU carbide 2 run had lower uncertainties, the reduced χ^2 for the fit is poor. This is being attributed to the presence of nonstatistical counts occurring in the data. This in turn reduced the precision of the fit. No claim about NEET can be

made using the DU carbide data. The multiple decaying systems make it difficult to see a 26 minute decay. Additionally, the background counts and the initial count rate in the spectrum are higher than the other null experiments. While the carbide experiments are not able to make any claims about the NEET rate, they are useful when combined with data from an enriched uranium carbide target. The depleted carbide results are able to be subtracted from the enriched carbide results in order to remove counts that are not due to the difference in isotopics. This is key because it would remove from the enriched carbide's decay spectrum decays that are related to exoelectrons and other processes. However, any counts in the spectrum that are due to nonstatistical effects would not be appropriately removed. Therefore, the subtraction of the depleted carbide data from the enriched carbide data could still have an excess of counts due to processes not related to NEET. This limits the sensitivity to observe NEET using the uranium carbide data.

7.2 Enriched Uranium Carbide Experiments

Following the null test experiments using depleted uranium carbide, the sample of enriched uranium carbide was placed in chamber. The experimental conditions were exactly the same as the depleted uranium carbide experiment. The large electron bursts that were present during the depleted uranium carbide experiment were also present during the enriched uranium carbide experiment. The same procedure involving introducing argon into the chamber to pacify the surfaces was used during the enriched uranium carbide experimental runs. Two spectra taken during the enriched uranium carbide runs are shown in Figure 7.2. Time zero for the plot corresponds to the start of the laser shots. Due to the time it takes to introduce argon into the chamber and then pump it out, the MCP was not on for the 13 minutes following the end of the laser shots. The data begins 13 minutes after the final laser shot and the fit to the data starts 2 minutes after the start of data. A total of 30 laser shots were done for each experimental run. Three decays are evident in the spectra. The half-lives measured for the experimental run called HEU carbide 1 are 14.5 ± 0.9 min, 52.3 ± 9.4 min, and 234 ± 54 min. A very short decay is not evident in the spectrum. There is a long decay of a couple of hundred minutes and then two decays with half-lives of order tens of minutes. For the run called HEU carbide 2, the half-lives are 11.9 ± 0.5 min, 56.6 ± 2.1 min, and 1440 ± 73 min. A very long decay was found in the data along with two half-lives that are similar to the ones measured in the HEU carbide 1 data. It should be noted that the reduced χ^2 for the HEU carbide 2 fit is poor. This is being attributed to nonstatistical counts within the spectrum. These nonstatistical effects were also present in the depleted uranium carbide data.

Due to the multiple half-lives present in the enriched uranium carbide data, it is difficult to make any claim involving whether NEET in ^{235}U occurred. The data did not exhibit a decay that is consistent with the 26 minute decay of $^{235\mathrm{m}}$U. If the isomer was created, its decay would be buried in the data unless there was a large excitation rate. As mentioned in Chapter 4, the plasma generated by the laser used is predicted to make 67,000 isomers per

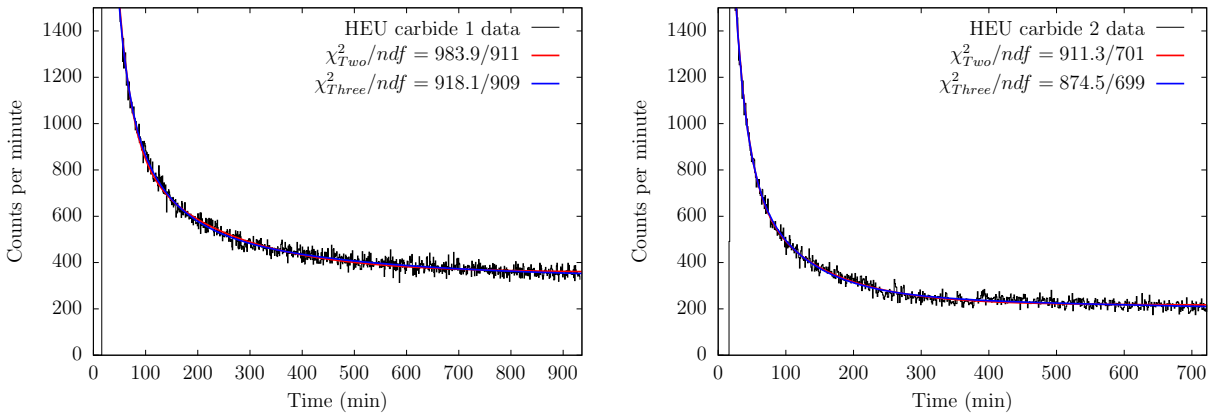

(a) HEU carbide 1

(b) HEU carbide 2

Figure 7.2: Decay spectra from the HEU carbide experiment. Time zero is the start of the laser shots. The detector was fully operational 14 minutes after the start of the laser shots.

laser shot with a NEET excitation rate of 1 s^{-1}. That would create nearly 1 kHz of signal. Since that was not observed, once again the results of previous experiment that claimed a large NEET excitation rate are not reproduced. The NEET rate found in [35] was very small and would not be visible in the enriched uranium carbide data. The observed data was very similar to the data found using the depleted uranium carbide targets. Since the depleted uranium carbide experiment was exactly the same as the enriched uranium carbide experiment except for the target, it is possible to subtract the depleted uranium data from the enriched uranium data. If there were no nonstatistical issues occurring in the spectra, the subtracted data would be flat assuming the data sets are properly scaled. Both HEU carbide 1 and HEU carbide 2 runs were added together. In addition, DU carbide 1 and DU carbide 2 runs were added together. The summed DU spectra was subsequently scaled to the summed HEU data by scaling to the background region in each summed spectrum. The background region consisted of the last 100 channels in the decay spectrum. The summed DU spectrum was subtracted from the summed HEU spectrum and the resulting spectrum is shown in Figure 7.3. A one exponential fit given by the equation

$$Counts = N_1 \exp\left(\frac{-\ln(2)t}{T^1_{1/2}}\right)\left(1 - \exp\left(\frac{-\ln(2)}{T^1_{1/2}}\right)\right) + B \tag{7.1}$$

along with a two exponential fit are shown on the graph. Both fits have poor reduced χ^2 values. Although all of the spectra that were added and subtracted to make the spectrum were collected using the exact same experimental conditions, there is still a decay present in the resulting spectrum. This suggests there is an unknown systematic effect in the experiment. This does explain why the reduced χ^2 values from the fits are large. The subtraction of the summed DU data from the summed HEU data did remove the long half-life evident

in the uranium carbide spectra. The half-life from the one exponential fit was 20.7 ± 1.0 min and the half-lives from the two exponential fit are 16.9 ± 1.5 min and 89.3 ± 43.3 min. It should be noted that the long half-life from the two exponential fit does have a very large uncertainty. What is interesting is that the one exponential fit produces a half-life close to the 26 minute half-life expected from the decay of ^{235m}U. This provides further evidence that previous measurements of NEET in ^{235}U are in fact observations of an unrelated decay. Additionally, there is no evidence of a 26 minute decay in the spectrum. If any isomers were created, the signal from their decay is hidden beneath the other decays.

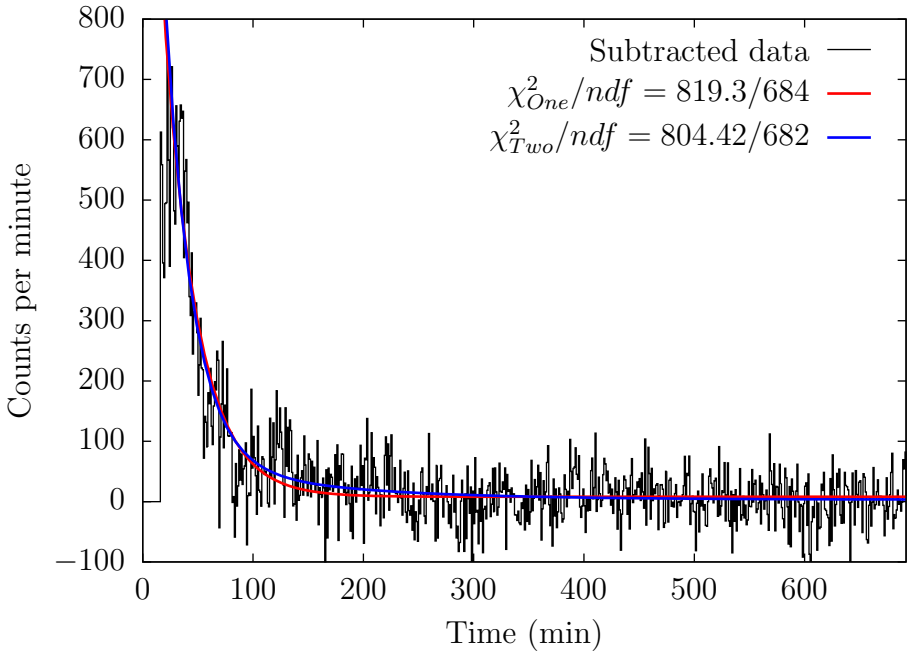

Figure 7.3: Enriched uranium carbide decay spectrum after subtraction of the depleted uranium decay spectrum.

7.3 Data Analysis

Since there was no clear evidence of a 26 minute decay in any of the measured spectra, an upper limit for the NEET excitation rate was determined. The presence of multiple decaying processes in the spectra made this calculation difficult. What had to be determined was the minimum number of isomers that needed to be created in order for their decay to be visible within the experimental data. The method used is found in [71] and the procedure is described below. For the uranium carbide data, the resulting decay after the subtraction of the DU data from the HEU data was assumed to be an exponential decay plus a background. Due to the unknown systematic effect occurring during the experiment, the error bars for

the data were expanded. The scaling factor used to expand the error bars was determined by fitting the one exponential fit function to the data to obtain a reduced χ^2 value. The error bars were subsequently scaled by the square root of the reduced χ^2. Applying the same fit function to the data with expanded error bars would produce a fit with a reduced χ^2 of 1.0. This procedure was applied to the data shown in Figure 7.3 and the subsequent fit parameters are the same but the fit has a reduced χ^2 of 1.0. The scaling of the uncertainty for each point spread out their normal distribution to account for the unknown systematic effect.

To determine the minimum number of isomers that needed to be created in order for their signal to be observed in the data, the data was fit with the function

$$\begin{aligned} Counts = N_1 \exp\left(\frac{-\ln(2)t}{T^1_{1/2}}\right)\left(1-\exp\left(\frac{-\ln(2)}{T^1_{1/2}}\right)\right) \\ +N_2 \exp\left(\frac{-\ln(2)t}{26.0}\right)\left(1-\exp\left(\frac{-\ln(2)}{26.0}\right)\right)+B, \end{aligned} \tag{7.2}$$

where N_1 is the initial number of decaying systems in the data, $T^1_{1/2}$ is the half-life for the decay, N_2 is the number of isomers created, and B is the background. It is initially assumed that N_2 is zero in order to fit the function with a one exponential decay. The uncertainty of the data was subsequently scaled to account for the unknown systematic effect. What was then determined was the confidence interval for N_2. The confidence interval for that parameter shows the level of confidence one has that the value of the parameter falls within a specified range. By perturbing the value of N_2, the confidence interval can be determined using the increase in the total χ^2 of the fit. The 68.3% confidence interval for one degree of freedom occurs when the total χ^2 for the fit increases by 1.00. In the case of N_2, the value of N_2 that produces a change of the total χ^2 value by 1.00 is the minimum number of isomers that one could see in the spectrum with a confidence of 68.3%.

Since the decay observed in the uranium carbide spectrum decays away, the minimum number of isomers required to see the signal changes over time. At short times, there is a large background due to the decay within the spectrum. This extra decay makes it more difficult to observe a 26 minute decay hidden in the data. At later times, the decay in the spectrum is gone, but any signal from the isomer decay would have decayed away too. It was not known at what point in the spectrum one would have the highest sensitivity to see the decay of ^{235m}U. To deal with this issue, the uranium carbide spectrum was fit starting at different times in order to determine at what time after the laser shots had the highest sensitivity to see counts from the decay of ^{235m}U. It was determined that 80 minutes after the last laser shot was the point that had the highest sensitivity to see the decay of ^{235m}U. At 80 minutes, only 12% of the isomer signal would be left. However, the decay visible in Figure 7.3 is significantly diminished after 80 minutes to 7% of its original value. There is a higher signal to noise at 80 minutes compared to earlier and later times that in turn creates the highest sensitivity to see the decay of ^{235m}U. Using the above procedure, the number of isomers that would produce a 68.3% confidence at 80 minutes is 420. That many

isomers would produce a signal of 0.2 Hz in the spectrum compared to 2 Hz of noise. When corrected for the decay time, the number of isomers that needed to be created in order to see a signal during the two enriched uranium carbide runs was 3,544. It should be noted that this minimum number of isomers that need to be created is calculated assuming 100% efficiency for measuring ^{235m}U decay. It is more accurate to call this number the minimum number of electron events associated with the decay of ^{235m}U that needs to occur. The number of electron events associated with the decay of ^{235m}U has be corrected using the efficiency for observing the decay of ^{235m}U in order to obtain the true value for the minimum number of isomers that needed to be created. The minimum number of detectable electron events was used to determine the upper limit for the ^{235}U NEET rate.

7.3.1 Efficiency Correction

A correction for the efficiency of the lens to observe the low energy electrons from the internal conversion of ^{235m}U was needed in order to account for the attenuation of the signal through the uranium layer. The efficiency for the lens system that is described in Section 3.4.2 assumed the electrons emitted were on the surface of the plate. That is because the recoils were slowed in the argon gas and then drifted onto the catcher plate. During the experiments involving uranium, the ablated material would form a uranium layer on the catcher plate. Electrons emitted within the layer of uranium would scatter off of the uranium and this would then reduce the probability of the electrons escaping from the catcher. The inelastic mean free path for a 50 eV electron in solid material is approximately 5 Å [72]. A mean free path of only 5 Å means that the thickness of the layer can only be a few angstroms before there are large losses. Due to a thick layer of uranium attenuating the signal, the number of laser shots per experimental run had to be limited. Having too few shots would reduce the amount of ^{235}U ablated and would reduce the possibility of seeing the isomer. Having too many shots would ablate more uranium and that in turn would increase the background due to alpha decay and attenuate the electron signal. For these reasons, the number of laser shots per experimental run was limited to between 30 and 40.

The thickness of the uranium on the catcher plate was determined using the data from the third uranium ablation experiment described in Section 5.2.1. For that experiment, the mass of uranium found on the catcher plate after one laser shot was 883 ng. Assuming the plate was evenly covered by the uranium and the uranium was at metal density, that one shot would produce a uranium layer which had a thickness of 0.16 Å. However, the uranium does not coat the catcher plate uniformly. This is clearly seen in Figure 5.2 where the different layer thicknesses generate multiple colors on the surface. Segment 5 from the third ablation experiment described in Section 5.2.1 contained the most uranium per unit area. The thickness of the uranium layer on that one segment after one laser shot was 0.34 Å. After 30 laser shots, that segment would have a layer of uranium that is 10 Å. That thickness would significantly reduce the signal from ^{235m}U decay.

To account for the efficiency change due to electron attenuation through the uranium, a correction factor (CF) was needed. The intensity of electrons emitted from a surface with a

layer of material is given by

$$I = I_0 \int_0^{\pi/2} \exp\left(\frac{-t}{\lambda(t,\theta)cos(\theta)}\right) sin(\theta)d\theta, \tag{7.3}$$

where I_0 is the intensity without the layer, t is the thickness of the layer, θ is the angle of emission for the electron, and $\lambda(t,\theta)$ is the effective attenuation length (EAL) for the electrons through the material. Since the electrons emitted due to ^{235m}U decay are emitted throughout the layer and not just from the bottom of the layer, the intensity was averaged over the total layer thickness.

$$I = \frac{I_0}{T} \int_0^{T} \int_0^{\pi/2} \exp\left(\frac{-t}{\lambda(t,\theta)cos(\theta)}\right) sin(\theta)d\theta dt, \tag{7.4}$$

where T is the total thickness of the layer. The values for the practical EAL for 50 eV electrons through uranium were obtained from the NIST Standard Reference Database 82 [73]. 50 eV was the minimum energy for electrons within the NIST database. This energy of electron is a reasonable approximation for the energy of an internal conversion electron from ^{235m}U decay. A matrix of EAL values dependent on both the layer thickness and the angle of emission was created using the data from the NIST database. The table was input into Mathematica [74] in order to create an interpolation for $\lambda(t,\theta)$ that can be used during the integration.

Segment Number	Uranium Layer Thickness (Å)	Correction Factor
Segment 1	3.42	0.509
Segment 2	3.93	0.474
Segment 3	1.74	0.663
Segment 4	8.28	0.291
Segment 5	10.2	0.247
Segment 6	4.44	0.443
Segment 7	4.05	0.466
Segment 8	5.55	0.387
Segment 9	2.28	0.605
Catcher Total	–	0.481

Table 7.1: Uranium layer thickness on the catcher plate and efficiency correction factors. These values assumed 30 laser shots and that the density of the uranium on the catcher plate was 19 g/cm^3.

Since it is evident from both the picture shown in Figure 5.2 and the data found in Table 5.2 that the layer thickness varied across the plate, a correction factor was necessary for each

segment. The correction factors were then averaged to generate a total correction factor due to the uranium layer thickness on the catcher plate. The correction factor for an individual segment is given by the equation

$$CF = 1/T \int_0^T \int_0^{\pi/2} \exp\left(\frac{-t}{\lambda(t,\theta)cos(\theta)}\right) sin(\theta) d\theta dt. \tag{7.5}$$

The layer thickness for each segment was calculated assuming the layer density was 19 g/cm^3 and that there were 30 laser shots. Table 7.1 shows the average uranium thickness of each segment along with the correction factor. The total correction factor for 30 laser shots is 0.481. That means that half of the electrons emitted from ^{235m}U decay would be attenuated. This correction factor applied to the efficiency measured using the ^{239}Pu source gives an efficiency of 2.5% for seeing electrons from the decay of ^{235m}U.

7.3.2 Results

The upper limit for the NEET excitation rate in ^{235}U was determined using the method found in [37]. The NEET excitation rate averaged over the laser pulse is given by

$$\lambda_{NEET} = \frac{N_{^{235m}U}}{N_{^{235}U}\tau\epsilon}, \tag{7.6}$$

where $N_{^{235m}U}$ is the minimum number of detectable electron events associated with ^{235m}U decay, $N_{^{235}U}$ is the number of ^{235}U atoms on the catcher plate, τ is the width of the laser pulse, and ϵ is the detection efficiency. The values of these variables along with their uncertainty are given in Table 7.2. The uncertainty for the minimum number of electron events term, $N_{^{235m}U}$, is due to the expansion of the error bars by the scaling factor. A combination of counting statistics and uncertainty in the collection of uranium yields an 11% uncertainty for the number of ^{235}U atoms on the catcher plate. There is a small uncertainty in the pulse width that comes from the fit of the pulse shape. The uncertainty for the efficiency is a combination of the uncertainty in the solid angle, the uncertainty in the attenuation correction factor, and the statistical uncertainty from the measurement of ^{235m}U decay. The upper limit for the NEET excitation rate with a confidence of 68.3% was calculated to be $\lambda_{NEET} < 1.5 \times 10^{-4}$ s^{-1}. This value can be compared to the previous measurements.

The NEET excitation rate found in Izawa and Yamanaka [33] was 1 s^{-1}. No evidence of this high excitation rate was observed in all subsequent experiments, including this current experiment. The limit set by the current experiment excludes by a wide margin the excitation rate measured in Izawa and Yamanaka. The plasma generated by the laser used in their experiment would be similar to one generated in this experiment. It is possible that the NEET resonance is very narrow, thus making small changes in plasma conditions cause a large change in the observed signal. However, with no subsequent measurement observing the large excitation rate measured in Izawa and Yamanaka, it is clear their observed signal

was due to physical mechanisms unrelated to NEET. The fact that there was a fast decay that was not properly explained in their spectrum furthers this point.

The next two experiments looking for NEET of ^{235}U are described in Arutyunyan et al. [35]. Their first experiment using a CO_2 laser did not see a signal even with using a uranium sample with 10 times more ^{235}U. They set a limit on the cross section for NEET that is equivalent to an excitation rate of $\lambda_{NEET} < 10^{-5}$ s^{-1} [25]. This value is smaller than the limit presented in this dissertation. However, the second experiment reported by Arutyunyan et al. using a high energy electron gun did report a NEET excitation rate of $\lambda_{NEET} \approx 3 \times 10^{-5}$ s^{-1}. This rate is also smaller than the upper limit for the rate measured in this experiment, but the value is most likely not correct. This is because numerous other excitations were possible during the high energy electron experiment. More importantly, the decay signal claimed to be from the isomeric decay had half-lives with large uncertainties. It is clear from this experiment that decays not related to NEET occur following the laser irradiation of uranium. These decays were found to have half-lives with values similar to the half-lives in Arutyunyan et al. that were supposedly due to ^{235m}U decay. For these reasons, it is unlikely the NEET excitation rate measured in Arutyunyan is correct.

The most recent attempt at measuring the NEET excitation rate described in Claverie et al. measured an upper limit of $\lambda_{NEET} < 6 \times 10^{-6}$ s^{-1} [37]. This limit is of course a smaller limit than the limit set from this measurement. However, there are problems with how the limit was determined in Claverie et al. First, the limit was determined by taking ten measurements using the same experimental conditions and adding the data together. What is clear from the experiment described in this dissertation is that each experimental run may not be exactly the same. There may be an unknown systematic issue that would change each run. In addition, no experiment was run using a sample of natural or depleted uranium in order to have a null experiment. The data from a null experiment would help to eliminate decays in their data that are not due to differences in ^{235}U content. A theoretical distribution for the decay of the isomer was added to their data in order to determine their limit. This was a perfect distribution, not one created via a Monte Carlo code. They then obtained a minimum value for the number of isomers they could see in their data. There was no mention of how they determined their fit parameters correspond to the minimum value visible in their data. This combined with the injection of a perfect decay distribution makes

Variable Name	Value	Uncertainty (%)
$N_{^{235m}U}$	3540 atoms	5
$N_{^{235}U}$	1.05×10^{17} atoms	11
τ	9×10^{-9} s	1
ϵ	0.025	11

Table 7.2: Parameters used to calculate the NEET upper limit along with their uncertainties.

their assertion for a minimum number of isomers suspect. The most problematic aspect of their NEET rate calculation is that their data was assumed to be flat. They claimed there was no fast decay in their data after they applied 2 V to their catcher plate. What is clear from one of their figures is that there is still a fast decay visible in their data with 2 V on their catcher plate. It is difficult to tell if there is a fast decay visible in their spectrum that consisted of 10 runs added together. What is unusual about that spectrum is that there appears to be a slight positive slope in their background. This would further cause problems for their calculation of the minimum number of isomers that needed to be created to see a signal.

Even with the issues mentioned above, the limit set in Claverie et al. is consistent with the result found in this dissertation. While it is unlikely their limit is as stringent as they claim, it is clear that they did not observe NEET of ^{235}U. What can be concluded from this experiment is that the NEET rate of ^{235}U is small. Previous measurements claiming to observe NEET of ^{235}U have most likely misinterpreted their results. This experiment and the experiment performed by Claverie et al. have set limits on the ^{235}U NEET rate and have suggested what caused the spurious results reported in Izawa and Yamanaka and Arutyunyan et al.

Chapter 8

Conclusions

An upper limit for the NEET rate in ^{235}U with a confidence of 68.3 % was determined to be $\lambda_{NEET} < 1.5 \times 10^4$ s^{-1}. This limit excludes the NEET rate found in Izawa and Yamanaka and calls into question the results of Arutyunyan et al. While the limit was not as stringent as the limit found in Claverie et al., discrepancies within Claverie et al. suggest that their limit is larger than what they claim. This limit can be compared to the expected NEET rate found in Harston and Chemin and in Morel et al. The NEET rate theorized in Harston and Chemin spanned ten orders of magnitude from 10^{-9} s^{-1} up to 1 s^{-1} and depended on the uranium charge state. The limit determined from this experiment excludes 5 orders of magnitude covered by the Harston and Chemin calculation. The theorized ^{235}U NEET rate found in Morel et al. depended on the density and temperature of the plasma and had a range from 10^{-6} s^{-1} up to 2×10^{-4} s^{-1}. This measurement was only able to exclude the highest theorized NEET rate found in Morel et al.

It was theorized that NEET occurring in uranium could be used for a new form of uranium enrichment. It would require a large NEET rate for it to be a viable method. Let's assume the NEET rate is $\lambda_{NEET} = 1.5 \times 10^{-4}$ s^{-1}. A 1 kg sample of natural uranium is irradiated by a laser with a pulse width of 10 ns. Let's also assume the entire mass of uranium is turned into a plasma with the correct conditions for NEET and the plasma lasts for 10 ns. The amount of ^{235m}U generated with that one laser pulse would be 2.8×10^{10} atoms of ^{235m}U. Assuming one would be able to collect 100% of those ^{235m}U atoms, that equates to extracting 11 picograms of ^{235}U out of a total of 7.2 grams of ^{235}U in the original sample. In order to extract 1 g of ^{235}U using NEET, one would have to irradiate the equivalent of 90,000 metric tons of natural uranium. All of this assumes ideal conditions and a NEET rate near the upper limit found from this experiment. Using the same assumptions and the NEET rate found in Izawa and Yamanaka of 1 s^{-1} would require the processing of 14 metric tons of natural uranium to produce 1 g of ^{235}U. Clearly it is not a viable method of uranium enrichment.

8.1 Future Work

The plasma conditions were one of the most important aspects of this measurement. The NEET rate found in the theory papers was highly dependent on the conditions found within the plasma. Small variations from the ideal charge state result in large changes in the predicted NEET rate. Only the measurement performed by Claverie et al. had some limited knowledge of the plasma conditions. The measurement described in this dissertation based the plasma conditions on the results of the hydrodynamic code. The code used the known experimental conditions in order to be as accurate as possible. Of course the plasma created during the experiment may not have been properly modeled by the code. Variations in the experimental conditions would also affect the plasma generated. The first improvement needed for future NEET experiments involving ^{235}U is a variety of plasma diagnostics to fully understand the plasma generated. These diagnostics would have to be able to measure the fast evolution of the plasma on a nanosecond time scale. Measurements of the electron temperature and ion density are essential. These diagnostics would be able to fully characterize the plasma and actually link the measured NEET rate or limit to specific plasma conditions. Changing the focal length would generate different plasma conditions and variations in the NEET rate would be able to be measured along with their corresponding plasma conditions.

An additional improvement to future measurements would be the acquisition of HEU metal. This experiment encountered numerous roadblocks trying to obtain HEU metal. While 93% enriched uranium metal is available, the high concentration of ^{234}U makes the sample undesirable. The ability to obtain a pure metal sample with an enrichment greater than 99% would greatly improve any future measurements due to the low background of other uranium isotopes, the large proportion of ^{235}U, and the stability of using a metallic target. In addition to obtaining a better target, future measurements would need to focus on the problem of electron signals not associated with the decay of $^{235\mathrm{m}}$U. Both this measurement and Claverie et al. observed decays in their spectrum that were not due to the decay of any isotope. It is likely that Izawa and Yamanaka and Arutyunyan et al. mischaracterized their observed decays as the isomeric decay. Further studies on the observed electron decays using a high efficiency electron spectrometer are needed along with solutions to mitigate their effects. Finally, improvements to the efficiency of the system to detect low energy electrons could provide an order of magnitude improvement to the sensitivity.

With the above improvements, the sensitivity of future experiments would be greatly increased. Four experiments have looked for NEET of ^{235}U and have published conflicting results. The information from this experiment addresses some of the discrepancies observed between the various experiments. This experiment also raised new questions. What exactly is generating the multiple decays seen in the spectra? How does one prevent these decays from occurring? What is the proper method to determine the efficiency for detecting low energy electrons from $^{235\mathrm{m}}$U decay? Future measurements have to address these questions and include the improvements mentioned above in order to discover if NEET of ^{235}U occurs. While NEET of ^{235}U was not observed, the process may still occur for other isotopes with low energy nuclear transitions.

Bibliography

[1] T. Kawano, P. Talou, J. E. Lynn, M. B. Chadwick, and D. G. Madland, "Calculation of nuclear reaction cross sections on excited nuclei with the coupled-channels method," *Phys. Rev. C*, vol. 80, no. 2, p. 024 611, 2009.

[2] W. Younes, H. C. Britt, and J. A. Becker, "Simulated (n,f) cross section of isomeric ^{235m}U," Lawrence Livermore National Laboratory, Tech. Rep. UCRL-CONF-201697, Dec. 2003.

[3] D'Eer, A. and Wagemans, C. and Nève de Mévergnies, M. and Gönnenwein, F. and Geltenbort, P. and Moore, M. S. and Pauwels, J., "Neutron-induced fission of the 26 min ^{235}U isomer," *Phys. Rev. C*, vol. 38, no. 3, pp. 1270–1276, 1988.

[4] 10 C.F.R 73.2 Revised as of January 1, 2014.

[5] *IAEA Safeguards Glossary: 2001 Edition*. Vienna, Austria: International Atomic Energy Agency, 2002.

[6] M. Benedict, T. H. Pigford, and H. W. Levi, *Nuclear Chemical Engineering*, 2nd ed. McGraw-Hill Book Company, 1981.

[7] M. Morita, "Nuclear excitation by electron transition and its application to uranium 235 separation," *Progress of Theoretical Physics*, vol. 49, no. 5, pp. 1574–1586, 1973.

[8] K. Okamoto, "Improvement of efficiency of isotope separation using nuclear excitation by electron transition," *Journal of Nuclear Science and Technology*, vol. 14, no. 10, pp. 762–765, 1977.

[9] K. S. Krane, *Introductory Nuclear Physics*. Hoboken, New Jersey: John Wiley and Sons, 1988.

[10] K. Heyde, *Basic Ideas and Concepts in Nuclear Physics: An Introductory Approach*. Bristol, UK: Institute of Physics Publishing, 2004.

[11] F. F. Karpeshin, M. R. Harston, F. Attallah, J. F. Chemin, J. N. Scheurer, I. M. Band, and M. B. Trzhaskovskaya, "Subthreshold internal conversion to bound states in highly ionized ^{125}Te ions," *Phys. Rev. C*, vol. 53, no. 4, pp. 1640–1645, 1996.

[12] T. Carreyre, M. R. Harston, M. Aiche, F. Bourgine, J. F. Chemin, G. Claverie, J. P. Goudour, J. N. Scheurer, F. Attallah, G. Bogaert, J. Kiener, A. Lefebvre, J. Durell, J. P. Grandin, W. E. Meyerhof, and W. Phillips, "First direct proof of internal conversion between bound states," *Phys. Rev. C*, vol. 62, no. 2, p. 024 311, 2000.

[13] J. F. Chemin, M. R. Harston, F. F. Karpeshin, J. Carreyre, F. Attallah, M. M. Aleonard, J. N. Scheurer, G. Boggaert, J. R. Grandin, and M. B. Trzhaskovskaya, "Nuclear internal conversion between bound atomic states," *AIP Conference Proceedings*, vol. 652, no. 1, pp. 221–231, 2003.

[14] F. Attallah, M. Aiche, J. F. Chemin, J. N. Scheurer, W. E. Meyerhof, J. P. Grandin, P. Aguer, G. Bogaert, J. Kiener, A. Lefebvre, J. P. Thibaud, and C. Grunberg, "Charge state blocking of k-shell internal conversion in ^{125}Te," *Phys. Rev. Lett.*, vol. 75, no. 9, pp. 1715–1718, 1995.

[15] M. Harston, T. Carreyre, J. Chemin, F. Karpeshin, and M. Trzhaskovskaya, "Internal conversion to bound final states in ^{125}Te," *Nuclear Physics A*, vol. 676, no. 14, pp. 143–154, 2000.

[16] National Nuclear Data Center. (7–2014). Chart of nuclides database, [Online]. Available: `http://www.nndc.bnl.gov/chart/`.

[17] B. R. Beck, C. Y. Wu, P. Beiersdorfer, G. V. Brown, J. A. Becker, K. J. Moody, J. B. Wilhelmy, F. S. Porter, C. A. Kilbourne, and R. L. Kelley, "Improved value for the energy splitting of the ground-state doublet in the nucleus ^{229m}Th," Lawrence Livermore National Laboratory, Tech. Rep. LLNL-PROC-415170, Jun. 2009.

[18] M. de Mevergnies and P. D. Marmol, "Effect of the oxidation state on the half-life of ^{235}U^m," *Physics Letters B*, vol. 49, no. 5, pp. 428 –430, 1974.

[19] M. N. de Mévergnies, "Chemical effect on the half-life of U^{235m}," *Phys. Rev. Lett.*, vol. 23, no. 8, pp. 422–425, 1969.

[20] M. N. de Mevergnies, "Perturbation of the ^{235m}U decay rate by implantation in transition metals," *Phys. Rev. Lett.*, vol. 29, no. 17, pp. 1188–1191, 1972.

[21] A. Panov, V. Zhudov, and Y. Teterin, "Conversion spectra of valence shell electrons of oxygen-containing uranium compounds," *Journal of Structural Chemistry*, vol. 39, no. 6, pp. 858–862, 1998.

[22] J. Verbist, J. Riga, J. Pireaux, and R. Caudano, "X-ray photoelectron spectra of uranium and uranium oxides. correlation with the half-life of ^{235}U^m," *Journal of Electron Spectroscopy and Related Phenomena*, vol. 5, no. 1, pp. 193–205, 1974.

[23] A. Panov, "Quantitative conversion spectroscopy of the ultrasoft isomeric transition of uranium-235 and the electronic structure of uranium oxides," *Journal of Experimental and Theoretical Physics*, vol. 85, no. 2, pp. 313–324, 1997.

[24] D. Grechukhin, V. Zhudov, A. Zelenkov, V. Kulakov, B. Odinov, A. Soldatov, and Y. A. Teterin, "Direct observation of strong-electron orbit hybridization in the internal-conversion electron spectra," *Soviet Journal of Experimental and Theoretical Physics Letters*, vol. 31, pp. 592–595, 1980.

[25] M. R. Harston and J. F. Chemin, "Mechanisms of nuclear excitation in plasmas," *Phys. Rev. C*, vol. 59, no. 5, pp. 2462–2473, 1999.

[26] P. Morel, V. Méot, G. Gosselin, D. Gogny, and W. Younes, "Evaluation of nuclear excitation by electronic transition in ^{235}U plasma at local thermodynamic equilibrium," *Phys. Rev. A*, vol. 69, no. 6, 063 414, 2004.

[27] E. V. Tkalya, "Mechanisms for the excitation of atomic nuclei in hot dense plasma," *Laser Physics*, vol. 14, no. 3, pp. 360–377, 2004.

[28] P. Morel, V. Méot, G. Gosselin, G. Faussurier, and C. Blancard, "Calculations of nuclear excitation by electron capture (neet) in nonlocal thermodynamic equilibrium plasmas," *Phys. Rev. C*, vol. 81, no. 3, p. 034 609, 2010.

[29] E. V. Tkalya, "Nuclear excitation in atomic transitions (neet process analysis)," *Nuclear Physics A*, vol. 539, no. 2, pp. 209 –222, 1992.

[30] E. V. Tkalya, "Probability of nonradiative excitation of nuclei in transitions of an electron in an atomic shell," *Sov. Phys. JETP*, vol. 75, no. 2, pp. 200–209, 1992.

[31] E. V. Tkalya, "Theory of the nuclear excitation by electron transition process near the k edge," *Phys. Rev. A*, vol. 75, no. 2, p. 022 509, 2007.

[32] M. Harston, "Analysis of probabilities for nuclear excitation by near-resonant electronic transitions," *Nuclear Physics A*, vol. 690, no. 4, pp. 447 –455, 2001.

[33] Y. Izawa and C. Yamanaka, "Production of ^{235}U^{m} by nuclear excitation by electron transition in a laser produced uranium plasma," *Physics Letters B*, vol. 88, no. 1-2, pp. 59–61, 1979.

[34] Y. Izawa, H. Otani, and C. Yamanaka, "Nuclear excitation of ^{235}U by electron transition in laser produced uranium plasma," in *Laser Interaction and Related Plasma Phenomena*, H. J. Schwarz, H. Hora, M. J. Lubin, and B. Yaakobi, Eds., vol. 5, Plenum Press, 1981, ch. 2, pp. 289–299.

[35] R. V. Arutyunyan, L. A. Bol'shov, V. D. Vikharev, S. A. Dorshakov, V. A. Kornilo, A. A. Krivolapov, V. P. Smirnov, and E. V. Tkalya, "Cross section for excitation of the isomer ^{235m}U in the plasma produced by an electron beam," *Yadernaya Fizika*, vol. 53, pp. 36–40, 1991.

[36] V. I. Zhudov, V. M. Kulakov, B. V. One, and A. D. Panov, in *Accurate Measurements in Nuclear Spectroscopy*, Vilnius: Mosklas, 1984, pp. 109–111.

[37] G. Claverie, M. M. Aléonard, J. F. Chemin, F. Gobet, F. Hannachi, M. R. Harston, G. Malka, J. N. Scheurer, P. Morel, and V. Méot, "Search for nuclear excitation by electronic transition in ^{235}U," *Phys. Rev. C*, vol. 70, no. 4, p. 044 303, 2004.

[38] S. Kishimoto, Y. Yoda, M. Seto, Y. Kobayashi, S. Kitao, R. Haruki, T. Kawauchi, K. Fukutani, and T. Okano, "Observation of nuclear excitation by electron transition in ^{197}Au with synchrotron x rays and an avalanche photodiode," *Phys. Rev. Lett.*, vol. 85, no. 9, pp. 1831–1834, 2000.

[39] S. Kishimoto, Y. Yoda, Y. Kobayashi, S. Kitao, R. Haruki, R. Masuda, and M. Seto, "Nuclear excitation by electron transition on ^{197}Au by photoionization around the K-absorption edge," *Phys. Rev. C*, vol. 74, no. 3, p. 031 301, 2006.

[40] H. Fujioka, K. Ura, A. Shinohara, T. Saito, and K. Otozai, "Observation of nuclear excitation by electron transition (neet) in ^{197}au," *Zeitschrift fr Physik A Atoms and Nuclei*, vol. 315, no. 1, pp. 121–122, 1984.

[41] K. Otozai, R. Arakawa, and T. Saito, "Nuclear excitation by electron transition in ^{189}Os," *Nuclear Physics A*, vol. 297, no. 1, pp. 97–104, 1978.

[42] A. Shinohara, T. Saito, M. Shoji, A. Yokoyama, H. Baba, M. Ando, and K. Taniguchi, "Nuclear excitation in ^{189}os with synchrotron radiation," *Nuclear Physics A*, vol. 472, no. 1, pp. 151–160, 1987.

[43] T. Saito, A. Shinohara, and K. Otozai, "Nuclear excitation by electron transition (neet) in ^{237}Np following k-shell photoionization," *Physics Letters B*, vol. 92, no. 34, pp. 293–296, 1980.

[44] S. Kishimoto, Y. Yoda, Y. Kobayashi, S. Kitao, R. Haruki, and M. Seto, "Evidence for nuclear excitation by electron transition on ^{193}ir and its probability," *Nuclear Physics A*, vol. 748, no. 12, pp. 3–11, 2005.

[45] C. Granja, J. Kuba, A. Haiduk, and O. Renner, "Survey of nuclei for low-energy nuclear excitation in laser-produced plasma," *Nuclear Physics A*, vol. 784, no. 14, pp. 1–12, 2007.

[46] D. Colombant and G. F. Tonon, "Xray emission in laserproduced plasmas," *Journal of Applied Physics*, vol. 44, no. 8, pp. 3524–3537, 1973.

[47] H.-W. Drawin and P. Felenbok, *Data for Plasmas in Local Thermodynamic Equilibrium*. Paris, France: Gauthier-Villars, 1965.

[48] H. R. Griem, "Validity of local thermal equilibrium in plasma spectroscopy," *Phys. Rev.*, vol. 131, no. 3, pp. 1170–1176, 1963.

[49] F. F. Chen, *Introduction to Plasma Physics and Controlled Fusion Volume 1: Plasma Physics*, 2nd ed. New York: Plenum Press, 1984.

[50] R. P. Drake, *High-Energy-Density Physics: Fundamentals, Inertial Fusion, and Experimental Astrophysics*. Springer Science and Business Media, 2006.

[51] J. E. Balmer and T. P. Donaldson, "Resonance absorption of 1.06- μm laser radiation in laser-generated plasma," *Phys. Rev. Lett.*, vol. 39, no. 17, pp. 1084–1087, 1977.

[52] K. R. Manes, V. C. Rupert, J. M. Auerbach, P. Lee, and J. E. Swain, "Polarization and angular dependence of 1.06-μm laser-light absorption by planar plasmas," *Phys. Rev. Lett.*, vol. 39, no. 5, pp. 281–284, 1977.

[53] N. Nakano and H. Kuroda, "Observation of atomic-number-dependent hot electrons due to the resonance absorption in laser plasmas," *Physics Letters A*, vol. 102, no. 9, pp. 412–415, 1984.

[54] W. L. Kruer, *The Physics of Laser Plasma Interactions*. Redwood City, California: Addison-Wesley Publishing Company, 1988.

[55] D. W. Forslund, J. M. Kindel, and K. Lee, "Theory of hot-electron spectra at high laser intensity," *Phys. Rev. Lett.*, vol. 39, no. 5, pp. 284–288, 1977.

[56] K. Estabrook and W. L. Kruer, "Properties of resonantly heated electron distributions," *Phys. Rev. Lett.*, vol. 40, no. 1, pp. 42–45, 1978.

[57] J. E. Balmer and T. P. Donaldson, "Resonance absorption of 1.06-μm laser radiation in laser-generated plasma," *Phys. Rev. Lett.*, vol. 39, no. 17, pp. 1084–1087, 1977.

[58] V. Goldanskii and V. Namiot, "On the excitation of isomeric nuclear levels by laser radiation through inverse internal electron conversion," *Physics Letters B*, vol. 62, no. 4, pp. 393–394, 1976.

[59] F. Brotzen, "Emission of exoelectrons from metallic materials," *physica status solidi (b)*, vol. 22, no. 1, pp. 9–30, 1967.

[60] A. E. Siegman, *Lasers*. Sausalito, California: University Science Books, 1986.

[61] FRED Optical Engineering Software Version 13.90.0. Tucson, Arizona: Photon Engineering, 2014.

[62] J. L. Wiza, "Microchannel plate detectors," *Nuclear Instruments and Methods*, vol. 162, no. 13, pp. 587 –601, 1979.

[63] G. Fraser, "The electron detection efficiency of microchannel plates," *Nuclear Instruments and Methods in Physics Research*, vol. 206, no. 3, pp. 445–449, 1983.

[64] M. Galanti, R. Gott, and J. F. Renaud, "A high resolution, high sensitivity channel plate image intensifier for use in particle spectrographs," *Review of Scientific Instruments*, vol. 42, no. 12, pp. 1818–1822, 1971.

[65] SIMION Version 8.1.1.32. Ringoes, New Jersey: Scientific Instrument Services, Inc., 2013.

[66] J. F. Ziegler, M. Ziegler, and J. Biersack, "SRIM-The stopping and range of ions in matter (2010)," *Nuclear Instruments and Methods in Physics Research Section B: Beam Interactions with Materials and Atoms*, vol. 268, no. 1112, pp. 1818–1823, 2010.

[67] H. Childs, E. Brugger, B. Whitlock, J. Meredith, S. Ahern, D. Pugmire, K. Biagas, M. Miller, C. Harrison, G. H. Weber, H. Krishnan, T. Fogal, A. Sanderson, C. Garth, E. W. Bethel, D. Camp, O. Rübel, M. Durant, J. M. Favre, and P. Navrátil, "VisIt: An End-User Tool For Visualizing and Analyzing Very Large Data," in *High Performance Visualization–Enabling Extreme-Scale Scientific Insight*, 2012, pp. 357–372.

[68] S. S. Harilal, C. V. Bindhu, M. S. Tillack, F. Najmabadi, and A. C. Gaeris, "Internal structure and expansion dynamics of laser ablation plumes into ambient gases," *Journal of Applied Physics*, vol. 93, no. 5, pp. 2380–2388, 2003.

[69] W. Haynes, *CRC handbook of chemistry and physics : a ready-reference book of chemical and physical data*. Boca Raton, Florida: CRC Press, 2014.

[70] R. Brun and F. Rademakers, "ROOT− An object oriented data analysis framework," *Nuclear Instruments and Methods in Physics Research Section A: Accelerators, Spectrometers, Detectors and Associated Equipment*, vol. 389, no. 12, pp. 81–86, 1997.

[71] W. H. Press, S. A. Teukolsky, W. T. Vetterlong, and B. P. Flannery, *Numerical Recipes in C++: The Art of Scientific Computing*, 2nd ed. Cambridge, United Kingdom: Cambridge University Press, 2002.

[72] S. Tanuma, C. J. Powell, and D. R. Penn, "Calculations of electron inelastic mean free paths. IX. Data for 41 elemental solids over the 50 ev to 30 kev range," *Surface and Interface Analysis*, vol. 43, no. 3, pp. 689–713, 2011.

[73] C. J. Powell and A. Jablonski, *NIST Electron Effective-Attenuation-Length Database-Version 1.3*. Gaithersburg, MD: National Institute of Standards and Technology, 2011.

[74] Wolfram Research, Inc., *Mathematica*, Version 10.1. Champaign, IL: Wolfram Research, Inc., 2015.